Aberystwyth University

Doctoral Thesis

Analytical and numerical modelling of thin functional layers

Author:
Gennaro Vitucci

Supervisor:
Prof Gennady Mishuris

Department of Mathematics

2018

Declaration

Word count of thesis: _____

This work has not previously been accepted in substance for any degree and is not being concurrently submitted in candidature for any degree.

Candidate Name: Date: Signed:

_____ _____ _____

This thesis is the result of my own investigations, except where otherwise stated. Where correction services[1] have been used, the extent and nature of the correction is clearly marked in a footnote(s).

Other sources are acknowledged by footnotes giving explicit references. A bibliography is appended.

Candidate Name: Date: Signed:

_____ _____ _____

I hereby give consent for my thesis, if accepted, to be available for photocopying and for inter-library loan, and for the title and summary to be made available to outside organisations.

Candidate Name: Date: Signed:

_____ _____ _____

[1] this refers to the extent to which the text has been corrected by others

Computational power is enormous, quantum computers look almost ready, artificial intelligence is going to undertake millions of intellectual jobs. What is left, then, to a scientist? The pleasure of discovery, the beauty of ideas. Perhaps, but surely a PhD thesis!

Summary of the Thesis

Department of Mathematics

Doctor of Philosophy

Analytical and numerical modelling of thin functional layers

by Gennaro VITUCCI

The thesis deals with the study of thin layers and their function within larger structures. Different thin intephases appearing in mechanics and biomechanics are considered. The work aims at setting a manageable mathematical framework in mechanical modelling. Analytical methods are provided in order to achieve closed-form solutions and effective numerical procedures.

Cartilage, which reveals crucial in transmitting loads without friction along the skeleton, is thoroughly investigated. Governing equations derived within mixture theory are used for a biphasic description of the tissue. Inhomogeneity and anisotropy are introduced and their effect on the global behavior of the tissue is investigated. This is accomplished via integral transforms for relatively small thickness of the layer and short-time asymptotics.

The model is extended to study the three-dimensional contact of cartilage surfaces in the joint. The involved integro-differential equations are solved in closed-form. Next, intra-articular pressurization is taken into account via modelling the whole joint capsule. Implications for healthy degenerated and tissues are discussed.

Lastly, cylindrical multilayer assemblies of layers are examined in the framework of thermoelasticity. The general solutions for the single components are arranged in a way to conveniently constitute a linear system. Perfect and imperfect contact between the layers are considered. An efficient numerical scheme is developed. Simulations are run with a special eye on ceramics.

Contents

Chapter 1

Introduction

Thin structures are ubiquitous in the evolution designed mechanism that constitutes the living matter. Their function can be related to the most diverse physics. They can be used as electro-chemical barriers, as osmotic membranes, as containing walls for vital fluids, for defense, for flight and so on. Usually they are optimal weight saving devices which allow for reduction in volume and energy for transportation without compromising the fundamental purpose that they serve. Humans are quite experienced observers and, accordingly to available technologies, try to imitate nature, their privileged playground. The so called bio-inspired engineering springs up from the principles that they learn about biological systems.

When thin layers need to be modelled mathematically, various complications may arise. A crucial one is related to computational costs and accuracy. If analytical solutions to the governing equations are not available, the domain where they are valid must be subdivided in smaller

subdomains in order to exploit numerical schemes. The concept of thinness itself implies that neighboring structures are relatively larger in one or more dimensions. The minimum mesh size of the domain has therefore be comparable to the smallest structure in the system. This requires, at least near the interface of the thin layer, a very high refinement in the larger body as well. Not only computational costs increase, but the reliability of the solution itself becomes questionable.

It is unfortunate that exact analytical solutions, which are therefore extremely valuable, are very rare commodities. As it happens, there is a wide loophole in between the purely numerical approach and the exact, ideally close-form solution. It is in this opening that the present Thesis aims to slip in.

The relative thinness of the layer can be used as an advantage in pushing the mathematical reasoning a bit further. This is commonly done by use of asymptotic analysis which is of central importance in the applications studied in this work. The obtained solutions in this framework are able to: promptly highlight the major contributions of the involved parameters; clearly give an order of magnitude of the discrepancy from the exact solution.

A major effort in this work relates to the mechanical analysis of the animal synovial joints, where a critical function is carried out by articular cartilage. Existing constitutive models and solutions to the problem of contact between layers are discussed in Sec.1.1. The complex interaction between different parts of a synovial capsule for providing enhanced load support are over-viewed in Sec.1.2. Thinking, among other things, to the

special layered structures characterizing bones, the last section Sec.1.3 is devoted to multilayer assemblies. Artificial materials which resemble biomaterials can be produced only after a correct prediction of the residual stresses that will affect their global properties.

1.1 Material models for contacting cartilage layers

Articular cartilage is a thin tissue which covers the diathrodial joints of the bones. Its structural functions facilitate the transmission of forces between the bones and minimize the contact stresses contact peaks as well as friction by means of self-pressurized lubrication. Provided that the tissue is avascular, it can not self-repair and must ideally last as long as an individual's life. A great interest surrounds its understanding because a correct modeling may lead to correct patient-specific diagnosis for degeneration pathologies and provide operative tools for repair and replacement engineering (see Ateshian et al. [1], Hollister [2] for a more extensive literature review).

This biological tissue peculiar properties are enhanced by a complex multiphasic architecture. A cartilage layer itself is a complex arrangement of a solid matrix saturated by interstitial fluid. The solid phase mainly consists of a porous proteoglycan matrix reinforced by collagen fibers. Both collagen fibrils and proteoglycans are heterogeneously distributed along the depth from the subchondral bone to the contact surface. Their

inhomogeneous arrangement across the layer depth causes inhomogeneity and anisotropy both in the stiffness and permeability of the solid skeleton; besides, it is the cause for the nonlinear time-dependent response to external stimuli. The voids are saturated by an interstitial fluid which is chiefly composed of water and mobile ions causing electro-chemo-mechanical interactions (e.g. Lai et al. [3], Loret and Simões [4]).

The overall mechanical properties of cartilage vary conspicuously during healthy animals' lifetimes. Usually the tissue is softer and more homogeneous in the early phases, while it stiffens, also via thinning, towards adulthood, probably for carrying a bigger bodyweight. Further aging, though, is usually associated with decrease in cells density within the matrix. It is not clear whether bones deterioration causes cartilage damage, or vice versa it is the case for a concatenated feedback (see Silver et al. [5], Lotz and Loeser [6]). The result of world population aging is anyway fuelling the emergence of joint disorders, such as osteoarthritis, which represent a heavy burden on the majority of over-65 people in the world (Buckwalter et al. [7], Arden and Nevitt [8], Anderson and Loeser [9], Bijlsma et al. [10]).

Keeping aside the complex biological interactions which lead to cartilage damage and loss in degenerative pathologies, very clear trends in distinctive material properties are usually spotted. The stiffness of the solid matrix increases, thus undermining the capacity of distributing loads. The permeability increases, with the consequence of faster interstitial fluid flows and decreased pressurization which cripple the beneficial dumping effects of the apparent viscosity (e.g. Herzog et al. [11], Mäkelä et al. [12]).

A comprehensive understanding of the importance of physical parameters in terms of stresses, strains, fluid flow is paramount in prevention, diagnosis and ultimately in designing reliable and bio-mimetic grafts for articular surfaces beyond repair.

One approach to the mechanical analysis consists in considering the solid phase of cartilage as a fibril-reinforced material and modeling the full complex layer through a finite element analysis (e.g. Li et al. [13], Korhonen et al. [14], Wilson et al. [15]). A big concern related to the its use arises in contact. The thin layers act as interphases between structures whose size exceeds the layers' ones of one or more orders of magnitude. An extremely fine mesh is required for both the tissue and the neighbor bone regions, which can easily give place to ill-conditioning and numerical instability of the method if not simply to an enormous increase of the computational effort (see e.g. Wilson et al. [16], Day and Potts [17], Capdeville and Marigo [18] and relative references). Homogenization procedures are then required in order to provide mathematically workable mechanical laws and they are often obtained, following a long tradition, via multi-scale approaches. It is worth to mention the contribution of Sabina and co-authors in the realm of fiber-reinforced materials with transversely isotropic constituents (Rodríguez-Ramos et al. [19], Bravo-Castillero et al. [20], Guinovart-Dıaz et al. [21], Guinovart-Díaz et al. [22], Sabina et al. [23], Berger et al. [24], Guinovart-Díaz et al. [25]) or laminated (Bravo-Castillero et al. [26], Camacho-Montes et al. [27]) materials subjected to elastic, thermal, electrical, magnetic multi-physics. With a homogenized constitutive law in hand, analytical methods to tackle the mechanics of thin layers have been developed.

Chiefly, they consist in reducing the problem to boundary value problems, thus allowing for the substitution of the finite thickness layer with a zero-thickness one (e.g. Bövik [28], Movchan and Movchan [29], Klarbring and Movchan [30], Mishuris [31], Benveniste [32], Sussmann et al. [33]) and sometimes even used to improve and make more efficient experimental data extrapolations (e.g. Öchsner et al. [34], Argatov and Sabina [35]). Their applicability must be examined case by case since inaccurate assumptions may even lead to non-uniqueness of the solutions which does not derive from the original mathematical ansatz, as proved by Dalla Riva and Mishuris [36]. However, these analytical models can be eventually suitable to be thereafter implemented for asymptotic finite-element computation. A recent work has been published by Cerfontaine et al. [37] about the construction of a zero-thickness homogeneous element which includes the hydro-mechanical coupling.

The debate on the appropriate constitutive model for articular cartilage, when assumed as a continuum medium, is wide, but applications basically count two main families: monophasic and multiphasic.

The cartilage material can be considered monophasic and thus its observed delayed response requires a viscoelastic constitutive law (Parsons and Black [38], Armstrong [39]). This approach finds application, for instance, in dynamics (Simon et al. [40], Argatov et al. [41]) and impact (Garcia et al. [42], Selyutina et al. [43]) problems for articular cartilage.

Often one wants, instead, to correctly split the stress contributions of the solid and fluid components. This is crucial when dealing with damage. The stresses on the solids are indeed the cause for irreversible damage

and need to be carefully predicted. The apparently viscous response, in a multiphasic framework, is thus explained as follows. By means of the permeability, the material volumetric changes are due to the fluid flowing non-instantaneously away from the loaded regions. This approach is for instance particularly suited for remarking that the fluid, about 80% of the structure volume, is the main responsible component for load-bearing at early time of deformation.

A steady progress in computational power encouraged to build complex biphasic and triphasic fiber-reinforced material models and to search for solutions by use of finite element analysis (Li et al. [13], Korhonen et al. [14], Placidi et al. [44], Görke et al. [45]). The correspondence between triphasic and biphasic models and the possible occurring difficulties have been discussed in Ateshian et al. [46], Meng et al. [47]. The thinness of the cartilage layers with respect to the size of the bones and contact area, though, may give origin to ill-conditioning, numerical instability and high computational costs due to the necessity for highly refined meshes in the vicinity of the layer (Wilson et al. [16]). Because of this, simpler analytical formulations are still more popular in the field and are, so far, able to include a wide range of nonlinear effects such as strain-dependency of the material properties and tension-compression nonlinearity (e.g. Soltz and Ateshian [48], Holzapfel and Ogden [49]). An effective, intuitive and perhaps the most used model is biphasic formulation as described by the mixture theory by Mow et al. [50]. It is noticeable that, in terms of response for the impacting body, this and the monophasic viscoelastic one can be mathematically connected and give nearly the same results (see Argatov [51]).

With the purpose of studying the contact problem for the diathrodial joint, analytical solutions for biphasic isotropic homogeneous (Ateshian et al. [52], Wu et al. [53], Argatov and Mishuris [54, 55, 56], Quinonez et al. [57]), elastic and viscoelastic (Barber [58], Eberhardt et al. [59], Pérez-González et al. [60], Lin et al. [61], Argatov and Mishuris [62], Argatov [63]) and transversely isotropic models (Argatov and Sabina [35], Rahman and Newaz [64]) have been retrieved. Nevertheless, it has been shown that a depth-dependent variation of the solid matrix stiffness and permeability may play a crucial role in determining the internal behavior of the layer. For instance it affects the homogeneity of the stress fields and improves the superficial fluid support in contact solicitation (see Schinagl et al. [65], Krishnan et al. [66], Federico et al. [67], Federico and Herzog [68], Ateshian et al. [69], Chegini and Ferguson [70]).

A recent interest developed in mechanics, which involves the study of inhomogeneous structures in the second half of the last century for aerospace or geomechanical purposes. The goal is individuating the response features of composite materials, eventually functionally-graded. A number of analytical studies of inhomogeneous structures have been provided for special material variation functions and for arbitrary inhomogeneity in axisymmetric configuration for monophasic layers. An extended bibliography was examined by Tokovyy and Ma [71].

In Chapter 2, *based on Vitucci et al. [72]*, an asymptotic model is constructed for the short-time deformation of an articular cartilage layer modeled as transversely isotropic, transversely homogeneous (TITH) biphasic material. It is assumed that the layer thickness is relatively small

compared to the characteristic size of the normal load applied to the upper surface of the cartilage layer, while the bottom surface is assumed to be firmly attached to a rigid impermeable substrate. The observed time is shorter than the hydrogel characteristic time. In view of applications to articular contact problems it is assumed that the interstitial fluid is not allowed to escape through the articular surface. To the best of our knowledge, this is the first study which provides an analytical solution for the deformation problem of a biphasic inhomogeneous thin layer.

So far, analytical solutions for inhomogeneous materials in contact mechanics have been obtained only for monophasic materials as in Heß [73], Hess and Popov [74]. In Chapter 3, the results of Chapter 2 are used for studying the frictionless contact that involves two thin biphasic TITH cartilage layers firmly attached onto rigid substrates and shaped as elliptic paraboloids of different radii. The layer itself is thin in comparison with the size of the contact area. The emerging three-dimensional contact problem is solved in closed-form and numerical benchmarks for constant and oscillating loads are given. The results are shown in terms of contact pressure and approach of the bones. The latter is derived to be directly proportional to the contact area. Existing experimental data are reinterpreted in view of the model formulation. Comparisons are made with existing solutions for homogeneous biphasic materials in order to underline the functional importance of inhomogeneity in spreading the contact pressure distribution across the contact area. Particular attention is paid to the applicability of the retrieved formulas for interpreting measurements of *in vivo* experiments. Future directions are also

prospected. *The main results of Chapter 3 have been published as Vitucci and Mishuris [75].*

1.2 Joint capsule pressurization

In the previous Section, we have discussed issues regarding the modelling of the cartilagineous tissue in order to predict the distribution of the stresses within the layers and the evolution of the contact. The focus of our novel research with that respect has been centered in investigating the effects and usefulness of the natural distribution of material properties within the tissue. Cartilage is only one of the components of the synovial joint even though the most investigated.

It is the whole capsule that allows for the very efficient mechanism ruling a joint. Articular cartilage surfaces are wet with an external fluid which completely fills the synovial cavity. The fluid must be kept inside the capsule and such task is carried out by the capsule shell. This is composed of an inner impermeable layer, the synovial membrane, covered by a fibrocartilagineous, stiffer outer layer. These two are attached to the bones at their extremities and form a deformable wall which inflates and deflates depending on the position of the contact across the articular cartilage surface, i.e. according to the loading and range of extension of the limb. Additional components such as menisci and ligaments can also be present. The function of the joint capsule is manifold and the scientific community is open to debate about some of the related issues. Nevertheless, it definitely helps, both actively and passively, to keep the

joint in place and provides stability by not permitting the conjoining bones to slip over each other out of the dedicated surfaces (a review in Ralphs and Benjamin [76]).

Many kinds of articular disturbs, especially osteo- or rheumatoid arthritis but also the post-traumatic one, arise in conjunction with synovitis, an inflammation of the membrane, and joint effusion, characterized by extra fluid in the cavity. The symptom is recognizable as swollen joints. The synovial fluid is known to enhance lubrication and to be the mean for transporting nutrients to cartilage and dead cells out of it. On the other hand, it may have a key role in assisting the transmission of loads outside the contact area. Whether this is the case or not, it has been long debated in the past. It has been regularly observed that diseased joints clearly show higher intra-articular pressures than healthy ones. The phenomenon is even sharpened during flexion (see Jayson and Dixon [77, 78], Jawed et al. [79], Viitanen et al. [80]). Myers and Palmer [81] revealed in *in vivo* settings that diseased joints showed much more difficult to inflate than intact ones. The intra-articular pressure soars more than linearly with the liquid volume injected into the cavity.

Experimentalists, for exploring this occurrence, have started to try and pump fluid into the capsule and to measure the resulting pressure-volume curves, whose derivative is called elastance or compliance depending on the axes order. The tests where performed *in vitro* on cadaveric samples. Various measurements have been carried out at different ranges of flexion (Nade and Newbold [82], Schwarz et al. [83], Yen et al. [84]).

We hypothesize in Chapter 4 what is the reason for this specific nonlinearity via a reductionist approach. We set a model of a membrane which follows a version of Laplace's Law including linear stiffness in elongation. This is inflated by a controlled injection of fluid and the 2D analytical solution is shown. Even such an extreme simplification predicts the qualitative behavior seen in experiments.

Effusions cause also loss of strength and control in the surrounding muscles because of neuronal inhibition (Fahrer et al. [85], Torry et al. [86], Hopkins et al. [87]). Volume of effusion, intra-articular pressure and muscles inhibition seem to be all linearly dependent (Spencer et al. [88]). The swollen capsule also impedes a correct blood circulation in the tissues surrounding it (see Geborek et al. [89]). It might be that muscles inhibition is beneficial in mitigating the pain and solicitations to diseased joints. We wonder which, if any, is the mechanical advantage of effusions in the context of contact.

In hips and shoulders, the most mobile joints of the body, the fluid is maintained by a seal structure called labrum, a ring which sits on the acetabulum, the socket of the bone. Labral tears often accompany the arthrodial pathologies. The tears constitute a passage for the intra-articular fluid which leaves the contact area. Contrary to the synovial membrane, this seal has received some attention from mechanical modellers. Henak et al. [90], Todd et al. [91] have published a very detailed finite element analysis, including a great deal of nonlinearities as material properties of cartilage and labrum. The in vitro experiments of Ferguson et al. [92] confirmed the same team's expectation Ferguson et al. [93, 94]

when they focused on variations in global joint consolidation speed. The labrum impermeability gives opportunity to a thin film of synovial fluid to pressurize. Its resistance to be squeezed away evens out the contact pressure. Such a uniformity makes possible to sustain external loads without elevated distortions in the solid, responsible for shear stresses. In Chapter 4, we try for the first time to have a simplified yet mechanically motivated insight into the most influent factors which coordinate the functioning of the joint capsule.

The linear elastic version of Laplace's Law is used for the synovial membrane Gregersen et al. [95]. The cavity fluid is trapped in the synovium by the membrane and the cartilage to preserve its volume. Simultaneously, biphasic articular tissue deforms for accommodating an external load. Combinations of geometry, membrane and cartilage stiffness are simulated analytically in order to qualitatively reproduce some of the more common situations for healthy and diseased joints. A previously disregarded role of the intra-articular pressurization seems to emerge which suggests some of the pros of the specific anatomical arrangement.

1.3 Multilayer assemblies for improved performance

Besides single functional tissues, layered assemblies are a very common feature in natural structures. An optimal combination of layers with different properties and thicknesses are able to provide the complex body

with global characteristics which show better performances than the simply averaged ones. Additionally, every layer can be specialized in a particular function and the whole stack can result in a complicated but effective device. In the framework of relatively stiff parts, calcified organs such as bones and teeth have traditionally attracted huge technological attention. Different animal species have developed highly efficient solutions adapted to their specific needs. Lightweight is coupled with robustness by an intelligent distribution of material properties. The cartilage that covers the bones ends in the joints can be seen as an external extremely soft wet layer, extremely beneficial in an area where wear is one of the main concerns. Either with the goal of imitating such structures or replacing them when they are damaged, ceramics seen to be excellent candidates mainly because of their bio-compatibility. See for instance a review in Giannoudis et al. [96] or an ingenious and promising invention in Tampieri et al. [97].

Ceramics present important and unique features, such as chemical inertness, high-temperature capability, hardness, which make them particularly suited to advanced engineering usages. Simultaneously, a well observed weakness is their fragile behavior. Unexpected brittle fractures with uncontrolled crack propagation speed arise after a certain threshold measure such as toughness is reached. The failure energy may be caused either by mechanical external loads and prestresses or by thermal induced differential deformations facing a material characterized by fortuitous and often designed inclusions (e.g. in fiber-reinforced ceramics).

It has been shown widely in literature that the macro-mechanical behavior with respect to crack propagation can be radically modified assembling multiple layers with different thicknesses and different material properties. Moreover, the full-thickness toughness does not depend only on the individual features of the layers, but also on their interactions. A property to be addressed is specifically the capability of laminar ceramics to deflect cracks.

This can be obtained by facilitating the crack bifurcation, event which can occur only in the case that the crack enters a compressed zone (Bermejo et al. [98], Rao et al. [99]). Thus a crucial role is played by controlling compressive prestresses arising during the cooling process below the joining temperature (Lugovy et al. [100, 101]). From a technological point of view, the creation of such conditions is committed to the choice of materials with different thermal expansion coefficients (Busso et al. [102], Orlovskaya et al. [103], Sglavo and Bertoldi [104]) and/or phase transformation diagrams upon cooling (Pontin and Lange [105], Pontin et al. [106]). A second artifice to alter crack paths is the introduction of weak interfaces between layers in order to lead the deformation energy to obstacle the crack growth along the thickness (Clegg et al. [107]). Delamination gives place to multiple stages fracturing and avoids catastrophic damage. Recent experimental tests confirm – in the framework of dental restoration – the effectiveness of a weak polymeric interlayer inside a stiff ceramic. The structure results toughened against sub-critical crack growth at regions near the interlayer, particularly in comparison with the monolithic sample (Costa et al. [108]).

Similar observations show that a possible improvement of ceramics resistance is possible if the production process is carefully controlled, also considering that usually the size of the layers is of an order of tens of micrometers. On the other hand, aleatory defects arise in every industrial product and if they show features directed in the sense of favoring a catastrophic fracture, both economical and safety losses can invalidate ceramic materials usage for innovative applications. Indeed a practical disadvantage of ceramics is that it may be extremely expensive to predict which sample is brittle without testing it to destruction (Calvert et al. [109]).

Prince Rupert's Paradox is a suggestive phenomenon that resumes the importance of the appearance of unintentional prestresses. The tip of a glass rod is melted before falling into room temperature water. The created drop-shaped solid demonstrates a very singular behavior: while its bulbous head turns very tough, its thin tail not only results fragile, but, when a fracture starts from there, it propagates with an extremely high velocity, in a self-sustained destruction wave, through the whole structure causing instantaneous disintegration (Johnson and Chandrasekar [110]). The reason is clearly to be researched in the arising of high residual stresses. Specifically, stretched internal zones of the head presented an elevate elastic energy which is suddenly released when even a small perturbation occurs (Calvert et al. [109]).

In order to characterize similar features of brittleness, the topic faced in Chapter 5 is the modeling of an axisymmetric multilayer structure. An exact analytical formulation is proposed in the framework of the plane

strain problem for a cylinder encircled by annular layers. Isotropic linear thermoelastic materials constitute the body. Perfect and imperfect contacts between the layers are made available for the analysis. The derived exact solution is compared to finite element simulations. Numerical applications are shown in order to study the dependency of the residual stress distribution on the constituent material properties during a cooling process. The role of residual stresses in brittle materials, particularly ceramics, is discussed. *The Chapter recalls the findings published in Vitucci and Mishuris [111].*

The problem received a large attention, up to the present days. The analysis performed by Stucu [112] presented a recursive algorithm which considers only two concentric cylinders at a time. More recent investigations (Zhang et al. [113], Vedeld and Sollund [114]) extended the analysis to 3D residual stresses and pressurized cylinders, but considering perfect interfaces between layers. In the field of homogeneization of composites, Sevostianov et al. [115] identified the interval of thickness at which the interphase does not influence the effective properties and showed how the imperfection effects described by different models can be expressed in terms of each other.

1.4 Dynamic fracture in discrete structures

As discussed in the previous section, fracture is a source of main concern in engineering layers within a mechanical structure. The contrast in properties with their surroundings often causes cracks to propagate

in the interfaces via delamination. It is highly debated how to analyse dynamic fracture propagation in continua. A common approach consists in reduction to discrete models. This is a method which empowers the analysis of a broad range of phenomena which would not emerge in the settings of continuum mechanics. The approach has found fruitful applications when dealing with crystals, cellular materials, cracks in fiber-reinforced matrices and investigations at the atomic level (e.g.Abraham et al. [116], Atrash and Sherman [117], Bolander and Sukumar [118], Tsai et al. [119], Glassmaker et al. [120]). Lattice structure models allow to predict many kinds of instabilities by intuitive considerations without the need of ad hoc hypotheses (see Marder and Gross [121], Bernstein and Hess [122], Kessler and Levine [123], Bitzek et al. [124]).

Our contribution to the field is out of the main scope of this thesis and thus relegated to the appendices.

A lattice structure is composed of concentrated masses interacting via links characterized by an interaction potential. In Appendix A, we study a discrete string attached to a substrate which deforms quasi-statically because of external loads at one extremity. We derive exactly the relation that shows how the elongation of the springs and the shape of the chain upon pulling are described by the Fibonacci sequence.

The simplest and most common failure criterion for a link neglects dynamic effects and considers the link broken when a certain elongation is reached. A fracture event, though, in many materials turns out to be not simply determined by an instantaneous threshold value for some energy measure like the maximum elongation established above. We deal with

non-instantaneous fracture criteria which nevertheless do not change the material stiffness. The rate with which a body is deformed or an integral measure of the deformation energy provided to a bond before it breaks are examined: the incubation time (IT) and the Tuler-Butcher (TB) criteria.

According to the first of those formulations, the average stress, or equivalently the average linear elastic stretch, over a period of time preceding the breakage is considered as the cause of fracture. Such a period is actually called the incubation time. The criterion was originally formulated in terms of stresses in Petrov and Utkin [125]. The main idea of this approach is that a transient process does not occur instantly but includes a more complicated breakage process. Its realization demands a time period depending on the intensity and shape of loading and on the internal structure of the fractured media. The introduction of the incubation time as additional strength parameter allows one to predict the stress level at the instant of fracture for a variety of loading pulses with different intensities and shapes (Volkov et al. [126]). Hence, the physical meaning of the fracture incubation time is a characteristic time determining the material's ability to resist to dynamic loading. The IT approach has shown to be reliable in different branches of mechanics and physics, such as the dynamic fracture of rocks and concretes, the dynamic yielding of metals, the acoustic ultrasonic cavitation of liquids, etc. (Petrov [127], Gruzdkov and Petrov [128]). Particularly, this criterion was successfully applied to problems of fracture in materials with pre-existing cracks. In this case the criterion can be reformulated in terms of stress intensity factor.

On the other hand, it has been observed that cumulative damage can also be the cause of fracture. A way to quantify it is via the Tuler-Butcher criterion discussed in Tuler and Butcher [129]. The physical meaning of the criterion is that a maximum work has to be done by an external overload on the spring before it collapses. Like IT materials, TB materials can be regarded as one possible extension of ideal brittleness. The criterion has found fruitful applications in analyzing spallation, impact loading, thermal shock caused fracture in rocks, glass, aluminum, copper (see Boustie and Cottet [130], Wei et al. [131], Grady [132]).

The focus of Appendix B is to investigate the influence of the fracture criteria of the links on the dynamic fracture propagation in the same structure. Exclusively cracks which advance at constant speed, in a steady state, are analyzed. Such regimes, indeed, have traditionally been of extreme interest in the field of dynamic fracture and have repeatedly been observed experimentally. A few classical studies can be highlighted for example in Ravi-Chandar and Knauss [133], Fineberg et al. [134], Hauch et al. [135] while the topic gained new attention more recently in discrete structures such as bridges (Brun et al. [136]) or xyloexplosives (King [137]).

Appendix B is devoted to model a fracture in a structured medium when including the aforementioned criteria and their effects on the stable regimes of propagation. The results are expressed in terms of trapped lattice energy, applied remote force and crack tip opening. *The research is the fruit of a collaboration with Nikolai Gorbushin, Grigory Volkov and*

Gennady Mishuris. The main findings are published as Gorbushin et al. [138].

Chapter 2

Deformation of a transversely isotropic, transversely homogeneous biphasic cartilage layer

An infinitely extended thin porous solid matrix is considered to be linear elastic, the interstitial fluid is inviscid, and the problem is stated within the framework developed by Ateshian et al. [52] for an isotropic homogeneous layer and by Argatov and Mishuris [139, 140] for the transversely isotropic case. The fluid flow is impeded through both surfaces and the structure is supposed to be firmly attached to a rigid substrate, thus neglecting the influence of the compliance of the substrate (see Argatov and

Sabina [35]). An arbitrary load is applied to the external surface in absence of normal tractions. Whereas the formulation remains completely general, a special in-depth exponential variation of the stiffness and permeability is assumed. The leading terms of the Laplace transform of the displacement field and the fluid pressure are retrieved. The boundary conditions used in the deformation problem are thought to be applied to contact problems for which analytical results have been already provided in Argatov and Mishuris [139] and which constitute the topic of Chapter 3. In this context, explicit formulae are given for the dependent variables only along the external surface, which is of the main interest in contact problem. Numerical benchmarks are studied and compared to the above mentioned existing solutions.

2.1 Biphasic Model

Mixture theory, originally developed by Mow et al. [50], assumes that all the phases of a mixture are:

- contemporarily present in every point of the multiphasic material, i.e. on average;
- both individually and mutually in equilibrium via momentum exchange.

Even though the theory is not derived entirely by first principles, it has been used fruitfully by most of the scholars in the field of biphasic tissues. As Mow et al. [50] declared in their seminal paper:

The reasonableness of these assumptions is manifested by the ability of this theory to predict the creep, stress relaxation and fluid exudation behaviors exhibited by the tissue.

In our case, we intend to consider only two incompressible phases: a solid, whose pores are fully saturated with a liquid. If Φ_s and Φ_f are the respective volume fractions, then

$$\Phi_s + \Phi_f = 1 \tag{2.1}$$

means saturation: the two phases account for all the volume and no empty space is left to a third phase. The mass conservation, in absence of sources or sinks, must hold for the single phase β of constant density ρ_β and velocity $\dot{\mathbf{u}}_\beta$

$$0 = \frac{\partial \rho_\beta \Phi_\beta}{\partial t} + \nabla \cdot (\rho_\beta \Phi_\beta \dot{\mathbf{u}}_\beta) = \frac{\partial \Phi_\beta}{\partial t} + \nabla \cdot (\Phi_\beta \dot{\mathbf{u}}_\beta). \tag{2.2}$$

Via summing up the mass conservation above for the two components, it follows that, for the whole mixture,

$$\frac{\partial (\Phi_s + \Phi_f)}{\partial t} + \nabla \cdot (\Phi_s \dot{\mathbf{u}}_s + \Phi_f \dot{\mathbf{u}}_f) = 0, \tag{2.3}$$

where $\dot{\mathbf{u}}_i$ are the velocities of the two constituents, t is the time variable, ∇ is the gradient operator in space. By using Eq.(2.1), the continuity becomes only a function of the fluxes as

$$\nabla \cdot (\Phi_s \dot{\mathbf{u}}_s + \Phi_f \dot{\mathbf{u}}_f) = 0. \tag{2.4}$$

This says that the only possible change in volume can be obtained by transport. It is convenient to use the relative seepage flux of the fluid phase

$$\mathbf{f} = \Phi_f(\dot{\mathbf{u}}_f - \dot{\mathbf{u}}_s), \tag{2.5}$$

in order to rewrite the continuity as

$$0 = \nabla \cdot ((1 - \Phi_f)\dot{\mathbf{u}}_s + \Phi_f \dot{\mathbf{u}}_f) = \nabla \cdot (\dot{\mathbf{u}}_s + \mathbf{f})\,. \tag{2.6}$$

The relation between the relative fluid velocity and the fluid pressure gradient ∇p is assumed linear according to Darcy's law

$$\mathbf{f} = -\mathbf{K}\nabla p, \tag{2.7}$$

where $\mathbf{K}$ represents the permeability tensor in its general form. This, substituted into Eq.(2.6), finally gives the relation between fluid pressure and solid phase velocity as

$$\nabla \cdot \dot{\mathbf{u}}_s = \nabla \cdot (\mathbf{K}\nabla p)\,. \tag{2.8}$$

Moreover, the quasi-static momentum balance must also be satisfied. This can be formulated for the phases as

$$\nabla \cdot \boldsymbol{\sigma}_s + \boldsymbol{\pi}_{fs} = \mathbf{0}, \tag{2.9}$$

$$\nabla \cdot \boldsymbol{\sigma}_f + \boldsymbol{\pi}_{sf} = \mathbf{0}, \tag{2.10}$$

$$\boldsymbol{\pi}_{fs} + \boldsymbol{\pi}_{sf} = \mathbf{0}, \tag{2.11}$$

where $\boldsymbol{\pi}_{fs}$ and $\boldsymbol{\pi}_{sf}$ are the exchanged momenta. By simple substitution, this is equivalent to state that in every point of the domain

$$\nabla \cdot (\boldsymbol{\sigma}_s + \boldsymbol{\sigma}_f) = \mathbf{0} \tag{2.12}$$

By applying the divergence theorem, this also means that on the boundaries, where tractions $\hat{\mathbf{t}}$ are assigned at every point of outward normal $\mathbf{n}$, it must hold

$$(\boldsymbol{\sigma}_s + \boldsymbol{\sigma}_f) \cdot \mathbf{n} = \hat{\mathbf{t}}, \tag{2.13}$$

which turns useful for assigning boundary conditions to the mixture.

For elastic solids, the stress depends just on its displacement gradient (i.e., $\boldsymbol{\sigma}_s = \boldsymbol{\sigma}_s(\nabla \mathbf{u}_s)$). The stress on an inviscid liquid is simply determined by the isotropic pressure $\boldsymbol{\sigma}_f = -p\mathbf{I}$. Therefore, the momentum balance reduces to

$$\nabla \cdot \boldsymbol{\sigma} = \nabla \cdot \boldsymbol{\sigma}_s(\nabla \mathbf{u}_s) - \nabla p = \mathbf{0}. \tag{2.14}$$

In the case of linear elasticity, the constitutive relation simplifies further into

$$\boldsymbol{\sigma}_s = \mathbf{A} : \frac{1}{2}\left(\nabla \mathbf{u}_s + \nabla^T \mathbf{u}_s\right) = \mathbf{A} : \boldsymbol{\varepsilon}_s, \tag{2.15}$$

where $\boldsymbol{\varepsilon}_s$ is the solid strain tensor, $\mathbf{A}$ is the stiffness tensor.

Additional considerations are required on the actual form of Eq.(2.15) in order to enforce incompressibility, which is otherwise used only in the continuity equation. As it was shown by Federico et al. [141], such a condition can be expressed as a set of mathematical constraints which relate

the independent material properties. In the simplest case of isotropy, only the deviatoric part of the strains should be considered via the shear modulus. In the case of transverse isotropy, considered in this Chapter, the general independent material parameters are five. The strict incompressibility reduces this number to three.

The set of continuity, momentum balance and constitutive Eqs.(2.8),(2.14) and (2.15) are used within this Thesis for describing the cartilage behavior. The unknowns for which the problem has to be solved are the solid displacements $\mathbf{u}_s$ and the scalar field of the fluid pressure p. For this reason, the subscript s is dropped from the stresses, strains and displacements of the solid matrix without risks of confusion.

2.2 Deformation problem settings

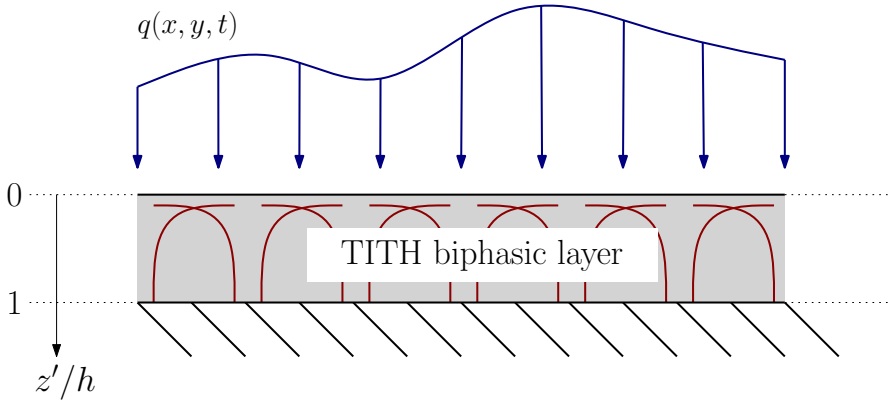

FIGURE 2.1: Geometry of the problem. Thin biphasic TITH layer contrained at the bottom and loaded on the top surface. Neither of the two surfaces allow fluid flow.

The cartilage layer is modelled as a transversely isotropic, transversely homogeneous (TITH) porous linear elastic solid matrix, saturated by a fluid with zero-viscosity. In matrix form, the elastic stiffness tensor can be written as a 6x6 symmetric matrix. In the case of transverse isotropy, Eq.(2.15) becomes

$$\begin{bmatrix} \sigma_{11} \\ \sigma_{22} \\ \sigma_{33} \\ \sigma_{23} \\ \sigma_{13} \\ \sigma_{12} \end{bmatrix} = \begin{bmatrix} A_{11} & A_{12} & A_{13} & & & \\ A_{12} & A_{11} & A_{13} & & & \\ A_{13} & A_{13} & A_{33} & & & \\ & & & 2A_{44} & & \\ & & & & 2A_{44} & \\ & & & & & 2A_{66} \end{bmatrix} \begin{bmatrix} \varepsilon_{11} \\ \varepsilon_{22} \\ \varepsilon_{33} \\ \varepsilon_{23} \\ \varepsilon_{13} \\ \varepsilon_{12} \end{bmatrix}. \tag{2.16}$$

Within the same framework, the permeability matrix is diagonal with only two independent components

$$\mathbf{K} = \begin{bmatrix} K_1 & & \\ & K_1 & \\ & & K_3 \end{bmatrix}. \tag{2.17}$$

The particular boundary-value problem investigated here describes a thin layer completely constrained at the bottom by a flat impermeable surface. A vertical load, i.e. without shear components, is applied at its top.

We use the superscript $'$ uniquely in the following of this chapter for indicating absolute, non-scaled quantities. While $\mathbf{x}' = [x_1', x_2']$ are the in-plane coordinates, z', the vertical one, is directed downward, set to 0 at the top. The displacements of the solid matrix are also distinguished

between in-plane and z'-directed ones as

$$\mathbf{u}' = \begin{bmatrix} v_1' \\ v_2' \\ w' \end{bmatrix} = \begin{bmatrix} \mathbf{v}' \\ w' \end{bmatrix}. \tag{2.18}$$

In order to take into account transverse homogeneity, both stiffness and permeability depend on the out-of-plane direction as

$$\mathbf{A} = \mathbf{A}(z') \qquad \text{and} \qquad \mathbf{K} = \mathbf{K}(z'). \tag{2.19}$$

The solid matrix equilibrium and constitutive equations Eqs.(2.14)-(2.15) are therefore written as follows:

$$\begin{aligned} &\frac{\partial}{\partial z'}\left(A_{44}\frac{\partial \mathbf{v}'}{\partial z'}\right) + A_{13}\frac{\partial \nabla_{\mathbf{x}'} w'}{\partial z'} + \frac{\partial}{\partial z'}\left(A_{44}\nabla_{\mathbf{x}'} w'\right) + A_{66}\Delta_{\mathbf{x}'}\mathbf{v}' \\ &\qquad + (A_{11} - 2A_{66} - A_{12})\nabla_{\mathbf{x}'}\nabla_{\mathbf{x}'}\cdot\mathbf{v} + (A_{66} + A_{12})\mathcal{H}_{\mathbf{x}'}\mathbf{v}' \\ &\qquad = \nabla_{\mathbf{x}'} p, \end{aligned} \tag{2.20}$$

$$\frac{\partial}{\partial z'}\left(A_{33}\frac{\partial w'}{\partial z'}\right) + \frac{\partial}{\partial z'}\left(A_{13}\nabla_{\mathbf{x}'}\cdot\mathbf{v}'\right) + A_{44}\frac{\partial \nabla_{\mathbf{x}'}\cdot\mathbf{v}'}{\partial z'} + A_{44}\Delta_{\mathbf{x}'} w' = \frac{\partial p}{\partial z'}. \tag{2.21}$$

In this notation: $\mathcal{H}_{\mathbf{x}}$ indicates the in-plane Hessian matrix operator whose ij-components are $\frac{\partial^2}{\partial x_i' \partial x_j'}$; $\nabla_{\mathbf{x}'}$ is the in-plane gradient of components $\frac{\partial}{\partial x_i'}$; $\Delta_{\mathbf{x}'}$ represents the in-plane Laplacian operator $\nabla_{\mathbf{x}'}\cdot\nabla_{\mathbf{x}'}$.

The continuity equation Eq.(2.8) for the fluid and Darcy's law are collected as

$$\frac{\partial}{\partial z'}\left(K_3\frac{\partial p}{\partial z'}\right) - \frac{\partial \nabla_{\mathbf{x}'}\cdot\mathbf{v}'}{\partial t'} - \frac{\partial^2 w'}{\partial t'\partial z'} + K_1\Delta_{\mathbf{x}'}p = 0. \tag{2.22}$$

If the thickness of the layer is h, the constraint at the bottom surface leads to the boundary conditions

$$\mathbf{v}'|_{z'=h} = 0, \tag{2.23}$$

$$w'|_{z'=h} = 0, \tag{2.24}$$

while the impermeability of both the bottom and upper surfaces is obtained by setting the relative flux to zero in Eq.(2.7) as

$$\left.\frac{\partial p}{\partial z'}\right|_{z'=h} = 0, \tag{2.25}$$

$$\left.\frac{\partial p}{\partial z'}\right|_{z'=0} = 0. \tag{2.26}$$

The frictionless contact between the rigid punch and the top of the layer allows to state that

$$\left.\frac{\partial \mathbf{v}'}{\partial z'} + \nabla_{\mathbf{x}'}w'\right|_{z'=0} = \mathbf{0}. \tag{2.27}$$

The top surface itself must be also in equilibrium and respect Eq.(2.13), that is

$$\left.A_{13}\nabla_{\mathbf{x}'}\cdot\mathbf{v}' + A_{33}\frac{\partial w'}{\partial z'} - p\right|_{z'=0} = -q. \tag{2.28}$$

As for the initial conditions, every variable is set to 0 at $t' = 0$.

2.3 Asymptotic Analysis

The thinness of the layer suggests to make use of perturbation analysis to solve the system of second order partial differential equations described in Section 3.1. The thickness h is assumed to be represented as

$$h = \varepsilon h_*, \tag{2.29}$$

where ε is a small positive parameter and h_* is a length independent of ε with the the same order of magnitude as the characteristic in-plane length of the loaded layer. Thus, it becomes useful:

- to introduce the new independent variables

$$z = \frac{z'}{h}, \quad t = \frac{t'}{h^2}, \quad x_i = \frac{x_i'}{h_*} \quad (i = 1, 2), \tag{2.30}$$

  so that $z \in [0, 1]$;

- to set the new unknowns variables

$$w = \frac{w'}{h}, \quad \mathbf{v} = \frac{\mathbf{v}'}{h}; \tag{2.31}$$

- to express the elastic parameters A_{jk} and the hydraulic resistivities K_j $(j, k = 1, 2, 3)$ as functions of the new stretched vertical coordinate $z = \frac{z'}{h} = \frac{z'}{\varepsilon h_*}$.

Our assumption is that the asymptotic expansion of the unknowns is written as follows:

$$\begin{aligned} \mathbf{v} &= \varepsilon^0 \mathbf{v}_0 + \varepsilon^1 \mathbf{v}_1 + \varepsilon^2 \mathbf{v}_2 ..., \\ w &= \varepsilon^0 w_0 + \varepsilon^1 w_1 + \varepsilon^2 w_2 ..., \\ p &= \varepsilon^0 p_0 + \varepsilon^1 p_1 + \varepsilon^2 p_2 ... . \end{aligned} \tag{2.32}$$

Substituting (2.30) and (2.31) into Eqs.(2.20)–(2.22) leads to a new set of differential equations governing the problem

$$\begin{aligned} &\frac{\partial}{\partial z}\left(A_{44}\frac{\partial \mathbf{v}}{\partial z}\right) + \varepsilon\left(A_{13}\frac{\partial \nabla_{\mathbf{x}} w}{\partial z} + \frac{\partial}{\partial z}\left(A_{44}\nabla_{\mathbf{x}} w\right) - \nabla_{\mathbf{x}} p\right) \\ &\qquad + \varepsilon^2\left((A_{11} - 2A_{66} - A_{12})\nabla_{\mathbf{x}}\nabla_{\mathbf{x}}\cdot\mathbf{v} + (A_{66} + A_{12})\mathbf{H}_{\mathbf{x}}\mathbf{v}\right) \\ &\qquad = \mathbf{0}, \end{aligned} \tag{2.33}$$

$$\begin{aligned} &\frac{\partial}{\partial z}\left(A_{33}\frac{\partial w}{\partial z}\right) - \frac{\partial p}{\partial z} + \varepsilon\left(\frac{\partial}{\partial z}\left(A_{13}\nabla_{\mathbf{x}}\cdot\mathbf{v}\right) + A_{44}\frac{\partial \nabla_{\mathbf{x}}\cdot\mathbf{v}}{\partial z}\right) \\ &\qquad + \varepsilon^2 A_{44}\Delta_{\mathbf{x}} w = 0, \end{aligned} \tag{2.34}$$

$$\frac{\partial}{\partial z}\left(K_3\frac{\partial p}{\partial z}\right) - \frac{\partial^2 w}{\partial t \partial z} + \varepsilon\left(-\frac{\partial \nabla_{\mathbf{x}}\cdot\mathbf{v}}{\partial t}\right) + \varepsilon^2 K_1 \Delta_{\mathbf{x}} p = 0. \tag{2.35}$$

In the same way, the boundary conditions take the form

$$\mathbf{v}|_{z=1} = \mathbf{0}, \quad w|_{z=1} = 0, \tag{2.36}$$

$$\left.\frac{\partial p}{\partial z}\right|_{z=1} = 0, \quad \left.\frac{\partial p}{\partial z}\right|_{z=0} = 0, \tag{2.37}$$

$$\left.\frac{\partial \mathbf{v}}{\partial z} + \varepsilon \nabla_{\mathbf{x}} w\right|_{z=0} = \mathbf{0}, \tag{2.38}$$

$$A_{33}\frac{\partial w}{\partial z} - p + q + \varepsilon\, A_{13} \nabla_{\mathbf{x}} \cdot \mathbf{v}|_{z=0} = 0. \tag{2.39}$$

Using the expansions (2.32) to solve the system (2.33)–(2.35) and taking into account the boundary conditions, it is easy to verify that some of terms of the expansions are identically zero

$$\mathbf{v}_0 = \mathbf{v}_2 = \mathbf{0}, \quad w_0 = w_1 = p_1 = 0, \tag{2.40}$$

$$\tag{2.41}$$

whereas

$$p_0 = q, \qquad \mathbf{v}_1 = \nabla_{\mathbf{x}} q \int_1^z \frac{z}{A_{44}}\, \mathrm{d}z. \tag{2.42}$$

The ε^2-terms of Eqs. (2.34) and (2.35) yield

$$\frac{\partial}{\partial z}\left(A_{33}\frac{\partial w_2}{\partial z}\right) + \frac{\partial}{\partial z}\left(A_{13}\nabla_{\mathbf{x}} \cdot \mathbf{v}_1\right) - \frac{\partial p_2}{\partial z} + A_{44}\frac{\partial \nabla_{\mathbf{x}} \cdot \mathbf{v}_1}{\partial z} = 0, \tag{2.43}$$

$$\frac{\partial}{\partial z}\left(K_3\frac{\partial p_2}{\partial z}\right) - \frac{\partial^2 w_2}{\partial t \partial z} - \frac{\partial \nabla_{\mathbf{x}} \cdot \mathbf{v}_1}{\partial t} + K_1 \Delta_{\mathbf{x}} q = 0. \tag{2.44}$$

The boundary condition (2.39) becomes

$$\left.A_{33}\frac{\partial w_2}{\partial z} + A_{13}\nabla_{\mathbf{x}} \cdot \mathbf{v}_1 - p_2\right|_{z=0} = 0. \tag{2.45}$$

Integrating Eq. (2.43) once between 0 and z and applying the boundary condition above leads to the following equation:

$$A_{33}\frac{\partial w_2}{\partial z} = p_2 - \Delta_{\mathbf{x}} q\frac{z^2}{2} - A_{13}\nabla_{\mathbf{x}}\cdot\mathbf{v}_1. \tag{2.46}$$

Thanks to Eq. (2.42) and the equation above, Eq. (2.44) can be expressed exclusively in terms of p_2 as

$$\begin{aligned}\frac{\partial^2 p_2}{\partial z^2} - \frac{1}{K_3}\frac{\partial K_3}{\partial z}\frac{\partial p_2}{\partial z} - \frac{1}{K_3 A_{33}}\frac{\partial p_2}{\partial t} = \\ \frac{1}{K_3 A_{33}}\frac{\partial \Delta_{\mathbf{x}} q}{\partial t}\left((A_{33}-A_{13})\int_1^z \frac{z}{A_{44}}\,\mathrm{d}z - \frac{z^2}{2}\right) - \frac{K_1}{K_3}\Delta_{\mathbf{x}} q,\end{aligned} \tag{2.47}$$

where the unknowns are kept on the left-hand side.

It remains to find the terms w_2 and p_2 of the asymptotic expansion of the out-of-plane displacement field and fluid pressure by means of Eqs.(2.46)-(2.47). This is accomplished, as detailed in the next Section, by use of integral transforms and assumptions on the distribution of the material properties through the layer.

2.4 Laplace transformation in the case of a specific type of inhomogeneity

Some assumption on the variation of the five parameters A_{13}, A_{33}, A_{44}, K_1, and K_1 needs to be made in order to simplify the continuation. In

the present work we consider that they vary exponentially along the z-axis while the product $K_3 A_{33}$ remains constant. This feature is validated by experimental observation which suggests that the axial mechanical stiffness — then A_{33} — increases with the depth from the surface toward the bone (see e.g.Schinagl et al. [65], Klein et al. [142], Wang et al. [143]), while the fact that a decreasing porosity causes an overall reduction in permeability was shown in Federico and Herzog [68], where, through this hypothesis, the classical results of Maroudas et al. [144] were fitted and justified. The exponential depth-dependency used later on is

$$\begin{cases} A_{33} = a_{33}\mathrm{e}^{2\gamma z}, \quad A_{44} = a_{44}\mathrm{e}^{\alpha z}, \quad A_{13} = a_{13}\mathrm{e}^{\alpha_{13} z}, \\ K_3 = k_3\mathrm{e}^{-2\gamma z}, \quad K_1 = k_1\mathrm{e}^{-\gamma_1 z}, \end{cases} \tag{2.48}$$

where $\gamma > 0$ is a specified constant. These expressions are substituted into Eq. (2.47) and the time variable t is changed into the dimensionless one by the formula

$$\tau = K_3 A_{33} t.$$

Recalling that any unknown is set to 0 for $-\infty < t < 0^-$, the Laplace transformation[1] with respect to τ is applied to yield

[1] Given a function $f(\tau)$, its Laplace transform of parameter s is defined as

$$F(s) = \mathcal{L}\{f\}(s) = \int_0^{+\infty} f(\tau)\mathrm{e}^{-s\tau}\,\mathrm{d}\tau.$$

i	M_i	$b_{i1}\alpha^2 a_{44}$	$b_{i0}\alpha^2 a_{44}$
1	$\alpha_{13}-\alpha$	αa_{13}	a_{13}
2	α_{13}	0	$-a_{13}(1+\alpha)\mathrm{e}^{-\alpha}$
3	$2\gamma-\alpha$	$-\alpha a_{33}$	$-a_{33}$
4	2γ	0	$a_{33}(1+\alpha)\mathrm{e}^{-\alpha}$

TABLE 2.1: Parameters of $\Phi_i^{(M)}$

$$\frac{\partial^2 P}{\partial z^2}-2\gamma\frac{\partial P}{\partial z}-sP= s\Delta_{\mathbf{x}}Q\left(\frac{a_{33}\mathrm{e}^{2\gamma z}-a_{13}\mathrm{e}^{\alpha_{13}z}}{a_{44}}\int_1^z\frac{z}{\mathrm{e}^{\alpha z}}\,\mathrm{d}z-\frac{z^2}{2}\right)-\frac{k_1}{k_3}\mathrm{e}^{(2\gamma-\gamma_1)z}\Delta_{\mathbf{x}}Q, \tag{2.49}$$

where $P(s)$ and $Q(s)$ are respectively the Laplace transforms of $p_2(\tau)$ and $q(\tau)$, s is the transformation parameter. For the terms that multiply an exponential function of z we introduce the following abbreviation:

$$\Phi_i^{(M)}=\mathrm{e}^{M_i z}(b_{i1}z+b_{i0})\quad(i=1,2,3,4), \tag{2.50}$$

whose coefficients are resumed in Table 2.1. It ensues that the second order ordinary differential equation above is suitable to be rewritten as

$$\frac{\partial^2 P}{\partial z^2}-2\gamma\frac{\partial P}{\partial z}-sP=\Delta_{\mathbf{x}}Q\sum_{i=1}^{6}\Upsilon_i(s,z). \tag{2.51}$$

Here we have introduced the notation

$$\begin{aligned} &\Upsilon_i(s,z) = s\Phi_i^{(M)}(z), \quad i = 1,2,3,4, \\ &\Upsilon_5(s,z) = -s\frac{z^2}{2}, \quad \Upsilon_6(s,z) = -\frac{k_1}{k_3}\mathrm{e}^{(2\gamma-\gamma_1)z}. \end{aligned} \tag{2.52}$$

Posed $\sigma(s) = \sqrt{\gamma^2 + s}$, the solution of the left-hand side of Eq. (2.51) is

$$P_h = \mathrm{e}^{\gamma z}(C_1 \sinh \sigma z + C_2 \cosh \sigma z), \tag{2.53}$$

where the two constants $C_1(s)$ and $C_2(s)$ must be determined to fulfil the boundary conditions $\frac{\partial P}{\partial z} = 0$ at $z = 0$ and $z = 1$ together with the particular solution which satisfies its right-hand side.

Within the Appendices 2.A, 2.B and 2.C, we deal with the particular solution of the non-homogeneous Eq. (2.51) splitting it into three parts (see Eq. (2.52)) as follows: one part containing the so-called $\Phi_i^{(M)}$-terms, corresponding to $\Upsilon_i(s,z)$, $i = 1,2,3,4$, one containing the z^2-term, corresponding to $\Upsilon_5(s,z)$, and the last one which involves the permeability, specifically the ratio $\frac{K_1(z)}{K_3(z)}$. This term, corresponding to $\Upsilon_6(s,z)$, will take the name of k-term.

It is useful to calculate (with the same subdivision) the integral $\xi = -\int_z^1 p_2 \mathrm{e}^{-2\gamma z}\,\mathrm{d}z$ which comes out from Eq. (2.46), if w_2 is recovered and the boundary condition $w_2 = 0$ at $z = 1$ is applied.

$$w_2 = -\int_z^1 \frac{\mathrm{e}^{-2\gamma z}\left(p_2 - \Delta_{\mathbf{x}} q \frac{z^2}{2} - A_{13}\nabla_{\mathbf{x}} \cdot \mathbf{v}_1\right)}{a_{33}}\,\mathrm{d}z. \tag{2.54}$$

i	M_i	$b_{i1}\alpha^2 a_{44}$	$b_{i0}\alpha^2 a_{44}$
1	$-\alpha$	αa_{13}	a_{13}
2	0	0	$-a_{13}(1+\alpha)\mathrm{e}^{-\alpha}$
3	$-\alpha$	$-\alpha a_{33}$	$-a_{33}$
4	0	0	$a_{33}(1+\alpha)\mathrm{e}^{-\alpha}$

TABLE 2.2: Parameters of $\Phi_i^{(M)}$ for $\alpha_{13} = \gamma = 0$

In particular we are interested in the evaluation of the pressure and the vertical displacement at the load application surface ($z = 0$) because those results are especially important for contact problems.

The asymptotic expansion for the fluid pressure at the load application surface ($z = 0$) results from Eq. (2.32) and Eq. (2.41):

$$p_0 \approx q(\tau) + \frac{h^2}{h_*^2} p_{02}(\tau), \tag{2.55}$$

$$p_{02} = \sum_{i=1}^{4} p_{0i}^{(M)} + p_0^{(2)} + p_0^{(k)}, \tag{2.56}$$

where the terms $p_{0i}^{(M)}$, $p_0^{(2)}$ and $p_0^{(k)}$ must be calculated as derived in the Appendices 2.A, 2.B and 2.C.

Let us assume that both α_{13} and γ are zero. In this case Table 2.1 becomes Table 2.2. For studying the homogeneous case α must also tend to zero, so that

$$-\sum_{i=1}^{4} b_{i0}\Delta_{\mathbf{x}} q = \Delta_{\mathbf{x}} q \frac{a_{33} - a_{13}}{a_{44}} \lim_{\alpha\to 0} \frac{1-(1+\alpha)\mathrm{e}^{-\alpha}}{\alpha^2} = \frac{1}{2}\frac{a_{33} - a_{13}}{a_{44}}\Delta_{\mathbf{x}} q, \tag{2.57}$$

$$\sum_{i=1}^{4}\sum_{n=0}^{\infty}\operatorname{Res}\left\{\mathrm{e}^{s\tau}\Omega_i^{(M)}(s);s_n\right\}*\Delta_{\mathbf{x}}q=\frac{a_{33}-a_{13}}{a_{44}}2\sum_{n=0}^{\infty}(-1)^n\mathrm{e}^{-n^2\pi^2\tau}*\Delta_{\mathbf{x}}q, \tag{2.58}$$

where the notation for convolution $*$ and complex residue Res are used according with Appendix 2.A. The two equations above imply that the homogeneous solution regarding the $\Phi_i^{(M)}$-terms is written as

$$\sum_{i=1}^{4}p_{0i}^{(Mh)}=\frac{1}{2}\frac{a_{33}-a_{13}}{a_{44}}\Delta_{\mathbf{x}}q+\frac{a_{33}-a_{13}}{a_{44}}2\sum_{n=0}^{\infty}(-1)^n\mathrm{e}^{-n^2\pi^2\tau}*\Delta_{\mathbf{x}}q. \tag{2.59}$$

Analyzing the same limits for the part of the solution generated by the z^2-term, we get

$$p_0^{(2h)}=-2\sum_{n=0}^{\infty}(-1)^n\mathrm{e}^{-n^2\pi^2\tau}*\Delta_{\mathbf{x}}q, \tag{2.60}$$

and for the k-term, we obtain

$$p_0^{(kh)}=\frac{k_1}{k_3}*\Delta_{\mathbf{x}}q. \tag{2.61}$$

Collecting the three formulas above and substituting them into Eqs. (2.55) and (2.56), the following complete expression for the ε^2-approximation of the fluid pressure at $z=0$ can be achieved:

$$p_0^h\approx q(\tau)+\frac{h^2}{h_*^2}p_{02}^h(\tau), \tag{2.62}$$

$$\begin{aligned} p_{02}^h = {} & \frac{1}{2}\frac{a_{33}-a_{13}}{a_{44}}\Delta_{\mathbf{x}} q(\tau) \\ & + \frac{k_1}{k_3}\int_0^\tau \Delta_{\mathbf{x}} q(\theta)\,\mathrm{d}\theta \\ & + 2\left(\frac{a_{33}-a_{13}}{a_{44}} - 1\right)\sum_{n=0}^{\infty}(-1)^n \int_0^\tau \mathrm{e}^{-n^2\pi^2(\tau-\theta)}\Delta_{\mathbf{x}} q(\theta)\,\mathrm{d}\theta. \end{aligned} \tag{2.63}$$

This is exactly the same expression obtained by Argatov and Mishuris in Argatov and Mishuris [139] in the case of transversely isotropic but homogeneous biphasic layers.

Equation (2.54) shows how to obtain the ε^2-term of the asymptotic expansion of the vertical displacement w_2 — which is actually also the only non-zero term of the approximation of w (see Eq. (2.41)) — starting from p_2 and $\mathbf{v}_1$. Sticking to the coordinate $z = 0$, the mentioned equation can be written as

$$\begin{aligned} \frac{w_0}{\varepsilon^2} \approx w_{02} = {} & \frac{1}{a_{33}}\left(\sum_{i=1}^{4}\xi_{0i}^{(M)} + \xi_0^{(2)} + \xi_0^{(k)}\right) + \frac{\Delta_{\mathbf{x}} q}{2a_{33}}\int_0^1 \mathrm{e}^{-2\gamma z} z^2\,\mathrm{d}z \\ & + \frac{a_{13}\Delta_{\mathbf{x}} q}{a_{33}a_{44}}\int_0^1 \mathrm{e}^{(\alpha_{13}-2\gamma)z}\left(\int_z^1 \mathrm{e}^{-\alpha\tilde{z}}\,\tilde{z}\,\mathrm{d}\tilde{z}\right)\mathrm{d}z. \end{aligned} \tag{2.64}$$

It is easy to notice, making use of Eq. (2.89), Table 2.1, Eqs. (2.99) and (2.107), that the only terms which do not vanish are

$$\begin{aligned} w_{02} &= \frac{\xi_{03}^{(M)} + \xi_{04}^{(M)} + \xi_{0}^{(k)} + b_{11} M_1 (\mathrm{e}^{M_1 - 2\gamma} - 1) \mathrm{e}^{A_2 \tau} * \Delta_{\mathbf{x}} q(\tau)}{a_{33}} \\ &= \frac{\mathrm{e}^{-\alpha}(\alpha^2 + 2\alpha + 2) - 2}{\alpha^3 a_{44}} \Delta_{\mathbf{x}} q \\ &+ \frac{a_{13}(\alpha_{13} - \alpha)(\mathrm{e}^{\alpha_{13} - \alpha - 2\gamma} - 1)}{\alpha a_{33} a_{44}} \Delta_{\mathbf{x}} q * \mathrm{e}^{(\alpha_{13} - \alpha)(\alpha_{13} - \alpha - 2\gamma)\tau} \\ &+ (\alpha - 2\gamma) \frac{\mathrm{e}^{-\alpha} - 1}{\alpha a_{44}} \Delta_{\mathbf{x}} q * \mathrm{e}^{\alpha(\alpha - 2\gamma)\tau} \\ &+ \frac{k_1}{a_{33} k_3} \frac{\mathrm{e}^{-\gamma_1} - 1}{\gamma_1} * \Delta_{\mathbf{x}} q(\tau). \end{aligned} \tag{2.65}$$

When all the exponents defined in Eq. (3.2) are set to zero, the previous equation takes the form

$$w_{02} = -\frac{1}{3a_{44}} \Delta_{\mathbf{x}} q(\tau) - \frac{k_1}{a_{33} k_3} \int_0^\tau \Delta_{\mathbf{x}} q(\theta) \, \mathrm{d}\theta. \tag{2.66}$$

As for Eq. (2.63), analysing the behavior of a homogeneous transversally isotropic layer, Argatov and Mishuris Argatov and Mishuris [139] gained the same result. Recovering all the original variables from Eqs. (2.30),

(2.31), and (2.32), and writing the load as $q = q(x', y', t')$, we find

$$\begin{aligned} w'_{02} = & \frac{\mathrm{e}^{-\alpha}(\alpha^2+2\alpha+2)-2}{\alpha^3 a_{44}} h^3 \Delta_{\mathbf{x}'} q \\ & + \frac{a_{13}(\alpha_{13}-\alpha)(\mathrm{e}^{\alpha_{13}-\alpha-2\gamma}-1)}{\alpha a_{44}} h k_3 \int_0^{t'} \mathrm{e}^{(\alpha_{13}-\alpha)(\alpha_{13}-\alpha-2\gamma)\frac{a_{33}k_3}{h^2}(t'-\theta)} \Delta_{\mathbf{x}'} q \, \mathrm{d}\theta \\ & + (\alpha-2\gamma)\frac{\mathrm{e}^{-\alpha}-1}{\alpha a_{44}} h k_3 a_{33} \int_0^{t'} \mathrm{e}^{\alpha(\alpha-2\gamma)\frac{a_{33}k_3}{h^2}(t'-\theta)} \Delta_{\mathbf{x}'} q \, \mathrm{d}\theta \\ & + \frac{\mathrm{e}^{-\gamma_1}-1}{\gamma_1} h k_1 \int_0^{t'} \Delta_{\mathbf{x}'} q(\theta) \, \mathrm{d}\theta. \end{aligned} \tag{2.67}$$

2.5 Numerical examples

In this Section, we present some numerical examples with the main purpose to underline the effect of the inhomogeneity to the response of the cartilage layer to an applied load. For this reason we compare every benchmark to the results obtained considering the solution by Argatov and Mishuris [139] for a transversely isotropic homogeneous (TIH) model with the same average permeability and mechanical stiffness.

The thickness of the layer is taken to be $h = 10\text{mm}$ (for the sake of easiness of scaling). The applied distributed load $q = q_{t'} q_r$ is axisymmetric with respect to the radial coordinate r, though this symmetry (not necessary from the assumptions) represents a lack of generality only for the sake of clarity in this section. It results from the product of two factors: $q_{t'} = q_{t'}(t')$ assigns the behavior in time, while $q_r = q_r(x', y') = q_r(r)$ contributes to the spacial distribution.

A total force $F = 125\text{N}$ is distributed according to the law

$$q_r(r) = \mathrm{e}^{-\left(\frac{1.73r}{10h}\right)^2} \left(\frac{10h}{1.73}\right)^2 \frac{F}{\pi}, \tag{2.68}$$

so that 100N are loaded within a radius of about $10h$.

A homogeneous and isotropic Poisson's ratio $\nu = 0$ is considered, thus the stiffness parameters (see Eq. (3.2)) result as follows:

$$\begin{cases} A_{33} = H_{A3}(z') = a_{33}\mathrm{e}^{2\gamma z'/h}, \\ A_{13} = \dfrac{\nu}{1-\nu} H_{A1}(z') = a_{13}\mathrm{e}^{\alpha_{13} z'/h}, \\ A_{44} = \dfrac{1-2\nu}{2(1-\nu)} \mathrm{H}_{A1}(z') = a_{44}\mathrm{e}^{\alpha z'/h}, \end{cases} \tag{2.69}$$

where H_{A1} and H_{A3} are respectively the planar and the vertical aggregate moduli. For the fixed ν, the behavior of A_{33} and A_{13} must be the same and only due to the variation of Ha_1, so that $\alpha_{13} = \alpha$.

The examples show a cartilage layer which is in average isotropic both in aggregate modulus and permeability. Using the operator $\langle\cdot\rangle$ to express average along the depth:

$$\begin{cases} \langle H_{A1}\rangle = \langle H_{A3}\rangle = \langle H_A\rangle = 0.5\text{MPa}, \\ \quad \langle K_1\rangle = \langle K_3\rangle = \langle K\rangle = 2\cdot 10^{-15} \dfrac{\text{m}^2}{\text{Pa s}}. \end{cases} \tag{2.70}$$

The parameter that is used both to describe the inhomogeneity of the permeability K_3 to the one of the stiffness A_{33} is γ. Anyway one can use a more intuitive quantity (called the *ratio of inhomogeneity*) R_I, which

says how much A_{33} grows from the articular surface to the bone (i.e., $e^{2\gamma}$) and at the same time the ratio of K_3 at $z' = 0$ and at $z' = h$. Thus, we put

$$\gamma = 0.5 \log R_I. \tag{2.71}$$

In order to study the effects of the inhomogeneity, we set the remaining parameters as functions of the same R_I as follows:

$$\begin{cases} \gamma_1 = 2 \log R_I, \\ \alpha = \alpha_{13} = 0.7 \log R_I. \end{cases} \tag{2.72}$$

As shown by Federico and Herzog [68] via a micromechanical approach, the anisotropy of permeability can be explained through the fact that the collagen fibers, whose statistical orientation varies with the depth, are impermeable. Consequently, being the fibers nearly parallel to the surface and perpendicular to the tidemark, $K_1 > K_3$ for small z' and vice versa. Since the same fibers are known to be responsible also for the mechanical properties, and particularly for the anisotropy and inhomogeneity of the cartilage stiffness (e.g. Federico et al. [67]), it is expected that $H_{A1} > H_{A3}$ in the upper part of the layer, conversely in the lower one. The achievement of these features are the reason of the choice of the parameters above. For instance, the effect of this characterization is visualized in Fig. 2.2 for $R_I = 3$, where K^{iso} and H_A^{iso} (see Fig. 2.2.b and Fig. 2.2.d) are the equivalent inhomogeneous isotropic aggregate modulus

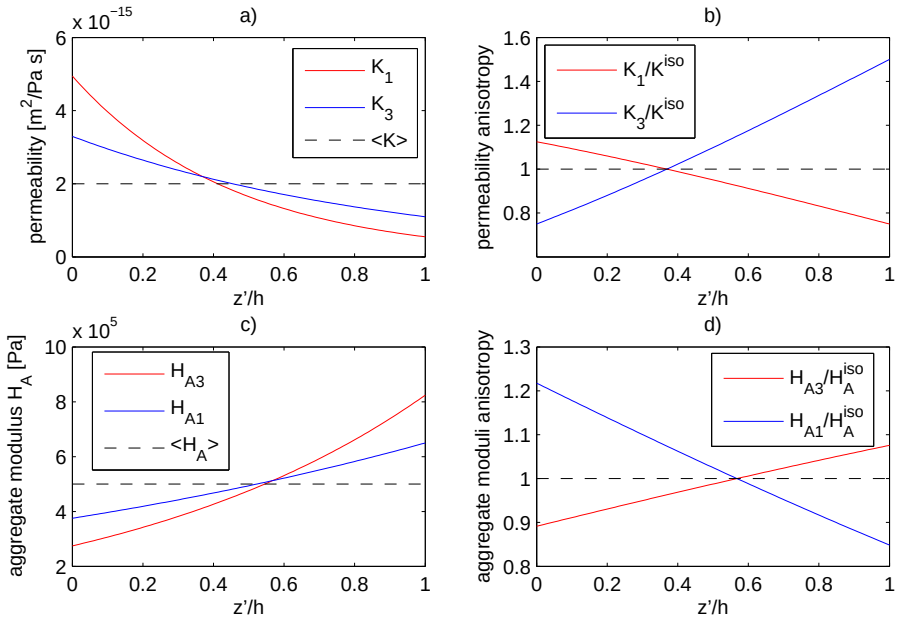

FIGURE 2.2: Permeability and aggregate modulus versus the isotropic homogeneous ones plotted along the depth z'/h for an *inhomogeneity ratio* $R_I = 3$ in a) and c) following the settings of Eq. (2.70), (2.71) and (2.72); Plots b) and d) illustrate the descending anisotropy as ratios between those quantities and the equivalent inhomogeneous isotropic ones.

and permeability defined as

$$\begin{cases} K^{\text{iso}}(z') = \dfrac{2}{3}K_1 + \dfrac{1}{3}K_3, \\ H_A^{\text{iso}}(z') = \dfrac{2}{3}H_{A1} + \dfrac{1}{3}H_{A3}. \end{cases} \tag{2.73}$$

According to Eq. (2.67), in the first place we show the behavior of the present cartilage model for a constant load ($q_{t'} = 1$) applied for 1200s,

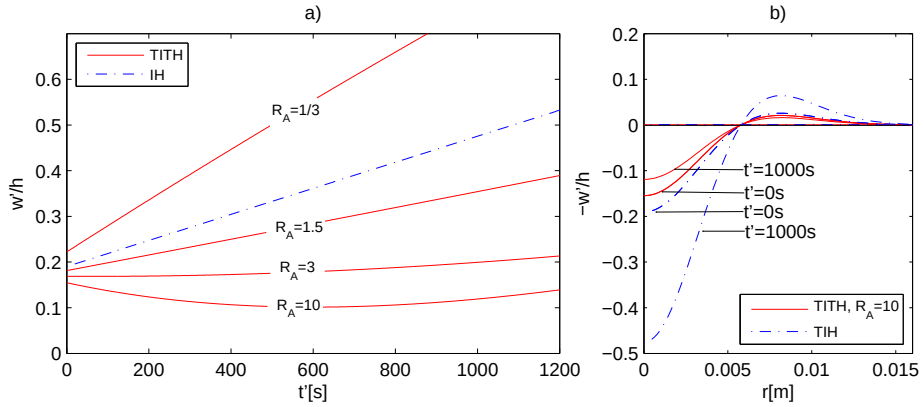

FIGURE 2.3: Vertical displacement of the TITH layer surface under a constant load and comparison with an IH layer behavior: a) is the evolution in time at $r = 0$; b) shows the deformation profile along the radius for different times.

smaller than the characteristic time $t' = h^2/(a_{33}k_3)$ for which the solution is valid. Both from Fig. 2.3.a and Fig. 2.3.b it is observable that R_I strongly influences the response of the structure. In particular, while in the case of a homogeneous isotropic layer the deformation increases for a constant load, above a certain value of R_I, which depends on the parameters settings, a phenomenon of swelling appears during the initial phase. It derives (see the second and third addends in Eq. (2.67)) from the contribution of K_3, effect that vanishes in the IH case. Fig. 2.3.b draws attention to the profile of deformation of the contact surface. The obtained asymptotic solution provides that w' depends only on $\Delta_{\mathbf{x}'}q$, so that, since for our loading condition its zeroes remain fixed (see Eq. (2.68)), every benchmark calculated in this section implies a homothetic deformation profile.

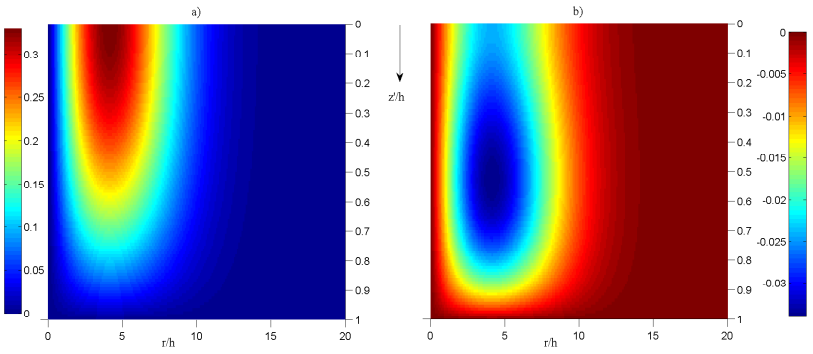

FIGURE 2.4: a) Lateral displacement of a TITH layer with $R_I = 3$ under constant load at $t' = 0$; b) Difference of lateral displacement between a TITH layer with $R_I = 3$ and an IH one under constant load at $t' = 0$.

Through Eq. (2.42) the lateral displacements are achieved. In Fig. 2.4.a, the axisymmetric v' is plotted under a constant load from $r = 0$ to $r = 20h$ at $t' = 0s$. The highest displacement is obtained at the load surface at $r \approx 4h$ with a value of $v' \approx 0.33h$ while the base is constrained (see Eq. (2.24)). In Fig. 2.4.b, the difference between the solution for a TITH layer with $R_I = 3$ and the one for a IH layer is measured. The maximum difference appears at the same $r \approx 4h$ but $z' \approx 0.5h$, and is about $0.034h$, so that, in terms of lateral displacements, the TITH structure with $R_I = 3$ shows to deform less than the equivalent IH one. In Fig. 2.4, the instantaneous response is calculated, and one can notice how (although the surface displacements can appear qualitatively similar at the load surface (Fig. 2.3.b) and the same fittings are eventually possible both through a homogeneous and inhomogeneous model calibrating the material parameters) remarkable differences are returned between the two if light needs to be shed inside the layer.

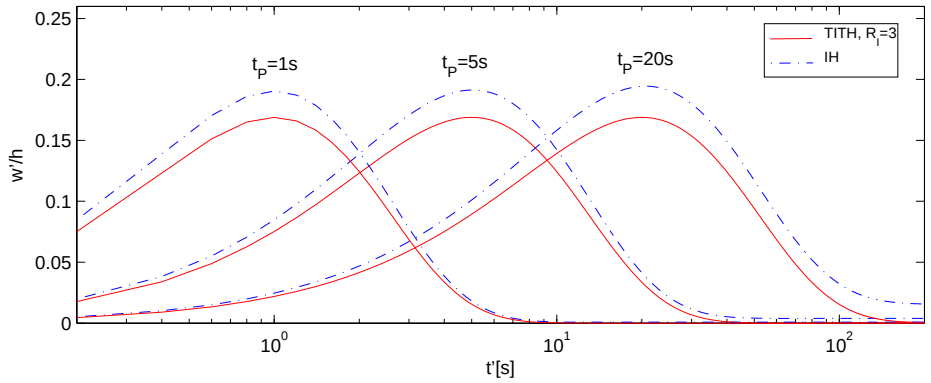

FIGURE 2.5: Displacement at $r = 0$. Peaks of the three considered loads: 1s, 5s, 20s. The representation timescale is logarithmic. The TITH has $R_I = 3$ and does not present significant residual displacements at $t' = 200s$. Its peak displacements verify at the respective t_P and are about $0.17h$, while the peaks for IH are $0.19h$.

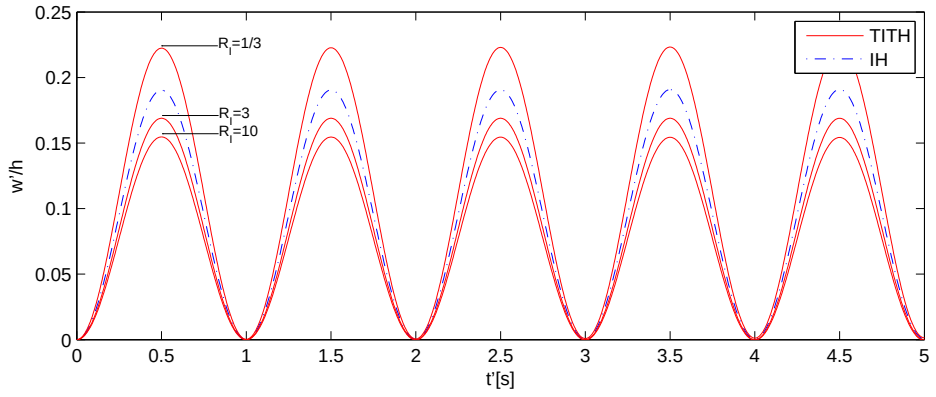

FIGURE 2.6: Vertical displacement at $r = 0$ under a sinusoidal load oscillating with a frequency of 1Hz. Three different inhomogeneous layers ($R_I = 1/3, 3, 10$) are compared to an IH one.

The second case that we consider deals with a load which reaches its peak at $t' = t_P$. Successively it decreases to 0 asymptotically following the law:

$$q_{t'} = \frac{t' \mathrm{e}^{-(\frac{t'}{t_P}+1)}}{t_P}. \tag{2.74}$$

The displacement of the point $r = 0$ is depicted in Fig. 2.5 for three different values of t_P for the first 200s. The peaks of the displacement are the same in the three cases and happen approximately at the respective t_P. As in the case of a constant load, the deformation at $r = 0$ becomes smaller for inhomogeneities with $R_I > 1$. The difference between the IH model and the TITH ($R_I = 3$) model consists mainly in the behavior at large t'. While the transversely homogeneous layer returns to the undeformed configuration after the load removal, the homogeneous solution presents a residual deformation that depends on t_P, that is on the rate with which the load is applied.

Finally, in Fig. 2.6 the effect on $w'|_{r=0}$ of a sinusoidal load is plotted. The frequency applied is considered to be 1Hz, similar to the one that can occur to a knee articular cartilage due to walking. As expected, since the period of 1s is small in comparison to the characteristic time, the short term difference between differently inhomogeneous layers is exclusively in terms of amplitude and no residual displacements are accumulated for next cycles. The structure deforms as a monophasic elastic one; yet again a positive R_I produces a *stiffer* response, while a negative one vice versa.

2.6 Remarks

An analytical approach is provided for solution of the deformation problem of a TITH biphasic thin layer. The mathematical analysis is conducted by use of Laplace transformation and asymptotic analysis. The leading terms of the displacement and fluid pressure fields are retrieved through the solution of ordinary differential equations. Such equations are made particularly simple thanks to the assumption of exponential in-depth variation of the solid matrix elastic stiffness and permeability with the only restriction of keeping the product $k_3 A_{33}$ constant along the layer transverse direction. This particular setting appears reasonable since experimental investigations on articular cartilage show that the aggregate modulus, contrarily to the permeability, decreases toward the subchondral bone (see Wang et al. [143], Maroudas et al. [144]). The scope of the present work is presenting an explicit form for the deformation of the external cartilage surface which can be straightforwardly applied for solving contact problems. It is reached through the formula in Eq. (2.67). In addition to the contribution of A_{33}, A_{44}, k_1 and k_3 found by Argatov and Mishuris [139], the one of A_{13} is shown, other than the effects of the variation parameters α_{ij} and γ_i (see their definitions in Eq. (3.2)). As discussed in Section 1.1, the role of inhomogeneity and anisotropy in affecting the internal state of the cartilage layer during loading encouraged many authors to develop fully 3D models for its mechanical analysis. However their applicability for the study of contact problems, due to the large difference in scales between the thin tissue and the bones interacting along the articular joint may result arduously suitable because of

the deriving numerical problems, possibly obligating to use homogeneous elements as interphases. The simplicity of Eq. (2.67), on the opposite, suggests that the same constitutive equations can be used both for an insight into the layer (see Fig. 2.4), for instance for experimental investigations, and for a large scale contact problems. The full-thickness layer can finally be substituted by a zero-thickness one through transmission conditions. Eventually an asymptotic-based finite element can be implemented for assessing patient-specific problems for real diathrodial joints and complex geometries, once the material parameters are experimentally estimated. Only in sight of the application to the contact problem in Chapter 3 the results are presented extensively on the contact surface, while, for the reader who desired to obtain the full-depth solution, it would be enough to remove the restriction on the z-coordinate for the Laplace inversion shown in the Appendices.

2.A Solution to Eq. (2.51) for the right-hand sides $\Upsilon_i(s,z)$, $i=1,2,3,4$

Let us consider the equation

$$\frac{\partial^2 P}{\partial z^2} - 2\gamma\frac{\partial P}{\partial z} - sP = s\Delta_{\mathbf{x}} Q \mathrm{e}^{Mz}(b_1 z + b_0), \tag{2.75}$$

with the boundary conditions $\frac{\partial P}{\partial z} = 0$ at $z = 0$ and $z = 1$. Its general solution, obtained through Eq. (2.53) and the method of undetermined

coefficients, is given by

$$P = \mathrm{e}^{\gamma z}(C_1 \sinh \sigma z + C_2 \cosh \sigma z) + \mathrm{e}^{Mz}\left(\frac{b_1}{A-s}z + \frac{b_0}{A-s} - \frac{2b_1(M-\gamma)}{(A-s)^2}\right) s\Delta_{\mathbf{x}}Q, \tag{2.76}$$

where $A = M(M-2\gamma)$. The coefficients $C_1(s)$ and $C_2(s)$ are set in order to respect the two boundary conditions mentioned above, and then arise from a linear system of two equations, so that

$$\begin{aligned}\frac{P}{\Delta_{\mathbf{x}}Q} = \frac{\mathrm{e}^{\gamma z}}{\sinh \sigma}\Bigg\{\left(\frac{Mb_o + b_1}{A-s} - \frac{2b_1M(M-\gamma)}{(A-s)^2}\right)\big[\cosh \sigma z(\gamma \sinh \sigma + \sigma \cosh \sigma - \mathrm{e}^{M-\gamma}\sigma) \\ + \sinh \sigma z(\gamma \mathrm{e}^{M-\gamma} - \gamma \cosh \sigma - \sigma \sinh \sigma)\big] + \frac{Mb_1}{A-s}\mathrm{e}^{M-\gamma}(\gamma \sinh \sigma z - \sigma \cosh \sigma z)\Bigg\} \\ + \mathrm{e}^{Mz}\left(\frac{b_1}{A-s}z + \frac{b_0}{A-s} - \frac{2b_1(M-\gamma)}{(A-s)^2}\right) s.\end{aligned} \tag{2.77}$$

At this point, only for the sake of brevity, we restrict our solution to the load application surface situated at $z = 0$. We define $P_0 = P|_{z=0}$ and obtain

$$\begin{aligned}\frac{P_0}{\Delta_{\mathbf{x}}Q} = \frac{1}{\sinh \sigma}\Bigg\{\left(\frac{Mb_o + b_1}{A-s} - \frac{2b_1M(M-\gamma)}{(A-s)^2}\right)\left(\gamma \sinh \sigma + \sigma \cosh \sigma - \sigma \mathrm{e}^{M-\gamma}\right) \\ - \frac{Mb_1}{A-s}\sigma \mathrm{e}^{M-\gamma}\Bigg\} + \frac{sb_0}{A-s} - \frac{2b_1(M-\gamma)s}{(A-s)^2}.\end{aligned} \tag{2.78}$$

The Laplace inversion of $f(s)$ can be done via contour integration as follows:

$$\mathcal{L}\{fs\}^{-1} = \frac{1}{2\pi \mathrm{i}}\int_{c-\mathrm{i}\infty}^{c+\mathrm{i}\infty} f(s)\mathrm{e}^{s\tau}\,\mathrm{d}s \tag{2.79}$$

with $c \in \mathbb{R}$ greater than the real part of every singularity of $f(s)$. If the integral converges for $|s| \to \infty$ in the half-plane $\mathrm{Re}(s) < c$ and the singularities lie on the real axis, then it can be reduced to

$$\mathcal{L}\left\{f(s)\right\}^{-1}(\tau) = -\frac{1}{2\pi \mathrm{i}} \int_{-\infty}^{c} f(s^+)\mathrm{e}^{s^+\tau}\,\mathrm{d}s^+ - \frac{1}{2\pi \mathrm{i}} \int_{-\infty}^{c} f(s^-)\mathrm{e}^{s^-\tau}\,\mathrm{d}s^- + \sum_{j=1}^{N} \mathrm{Res}\left\{f(s)\mathrm{e}^{s\tau}; s_j\right\}, \tag{2.80}$$

in which N is the number of the singularities located at s_j, s^+ means that the path of integration is taken above the real axis, s^- vice versa. It is the case of $\Omega(s)$ (see Eq. (2.83)), for which it is also easy to show the two integrals on the right-hand side eliminate each other, so that the inverse Laplace transform results simply the sum of the residues.

Here, we use the complex residue of a function $f(s)$ in a pole $s = s_j$

$$\mathrm{Res}\left\{f(s)\mathrm{e}^{s\tau}; s_j\right\} = \frac{1}{2\pi \mathrm{i}} \oint_{\Omega_j} f\,\mathrm{d}s, \tag{2.81}$$

where the contour Ω_j in the complex plane is taken which includes s_j and no other poles.

The inverse Laplace transformation of Eq.(2.78) needs to be conducted on $P_0(s)$ in order to find $p_0(\tau)$. For this purpose we invert the ratio $\frac{P_0}{\Delta_{\mathbf{x}} Q}$ and at the end, exploiting the convolution theorem, convolve the result with $\Delta_{\mathbf{x}} q(\tau)$. While the inversion of the terms outside the curly brackets is trivial, the ones inside divided by $\sinh \sigma$ can be inverted making use of the residue theorem. The poles of such functions are in $s = A$ and

where $\sinh\sigma$ vanishes. This occurs when $\sigma = n\pi\mathrm{i}$, namely in $s = s_n = -(\gamma^2 + n^2\pi^2)$ $(n = 0, 1, ..., +\infty)$, so that

$$\mathcal{L}\left\{\frac{P_0}{\Delta_{\mathbf{x}}Q}\right\}^{-1} = \mathrm{Res}\left\{\mathrm{e}^{s\tau}\Omega(s); s = A\right\} + \sum_{n=0}^{\infty}\mathrm{Res}\left\{\mathrm{e}^{s\tau}\Omega(s); s = s_n\right\} - b_0\left(A\mathrm{e}^{A\tau} + \delta(\tau)\right) - 2b_1(M-\gamma)\mathrm{e}^{A\tau}(1 + A\tau), \tag{2.82}$$

where $\delta(t)$ is Dirac's delta function and

$$\Omega(s) = \frac{1}{\sinh\sigma}\left\{-\frac{Mb_1}{A-s}\sigma\mathrm{e}^{M-\gamma} + \left(\frac{Mb_o + b_1}{A-s} - \frac{2b_1M(M-\gamma)}{(A-s)^2}\right)\left(\gamma\sinh\sigma + \sigma\cosh\sigma - \sigma\mathrm{e}^{M-\gamma}\right)\right\} \tag{2.83}$$

It results that

$$\mathrm{Res}\left\{\mathrm{e}^{s\tau}\Omega(s); s = A\right\} = \mathrm{e}^{A\tau}Ab_0 + 2b_1(M-\gamma)\mathrm{e}^{A\tau}(1 + A\tau). \tag{2.84}$$

If L_n is defined as $L_n = ((M-\gamma)^2 + n^2\pi^2)$, the residue in s_n is written as

$$\mathrm{Res}\left\{\mathrm{e}^{s\tau}\Omega(s); s = s_n\right\} = \left\{\left[\frac{Mb_o + b_1}{L_n} - \frac{2b_1M(M-\gamma)}{L_n^2}\right]\left((-1)^n\mathrm{e}^{M-\gamma} - 1\right) + \frac{Mb_1}{L_n}(-1)^n\mathrm{e}^{M-\gamma}\right\} 2n^2\pi^2\mathrm{e}^{-(\gamma^2+n^2\pi^2)\tau}, \tag{2.85}$$

which vanishes at $s = 0$ ($n = 0$). Making use of the convolution theorem and collecting the expressions (2.84) and (2.85), Eq. (2.82) gives

$$p_{0i}^{(M)}(\tau) = -b_{0i}\Delta_{\mathbf{x}}q(\tau) + \sum_{n=1}^{\infty} \mathrm{Res}\left\{\mathrm{e}^{s\tau}\Omega_i^{(M)}(s); s_n\right\} * \Delta_{\mathbf{x}}q(\tau), \tag{2.86}$$

where the index i and the superscript (M) have the same meaning as in Eq. (2.51). Here, a convolution in time $f * g$ between two functions is defined as

$$(f * g)(\tau) = \int_{0^-}^{\tau} f(\theta)g(\tau - \theta)\,\mathrm{d}\theta = \int_{0}^{\tau} g(\theta)f(\tau - \theta)\,\mathrm{d}\theta, \tag{2.87}$$

as in our case all the variables are set to 0 in $\tau < 0$.

Now we proceed to evaluate $\Xi_0 = \mathcal{L}\{\xi\}^{-1}|_{z=0} = -\int_0^1 P\mathrm{e}^{-2\gamma z}\,\mathrm{d}z$, where P is defined in Eq. (2.77). In this way, we obtain

$$\begin{aligned}\frac{\Xi_0}{\Delta_{\mathbf{x}}Q} = &-\mathrm{e}^{M-2\gamma}\left(\frac{Mb_0 + (M+1)b_1}{s - A} + \frac{2b_1M(M-\gamma)}{(s-A)^2}\right) \\ &+ \left(\frac{Mb_0 + b_1}{s - A} + \frac{2b_1M(M-\gamma)}{(s-A)^2}\right) + \frac{s}{s-A}\frac{b_1}{M-2\gamma}\mathrm{e}^{M-2\gamma} \\ &+ \frac{\mathrm{e}^{M-2\gamma} - 1}{M - 2\gamma}\left[\frac{s}{s-A}b_0 + \frac{2sb_1(M-\gamma)}{(s-A)^2} - \frac{sb_1}{(M-2\gamma)(s-A)}\right].\end{aligned} \tag{2.88}$$

Passing to inverse Laplace transforms and convolving by $\Delta_{\mathbf{x}} q(\tau)$, each i-th term of $\xi_0^{(M)} = \sum_{i=1}^{4} \xi_{0i}^{(M)}$ results to be

$$\begin{aligned}\xi_{0i}^{(M)}(\tau) = &\left[b_{0i} \frac{\mathrm{e}^{M_i - 2\gamma} - 1}{M_i - 2\gamma} + b_{1i} \frac{\mathrm{e}^{M_i - 2\gamma}(M_i - 2\gamma - 1) + 1}{(M_i - 2\gamma)^2} \right] \Delta_{\mathbf{x}} q(\tau) \\ &+ b_{1i} M_i (\mathrm{e}^{M_i - 2\gamma} - 1) \mathrm{e}^{A_i \tau} * \Delta_{\mathbf{x}} q(\tau).\end{aligned} \tag{2.89}$$

2.B Solution to Eq. (2.51) for the right-hand sides $\Upsilon_5(s, z)$

The equation, coupled with the usual boundary conditions on the derivative of P, is

$$\frac{\partial^2 P}{\partial z^2} - 2\gamma \frac{\partial P}{\partial z} - sP = -\frac{z^2}{2} s \Delta_{\mathbf{x}} Q, \tag{2.90}$$

and its solution is given by

$$P = \mathrm{e}^{\gamma z}(C_1(s) \sinh \sigma z + C_2(s) \cosh \sigma z) + \left(\frac{z^2}{2} - \frac{2\gamma z}{s} + \frac{1}{s} + \frac{4\gamma^2}{s^2} \right) \Delta_{\mathbf{x}} Q, \tag{2.91}$$

where

$$C_1(s) = \frac{\frac{2\gamma}{s}(\gamma \cosh \sigma + \sigma \sinh \sigma - \gamma \mathrm{e}^{-\gamma}) + \gamma \mathrm{e}^{-\gamma}}{s \sinh \sigma} \Delta_{\mathbf{x}} Q, \tag{2.92}$$

$$C_2(s) = \frac{\frac{2\gamma}{s}(\sigma \mathrm{e}^{-\gamma} - \gamma \sinh \sigma - \sigma \cosh \sigma) - \sigma \mathrm{e}^{-\gamma}}{s \sinh \sigma} \Delta_{\mathbf{x}} Q. \tag{2.93}$$

Complying exclusively with the search for $P_0 = P|_{z=0}$, the next function must be inverted to give

$$\begin{aligned}\frac{P_0}{\Delta_{\mathbf{x}} Q} &= \frac{\frac{2\gamma}{s}(\sigma \mathrm{e}^{-\gamma} - \gamma \sinh\sigma - \sigma\cosh\sigma) - \sigma \mathrm{e}^{-\gamma}}{s\sinh\sigma} + \frac{1}{s} + \frac{4\gamma^2}{s^2} \\ &= \Omega(s) + \frac{1}{s} + \frac{4\gamma^2}{s^2},\end{aligned} \tag{2.94}$$

with the self-evident definition of $\Omega(s)$. The transform above has non-zero residues at $s = 0$ and at $s = s_n$. Similarly to what explained in the previous paragraph, the inverse Lalace transform of $\Omega(s)$ can be executed only in terms of residues

$$\mathcal{L}\left\{\frac{P_0}{\Delta_{\mathbf{x}} Q}\right\}^{-1} = \mathrm{Res}\left\{\Omega(s)\mathrm{e}^{s\tau}; 0\right\} + \sum_{n=0}^{\infty} \mathrm{Res}\left\{\Omega(s); s_n\right\} + 1 + 4\gamma^2\tau. \tag{2.95}$$

On the other hand, it occurs that $\mathrm{Res}\left\{\Omega(s); 0\right\} = -1 - 4\gamma^2 t$. It remains to compute the residue at $s = s_n$:

$$\mathrm{Res}\left\{\mathrm{e}^{s\tau}\Omega(s); s_n\right\} = \left[2\gamma\frac{1-(-1)^n\mathrm{e}^{-\gamma}}{(\gamma^2+n^2\pi^2)^2} - \frac{(-1)^n\mathrm{e}^{-\gamma}}{\gamma^2+n^2\pi^2}\right] 2n^2\pi^2\mathrm{e}^{-(\gamma^2+n^2\pi^2)\tau}. \tag{2.96}$$

Substituting this results into Eq. (2.95) and taking advantage from the convolution theorem, it follows that

$$p_0^{(2)}(\tau) = \sum_{n=1}^{\infty} \mathrm{Res}\left\{\Omega^{(2)}(s)\mathrm{e}^{s\tau}; s_n\right\} * \Delta_{\mathbf{x}} q(\tau), \tag{2.97}$$

where we use the superscript (2) to signify z^2-term. With respect to Ξ_0, the integration of Eq. (2.91) along the layer depth yields

$$\begin{aligned}\frac{\Xi_0}{\Delta_{\mathbf{x}}Q} = &-\frac{C_1(s)}{\Delta_{\mathbf{x}}Q}\int_0^1 \mathrm{e}^{-\gamma z}\sinh\sigma z\,\mathrm{d}z - \frac{C_2(s)}{\Delta_{\mathbf{x}}Q}\int_0^1 \mathrm{e}^{-\gamma z}\cosh\sigma z\,\mathrm{d}z \\ &- \int_0^1 \left(\frac{z^2}{2} - \frac{2\gamma z}{s} + \frac{1}{s} + \frac{4\gamma^2}{s^2}\right)\mathrm{d}z.\end{aligned} \tag{2.98}$$

This, after substituting the costants of Eq. (2.93) leads simply to

$$\xi_0^{(2)}(\tau) = -\Delta_{\mathbf{x}}q(\tau)\int_0^1 \mathrm{e}^{-2\gamma z}\frac{z^2}{2}\,\mathrm{d}z. \tag{2.99}$$

2.C Solution to Eq. (2.51) for the right-hand sides $\Upsilon_5(s,z)$

The function P, regarding the k-term in Eq. (2.51), can be directly recovered from the solution of Eq. (2.76), setting b_1 to zero, $b_0 = -\frac{1}{s}\frac{k_1}{k_3}$, $M = 2\gamma - \gamma_1$ and $A = -\gamma_1(2\gamma - \gamma_1)$. Thus, we will have

$$\begin{aligned}\frac{P}{\Delta_{\mathbf{x}}Q} = &\frac{\mathrm{e}^{\gamma z}Mb_0}{(A-s)\sinh\sigma}\left\{\cosh\sigma z(\gamma\sinh\sigma + \sigma\cosh\sigma - \sigma\mathrm{e}^{M-\gamma})\right. \\ &\left. + \sinh\sigma z(\gamma\mathrm{e}^{M-\gamma} - \gamma\cosh\sigma - \sigma\sinh\sigma)\right\} + \mathrm{e}^{\gamma z}\frac{b_0}{A-s}.\end{aligned} \tag{2.100}$$

On the load application surface, we have

$$\begin{aligned}\frac{P_0}{\Delta_{\mathbf{x}}Q} &= \frac{M\frac{k_1}{k_3}}{s(s-A)\sinh\sigma}(\gamma\sinh\sigma+\sigma\cosh\sigma-\gamma\mathrm{e}^{M-\gamma})+\frac{k_1}{k_3}\frac{1}{s-A}\\ &= \Omega(s)+\frac{k_1}{k_3}\frac{1}{s-A},\end{aligned} \tag{2.101}$$

where, again, the meaning of $\Omega(s)$ is clear. The inverse Laplace transform of $\Omega(s)$ is calculated via residue theorem as the sum of the residues of $\Omega(s)\mathrm{e}^{st}$ at the singularities, which are situated at 0, A and s_n.

$$\mathrm{Res}\left\{\Omega(s)\mathrm{e}^{st};0\right\} = \frac{\gamma\frac{k_1}{k_3}}{(M-2\gamma)\sinh\gamma}(\mathrm{e}^{M-\gamma}-\mathrm{e}^{\gamma}), \tag{2.102}$$

$$\mathrm{Res}\left\{\Omega(s)\mathrm{e}^{s\tau};A\right\} = -\frac{k_1}{k_3}\mathrm{e}^{A\tau}, \tag{2.103}$$

$$\mathrm{Res}\left\{\Omega(s)\mathrm{e}^{s\tau};s_n\right\} = \frac{M(1-(-1)^n\mathrm{e}^{M-\gamma})}{((M-\gamma)^2+n^2\pi^2)\,(\gamma^2+n^2\pi^2)}2n^2\pi^2\mathrm{e}^{-(\gamma^2+n^2\pi^2)\tau}. \tag{2.104}$$

Connoting with (k) the elements arising from the k-terms, the complete inverse Laplace transform gives

$$p_0(\tau) = \frac{\gamma\frac{k_1}{k_3}\mathrm{e}^{\gamma}}{\gamma_1\sinh\gamma}(1-\mathrm{e}^{-\gamma_1})*\Delta_{\mathbf{x}}q(\tau)+\sum_{n=1}^{\infty}\mathrm{Res}\left\{\mathrm{e}^{s\tau}\Omega^{(k)}(s);s_n\right\}*\Delta_{\mathbf{x}}q(\tau). \tag{2.105}$$

The function $\Xi_0(s)$ is (using the same substitution as explained for the pressure) simply recovered from Eq. (2.88) and is

$$\frac{\Xi_0(s)}{\Delta_{\mathbf{x}}Q} = \frac{k_1}{k_3}\left(\mathrm{e}^{-\gamma_1}-1\right)\left[\frac{2\gamma-\gamma_1}{s(s-A)}+\frac{1}{\gamma_1(s-A)}\right]. \tag{2.106}$$

Inverting this Laplace transform and using the convolution theorem, finally we obtain

$$\xi_0^{(k)}(\tau) = \frac{k_1}{k_3} \frac{\mathrm{e}^{-\gamma_1} - 1}{\gamma_1} * \Delta_{\mathbf{x}} q(\tau). \tag{2.107}$$

Chapter 3

Three-dimensional contact of transversely isotropic transversely homogeneous cartilage layers: A closed-form solution

This Chapter adds to the discussion about how to analytically solve the contact problem of two biphasic layers attached onto rigid substrates. It is done using an asymptotic approach which enables to retrieve closed-form solutions with the advantage of easily analyzable formulas (Argatov and Mishuris [145]). The studies published so far attain to the cartilagineous material modeled first as isotropic homogeneous (Ateshian

et al. [52]), later as homogeneous but transversely isotropic (Argatov and Mishuris [139]). Speaking of the utilized geometry, the solution provided in Ateshian et al. [52] regarded identical spherical surfaces and it was extended to two different radii spheres in Wu et al. [53, 146]. Further advances were aimed in Argatov and Mishuris [55] by the introduction of elliptic paraboloids resulting in elliptical contact areas. Nevertheless the importance of inhomogeneity in the material property distribution across the thickness has been widely explored as a crucial factor in improving superficial fluid support, thus protecting the tissue from damage (Krishnan et al. [66], Federico and Herzog [68]). This was the reason for our recent study Vitucci et al. [72], summarized in Chapter 3, where a special exponential-type inhomogeneity was introduced.

The solution to the contact problem is derived in Sec.3.2 and some numerical benchmarks are illustrated in Sec.3.3. The physical bounds for the model parameters are discussed. Geometry, solicitations and material stiffness and permeability are assigned trying to be as realistic as possible in the framework of the model by ample use of available publications. Two load conditions are exemplified, a constant load and a sinusoidal one. In particular, by means of the retrieved formulas, the utilized contact radii are extracted from the experimental measurements on human tibiofemoral joints provided Hosseini et al. [147]. In Sec.3.4 we draw our conclusions on some aspects which suggest how inhomogeneity turns favorable for this specific biological tissue and on the applicability and limitations of the current model. The need for data which can reveal crucial for mechanics scientists in order to provide effective diagnosis tools are also remarked.

3.1 Model and statement of the contact problem

The contact of thin cartilaginous layers can not be tackled using an Hertzian approach mainly for two reasons: the material is not constituted of a single phase and, perhaps even more critically, the assumption of contacting half spaces is dramatically violated. Because of that, the inquiry for analytical solutions is commonly responded by using transmission conditions based on the simplification that the layer thickness is asymptotically small and its stiffness is much smaller than the underlying bone. The procedure, surveyed by Argatov and Mishuris [145], is regardless of the constitutive laws of the material and of the contact model and consists in: first solving the deformation problem for an infinitely extended thin layer to which the same boundary conditions are assigned on the two surfaces but the load kept general as in Barry and Holmes [148]; then making use of it for coupling two layers in contact as in Ateshian et al. [52], Yang [149].

In our recent work Vitucci et al. [72], the deformation problem for a thin biphasic transversely isotropic, transversely homogeneous (TITH) biphasic layer was studied. An infinitely extended thin layer, firmly attached along one face, was loaded perpendicularly to the opposite one. The fluid flow, whose filtration through the porous matrix was regulated by the three-dimensional form of Darcy's law, was constrained by the two layer faces by imposing null fluid pressure derivative there. At the top surface the absence of friction was enforced via setting zero shear strain

in the solid matrix. The initial conditions on deformation and fluid pressure until the moment when the load is applied were set also to zero. The solid matrix was considered linear elastic and the interstitial fluid inviscid, given that the low permeability causes the friction drag to be dominant with respect to the viscous flow: due to the low permeability of the tissue, the relative velocity of the fluid through the solid structure makes the inertia terms play no role in the deformation process under common solicitations as justified also in Holzapfel and Ogden [150], Klika et al. [151] . The governing partial differential equations were thus led back to the classical mixture theory for biphasic poroelasticity as originally derived in Mow et al. [50]. The solid matrix constitutive law is described by the stiffness matrix

$$\mathbf{A}(z) = \begin{bmatrix} A_{11} & A_{12} & A_{13} & & & & \\ A_{12} & A_{11} & A_{13} & & & & \\ A_{13} & A_{13} & A_{33} & & & & \\ & & & 2A_{44} & & & \\ & & & & 2A_{44} & & \\ & & & & & 2A_{66} & \end{bmatrix}, \tag{3.1}$$

whose components vary through the local depth-coordinate $z \in [0, 1]$ from the surface to the substrate (see Sec.3.1). Also the diagonal permeability tensor was considered TITH of components $\mathrm{diag}(\mathbf{K}(z)) = [K_1, K_1, K_3]$. As discussed in detail in Section 2.4, a special exponential inhomogeneity

was assumed:

$$\begin{aligned} A_{33} &= a_{33}\mathrm{e}^{2\gamma z}, \quad A_{44} = a_{44}\mathrm{e}^{\alpha z}, \quad A_{13} = a_{13}\mathrm{e}^{\alpha_{13} z}, \\ K_3 &= k_3\mathrm{e}^{-2\gamma z}, \quad K_1 = k_1\mathrm{e}^{-\gamma_1 z}. \end{aligned} \tag{3.2}$$

According to it, in spite of an arbitrary exponential variation of every component, A_{33} and K_3 are linked through $\gamma > 0$, thus let respectively increase and decrease of the same ratio across the thickness. The derived asymptotic relation between the contact pressure P and the surface layer displacement field w, taken positive in compression, is expressed via a sum of convolutions in time t as

$$w = \bar{\alpha}_0 \Delta P + \bar{\alpha}_1 \int_0^t \mathrm{e}^{\bar{\beta}_1(t-\theta)} \Delta P \, \mathrm{d}\theta + \bar{\alpha}_2 \int_0^t \mathrm{e}^{\bar{\beta}_2(t-\theta)} \Delta P \, \mathrm{d}\theta + \bar{\alpha}_3 \int_0^t \Delta P(\theta) \, \mathrm{d}\theta, \tag{3.3}$$

where the operator Δ represents the Laplacian in the plane orthogonal to z. The expression of the coefficients in Eq. (3.3) as functions of the TITH biphasic material parameters of Eq. (3.2) are displayed in the Table. Such

$\bar{\alpha}_0$	$\dfrac{2-\mathrm{e}^{-\alpha}(\alpha^2+2\alpha+2)}{\alpha^3 a_{44}} h^3$	$\bar{\alpha}_3$	$\dfrac{1-\mathrm{e}^{-\gamma_1}}{\gamma_1} h k_1$
$\bar{\alpha}_1$	$\dfrac{a_{13}(\alpha_{13}-\alpha)(1-\mathrm{e}^{\alpha_{13}-\alpha-2\gamma})}{\alpha a_{44}} h k_3$	$\bar{\beta}_1$	$(\alpha_{13}-\alpha)(\alpha_{13}-\alpha-2\gamma)\dfrac{a_{33}k_3}{h^2}$
$\bar{\alpha}_2$	$(\alpha-2\gamma)\dfrac{1-\mathrm{e}^{-\alpha}}{\alpha a_{44}} h k_3 a_{33}$	$\bar{\beta}_2$	$\alpha(\alpha-2\gamma)\dfrac{a_{33}k_3}{h^2}$

TABLE 3.1: Coefficients of the pressure-displacement asymptotic relation in Eq. (3.3) as functions of the material parameters of Eq. (3.2) as derived in Vitucci et al. [72].

closed-form asymptotic solution was obtained under the conditions that the characteristic scale of the phenomenon along the tissue was much bigger than the thickness h itself and that the observed time t was much smaller than the hydrogel characteristic time $\tau_{\text{gel}} = h^2/(A_{33}K_3)$. The solution represents the second-order non-trivial terms of the asymptotic expansion of the displacement field with relative accuracy $\mathcal{O}(h^2/a_*^2)$, where a_* is a length characterizing the loaded area. Looking at Eq.(3.3), however, shows that the problem, though not fully dynamic, remains time-dependent in a way similar to viscoelasticity, which was indeed one of the first models of cartilage in Kempson et al. [152] but that could not distinguish between the stresses of the single phases as discussed by Mak [153].

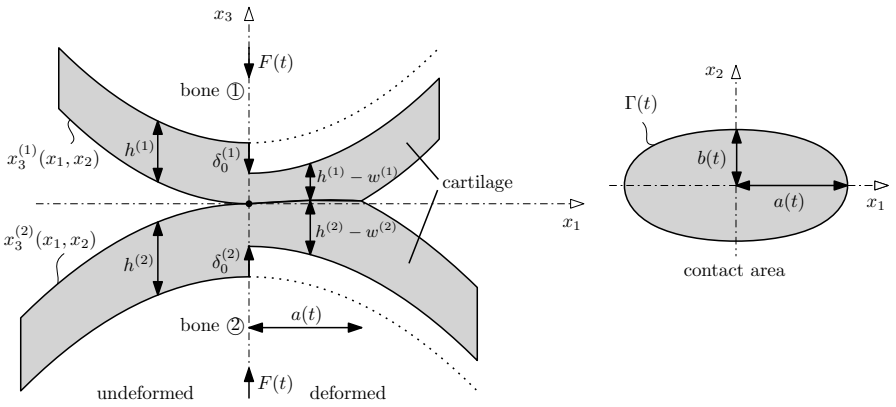

FIGURE 3.1: Geometry of the contact problem. On the left-hand side, the cross section before and after deformation. On the right-hand side, the contact area at time t.

The articular cartilage joint is the zone where two bone heads (1) and (2), coated by thin films of cartilaginous tissue, get in reciprocal contact. Fig. 4.1 gives an idea of the geometrical changes due to deformation

through a finite cross section of the infinitely extended three-dimensional model. There, the left-hand side illustrates the finite cross section on the plane $x_2 = 0$ of the contact zone between two bone heads covered by constant thickness cartilage. The two sides of the cross section split the geometry before and after the compression caused by the force $F(t)$ (see Eq.(3.4)). On the right-hand side of the figure, there is the contact area and its moving boundary. The surface displacements $w^{(i)}$ are taken positive if directed toward the respective bones. The bones gap is $\delta_0 = \delta_0^{(1)} + \delta_0^{(2)}$. If the two cartilage layers present constant thickness, the problem is stated as

$$\delta_0 - w^{(1)} - w^{(2)} = x_3^{(1)} - x_3^{(2)}, \tag{3.4}$$

where the two undeformed surfaces are elliptic paraboloids of equation

$$x_3^{(i)}(x_1, x_2) = \left(\frac{x_1^2}{2R_1^{(i)}} + \frac{x_2^2}{2R_2^{(i)}} \right) (-1)^{(i+1)}. \tag{3.5}$$

This way the right-hand side of Eq.(3.4) may be grouped via a function of the planar coordinates only

$$\Phi(x_1, x_2) = \frac{x_1^2}{2R_1} + \frac{x_2^2}{2R_1} \tag{3.6}$$

expressed through the harmonic averages of the radii

$$\frac{1}{R_k} = \frac{1}{R_k^{(1)}} + \frac{1}{R_k^{(2)}} > 0, \tag{3.7}$$

being strictly positive. Later on we associate the index (1) to the convex

body lying in the upper half-space $x_3 > 0$. The studies by Argatov and Mishuris [54], Rogosin et al. [154] offered a solution to the contact problem which accounts also for the displacement component which is parallel to the contact surface. Despite an increase in computational efforts and loss of simplicity in the obtained formulas, such rigor did not seem to alter dramatically the quantitative results within the usual values of the material and it is consequently neglected in the present work. Substituting the pressure-displacement relation Eq.(3.3) into Eq.(3.4) and multiplying both sides by $m = -(\bar{\alpha}_0^{(1)} + \bar{\alpha}_0^{(2)})^{-1}$ leads to

$$\Delta P(t) + \sum_{j=1}^{4} \alpha_j \int_0^t \mathrm{e}^{\beta_j (t-\theta)} \Delta P(\theta)\, \mathrm{d}\theta + \alpha_5 \int_0^t \Delta P(\theta)\, \mathrm{d}\theta = m(\Phi - \delta_0), \quad (3.8)$$

once defined $\alpha_5 = -m(\alpha_3^{(1)} + \alpha_3^{(2)})$, $\alpha_j = -m\bar{\alpha}_k^{(i)}$ and the exponents $\beta_j = \bar{\beta}_k^{(i)}$ by re-indexing $j = i + 2k - 2$ for $k = 1, 2$. It turns useful to introduce the operator $\mathcal{G}$ as

$$\mathcal{G}y(t) = Y(t) = y(t) + \sum_{j=1}^{4} \alpha_j \int_0^t \mathrm{e}^{\beta_j (t-\theta)} y(\theta)\, \mathrm{d}\theta + \alpha_5 \int_0^t y(\theta)\, \mathrm{d}\theta. \quad (3.9)$$

In view of Eq. (3.9), Eq. (3.8) appears now concisely as

$$\mathcal{G}\Delta P(x_1, x_2, t) = m(\Phi(x_1, x_2) - \delta_0(t)). \quad (3.10)$$

The pressure is set to zero outside the contact area. In the case of cartilage it has been shown that in the superficial area the load is borne mainly by the fluid pressure (Ateshian et al. [52], Argatov and Mishuris [139], Wu and Herzog [155]), indeed shear strains are zero because of the

absence of friction. It means nullifying also the normal derivative of the pressure at the border $\Gamma(t)$ of $\omega(t)$:

$$P = 0, \qquad \nabla P \cdot \mathbf{n} = 0 \qquad \text{on} \quad \Gamma(t), \tag{3.11}$$

with $\mathbf{n}$ outward normal to the border. The total external force $F(t)$ is transmitted through the joint which must be balanced on both the cartilaginous surfaces by means of the pressure. Specifically:

$$\iint_{\omega(t)} P(x_1, x_2, t)\, \mathrm{d}\omega = F(t). \tag{3.12}$$

Summarizing, the unknowns $\delta_0(t)$, $P(x_1, x_2, t)$ and the contact domain $\omega(t)$ represent the solution of the described contact problem if: the contact condition is fulfilled via Eq.(3.10); P satisfies the Dirichlet and Neumann boundary conditions Eq.(3.11) on the moving border of $\omega(t)$ at any time; the distribution of P results in global balance with the external force $F(t)$ as in Eq.(3.12).

3.2 Analytical solution

Summarizing, we study two elliptic paraboloids in reciprocal contact. They share their principal direction along which a force pushes them against each other, e.g. they are neither tilted nor can the force make them slide. In such a configuration, it is reasonable to guess that the

contact area would be an unknown ellipse of border

$$\Gamma(t): \quad \frac{x_1^2}{a^2(t)} + \frac{x_2^2}{b^2(t)} = 1. \tag{3.13}$$

Consequently, adopting a similar line of reasoning as Argatov and Mishuris [156], the solution to Eq. (3.10) is searched in the following form: we assume that $\mathcal{G}P(x_1, x_2, t)$ may be expressed through the auxiliary variable $p(x_1, x_2, t)$; then we factorize p in the form of a product of a time function $p_0(t)$ and a part which fulfills *a priori* the boundary conditions Eqs. (3.11) on $\Gamma(t)$. Naming $a(t)$ and $b(t)$ respectively the major and minor semi-axes of the elliptical contact area to determine,

$$p = \mathcal{G}P(x_1, x_2, t) = p_0(t)\left(1 - \frac{x_1^2}{a^2(t)} - \frac{x_2^2}{b^2(t)}\right)^2, \tag{3.14}$$

which transforms to the problem Eq. (3.10) into

$$\Delta p = m(\Phi - \delta_0). \tag{3.15}$$

Substituting Eq. (3.14) into Eq. (3.15), the resulting relation can be split into three simultaneous conditions by equating the coefficients of the squares of the Cartesian planar coordinates x_1^2, x_1^2 and the remaining constant terms. It will be soon evident how convenient it is to introduce

the ellipse aspect ratio $\lambda(t) = b(t)/a(t)$.

$$\begin{cases} \dfrac{4p_0}{a^4}\dfrac{3\lambda^2+1}{s^2} = \dfrac{m}{2R_1}, \\ \dfrac{4p_0}{a^4}\dfrac{\lambda^2+3}{s^4} = \dfrac{m}{2R_2}, \\ \dfrac{4p_0}{a^2}\dfrac{\lambda^2+1}{s^2} = m\delta_0. \end{cases} \tag{3.16}$$

Dividing the first by the second, it turns out that the aspect ratio depends only on the initial geometry, since it solves

$$3\lambda^4 + \frac{R_1 - R_2}{R_1}\lambda^2 - 3\frac{R_2}{R_1} = 0 \tag{3.17}$$

via the only real positive root

$$\lambda = \sqrt{\frac{R_2 - R_1}{6R_1} + \sqrt{\frac{R_2}{R_1} + \left(\frac{R_2 - R_1}{6R_1}\right)^2}}. \tag{3.18}$$

Such solution is valid for any R_1 and R_2, if chosen according to Section 3.1, including the eventuality that one of the two is negative, which is the common case of a contact between a concave and a convex bone extremity. Combining for instance the first and the third of the system (3.16), $\delta_0(t)$ and $p_0(t)$ are found as power functions of the semi-axis $a(t)$ as follows:

$$\delta_0(t) = \frac{\lambda^2+1}{2R_1(3\lambda^2+1)}a^2(t); \tag{3.19}$$

$$p_0(t) = \frac{m}{8R_1}\frac{\lambda^2}{3\lambda^2+1}a^4(t). \tag{3.20}$$

In view of the latter, Eq. (3.14) becomes

$$p = \mathcal{G}P(x_1, x_2, t) = \frac{m}{8R_1}\frac{\lambda^2}{3\lambda^2+1}\Psi(x_1, x_2, a(t))^2, \tag{3.21}$$

establishing that

$$\Psi(x_1, x_2, a(t)) = a^2(t) - x_1^2 - \frac{x_2^2}{\lambda^2}. \tag{3.22}$$

It remains to enforce the condition Eq. (3.12) in order to gain the unknown $a(t)$. It is easy to integrate p over $\omega(t)$ switching to elliptical coordinates with the result:

$$\iint_{\omega(t)} p(x_1, x_2, t)\,\mathrm{d}\omega = \frac{m\pi\lambda^3}{24R_1(3\lambda^2+1)}a^6(t). \tag{3.23}$$

Recalling the definition of p in Eq. (3.14) and moving the time integral operator $\mathcal{G}$ out of the area integral, then the balance condition Eq. (3.12) appears, leading to

$$a(t) = \left(\frac{24R_1(3\lambda^2+1)}{m\pi\lambda^3}\mathcal{G}F(t)\right)^{1/6}. \tag{3.24}$$

In particular, the major semi-axis at the beginning of the loading $a_0 = a(0)$ depends on the geometries and mechanical parameter m of the two contacting bodies and the initial force $F_0 = F(0)$ as

$$a_0 = \left(\frac{24R_1(3\lambda^2+1)}{m\pi\lambda^3}F_0\right)^{1/6} \tag{3.25}$$

and allows to express $a(t)$, $A(t)$ and $\delta_0(t)$ more concisely as

$$\left(\frac{a(t)}{a_0}\right)^6 = \left(\frac{A(t)}{A(0)}\right)^3 = \left(\frac{\delta_0(t)}{\delta_0(0)}\right)^3 = \mathcal{G}\frac{F(t)}{F_0}. \tag{3.26}$$

The asymptotic solution Eq.(3.3) was obtained under the assumption that the loaded area size is much bigger than the layer thickness, thus F_0 can not be set to zero. The right-hand side of the equation above results then never indeterminate.

In the case of time-independent coefficients α_i and β_i, the operator $\mathcal{G}$ can be inverted as next. Introducing the superscript $\sim$ to indicate the time Laplace transform of parameter s, Eq.(3.9) yields to:

$$\frac{\tilde{y}}{\tilde{Y}} = \left(1 + \sum_{i=1}^{4} \frac{\alpha_i}{s-\beta_i} + \frac{\alpha_5}{s}\right)^{-1} = s\frac{\mathcal{P}_n(s^4)}{\mathcal{P}_d(s^5)} = s\sum_{i=1}^{5}\frac{B_i}{s-\bar{s_i}}, \tag{3.27}$$

being $\bar{s_i}$ and B_i the poles and the residua of the polynomial fraction $\mathcal{P}_n/\mathcal{P}_d$. The remainder is surely zero because $\deg\mathcal{P}_n < \deg\mathcal{P}_d$. By applying the convolution theorem, the Laplace inversion of the above gives

$$\mathcal{G}^{-1}Y(t) = y(t) = \sum_{i=1}^{5} B_i Y(t) + \sum_{i=1}^{5} \bar{s_i} B_i \int_0^t \mathrm{e}^{\bar{s_i}(t-\theta)} Y(\theta)\,\mathrm{d}\theta. \tag{3.28}$$

With the inverse operator in the hand and after the due substitutions in Eq. (3.21), finally the contact pressure can be obtained. Using the symbol H for the Heaviside step function, for fulfilling the boundary conditions

Eq. (3.11) also outside $\omega(t)$, one can write

$$P(x_1, x_2, t) = \frac{m\lambda^2}{8R_1(3\lambda^2+1)}\mathcal{G}^{-1}\Psi^2 H(\Psi), \tag{3.29}$$

where $H(\Psi)$ assumes the value 1 when $\Gamma(t)$ reaches the point of coordinates (x_1, x_2). In the same way it is possible to trace back the individual surface displacements $w^{(i)}$ substituting

$$\Delta P(x_1, x_2, t) = m\mathcal{G}^{-1}(\Phi(x_1, x_2) - \delta_0(t))H(\Psi) \tag{3.30}$$

coming from Eq. (3.10) into Eq.(3.3). The problem stated in Section 3.1 results then analytically solved for the evolution of the contact domain and the bones gap as well as for the contact pressure distribution through Eqs.(3.18), (3.24), (3.19) and (3.29). Moreover, the guess of ellipticity of the contact area Eq.(3.4) is confirmed and in agreement with the previous findings about three-dimensional contact of both single- and biphasic thin layers (e.g. see Argatov and Mishuris [55], Dowson and Yao [157], Hlaváček [158]).

3.3 Numerical benchmarks

Let us consider a single cartilagineous tissue to which the constitutive laws Eqs. (3.1) - (3.2) apply. The TITH stiffness matrix components A_{13}, A_{33}, the only ones which contribute to the asymptotic solution in Vitucci et al. [72] together with A_{44}, can be rewritten as functions of the in-plane and out-of-plane Young's moduli E_1, E_3 and the Poisson ratios

ν_1, ν_{13} as follows:

$$A_{13} = \frac{\nu_{13}}{1 - \nu_1 - 2\nu_{13}^2 \dfrac{E_3}{E_1}} E_3; \qquad A_{33} = \frac{1 - \nu_1}{1 - \nu_1 - 2\nu_{13}^2 \dfrac{E_3}{E_1}} E_3. \tag{3.31}$$

The choice of the material parameters is not completely free though, but bounded by physical restrictions. Particularly, in order to preserve the solid matrix strain energy positivity, it was proved by Auld [159] that, for TITH thin layers, it is required that

$$A_{33} \geq A_{13}, \qquad A_{33} \geq \frac{3}{4} A_{44} \geq 0. \tag{3.32}$$

Specific and separate values of ν_{13} and ν_1 for a TITH cartilage layer have not been traditionally investigated, but the experimental studies which characterize the material as biphasic suggest that the apparent isotropic ratio is relatively small (e.g. see Chegini and Ferguson [70], Wang et al. [160], Keenan et al. [161]). Therefore we assume for simplicity that $\nu_1 = \nu_{13} = 0$ within the next benchmarks. It is easy to show that, in such situation, Eqs.(3.31), combined with Auld's conditions Eq.(3.32), shrink to

$$A_{13} = 0, \qquad A_{33} = E_3 > 0, \qquad A_{33} \geq \frac{3}{4} A_{44} > 0. \tag{3.33}$$

At the same time, in Federico et al. [67], Wu and Herzog [162] it was shown how typical collagen distributions through the cartilage layer cause E_3 also to grow towards the tidemark at $z = 1$, where $E_1 > E_3$; vice versa E_1 decreases until it becomes smaller than E_3 at the tidemark. Since the proteoglycan matrix porosity decreases with the local coordinate z resulting in an overall increased stiffness in the same direction, the isotropic

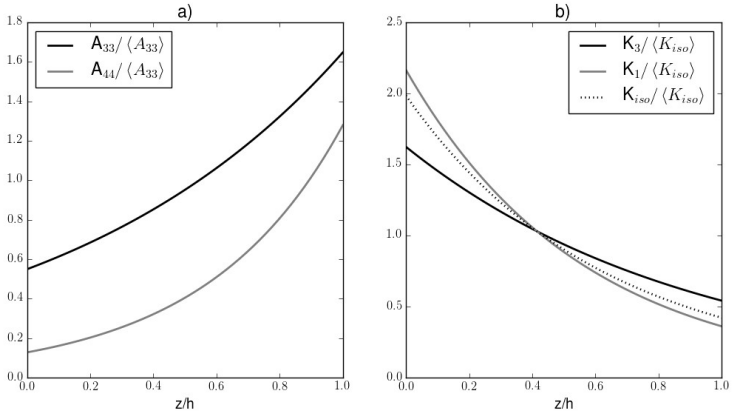

FIGURE 3.2: In-depth distribution of material parameters. a) Stiffness matrix elements as multiples of $\langle A_{33}\rangle$. b) Permeability components as multiples of $\langle K_{\text{iso}}\rangle$.

Young's modulus at the articular surface is smaller than at the bone attachment. The setting that we will use, which also accounts for these considerations, reads

$$A_{13} = 0, \qquad \gamma = \frac{\log 3}{2}, \qquad \alpha = \log 10. \tag{3.34}$$

The reader can notice, looking at Eq.(3.2), that the shear modulus A_{44} presents a tenfold increase through the depth as in Buckley et al. [163], while the axial permeability K_3, linked to the axial stiffness inhomogeneity by the parameter γ, is let decrease three times toward the tidemark. As shown in Federico and Herzog [68], the planar permeability K_1 is expected to be larger than axial K_3 at the articular surface and vice versa at $z = 0$ as the fluid flows easier along the prevailing collagen fibers orientation, while the overall equivalent isotropic $K_{\text{iso}} = (2K_1 + K_3)/3$

steadily grows as a result of the decreased porosity. This leads us to the choice:

$$k_1 = \frac{4}{3}k_{33}, \qquad \gamma_1 = \log 6. \tag{3.35}$$

The material was assigned average typical stiffness values $\langle A_{33}\rangle = 2\langle A_{44}\rangle = 0.5$MPa (e.g. see Boschetti et al. [164]). Furthermore, an isotropic permeability was considered of average value $\langle K_{\text{iso}}\rangle = 2 \cdot 10^{-14}\text{m}^4\text{N}^{-1}\text{s}^{-1}$ similarly to the findings of Boschetti et al. [164], Boschetti and Peretti [165]. The same properties are assigned to all the layers within the following benchmarks. The resulting distribution of the material parameters through the depth of the cartilage layer is shown in Fig. 3.2.

Focusing on the tibiofemoral knee joint in extension, it is the locus where the two medial and lateral femoral condyles - respectively denoted M and L later on - contact the underlying tibial plateau. The latter is considerably flat at least in the stance contact area, which leads to choose the curvatures $1/R_1^{(2)} = 1/R_2^{(2)} = 0$. The medial condyle has been observed to be approximately spherical ((Martelli and Pinskerova [166], Kim and Suh [167])) causing an approximately circular contact area, i.e. $R_1^{(1M)}/R_2^{(1M)} = 1$, $\lambda^{(M)} = 1$. A visual estimate of the typical lateral contact area detected via magnetic resonance imaging (MRI) published in Hosseini et al. [147] reveals a much tapered shape than in the medial compartment with an aspect ratio of about $\lambda^{(L)} = 0.5$ which indicates $R_1^{(1M)}/R_2^{(1M)} = 7.43$ from Eq. (3.17), where the reference axis x_1 is in the sagittal plane, x_2 in the coronal one. Making use of Eq. (3.19),

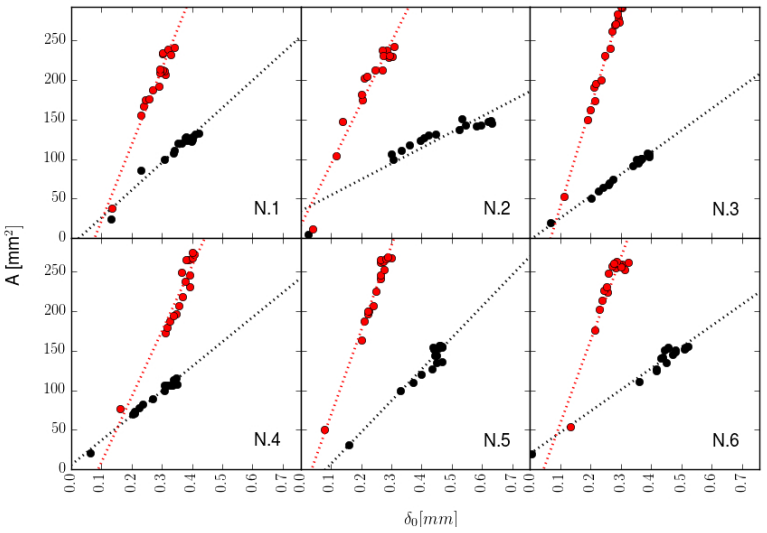

FIGURE 3.3: Linear dependency of $A(t)$ and $\delta_0(t)$ observed in the results published in Hosseini et al. [147]. Six human tibiofemoral joints were loaded *in vivo* and the contact area and bones gap were measured via MRI. Such dependency can be expained by Eq.(3.36). Points represent the experimental results, dotted lines their linear regression. Black indicates the lateral compartment, red the medial one.

one can deduce that the ratio

$$\frac{A(t)}{\delta_0(t)} = \frac{2\pi(3\lambda^2+1)}{\lambda^2+1} R_1 \tag{3.36}$$

is supposed to be time independent according to our model. Analyzing the results of Hosseini et al. [147] in terms of contact area and bones gap, the ratio $A(t)/\delta_0(t)$ presents indeed appreciably constant slope (see Fig.3.3), from which we are able to extract the unpublished size of their 6 patients for both the joint compartments expressed as contact radii. The

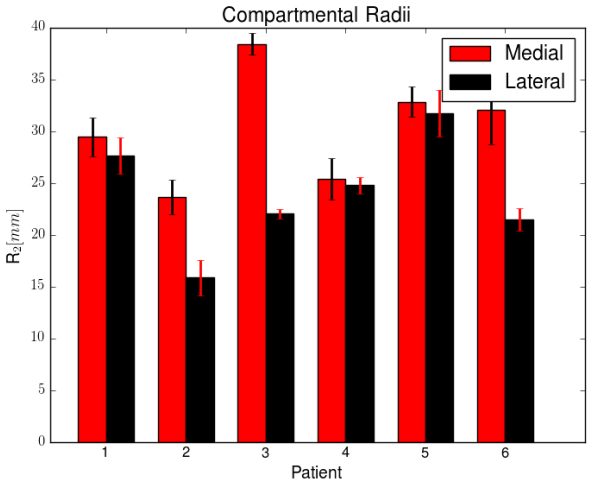

FIGURE 3.4: Minimum contact curvature radii R_2 and respective error extracted from the experimental data published by Hosseini et al. [147] assuming that the aspect ratios of the contact ellipses for the medial and lateral compartments of the tibiofemoral joint are $\lambda^{(M)} = 1$, $\lambda^{(L)} = 0.5$.

retrieved values and standard deviations are illustrated in Fig. 3.4. The average medial $R_2^{(1M)}$ and lateral $R_2^{(1L)}$ were found to be 30.3±4.9mm and 23.9 ± 5.0mm with the same level of uncertainty. The minimum medial radius, in the coronal plane, resulted then approximately 27% bigger than the lateral one, which is in good agreement with the findings of Siebold et al. [168]. The fact that the maximum medial radius, the one in the sagittal plane, is much bigger and equal to 225.3±36.5mm agrees with the observation by Martelli and Pinskerova [166], where they noticed that, at stance, the medial condyle in such direction appears very flattened and a precise estimation of the contact radius results difficult. The two couple of average radii are adopted in the subsequent calculations together with

the average thicknesses $h^{(M)} = 1.3$mm and $h^{(L)} = 1.6$mm extracted from Hosseini et al. [147].

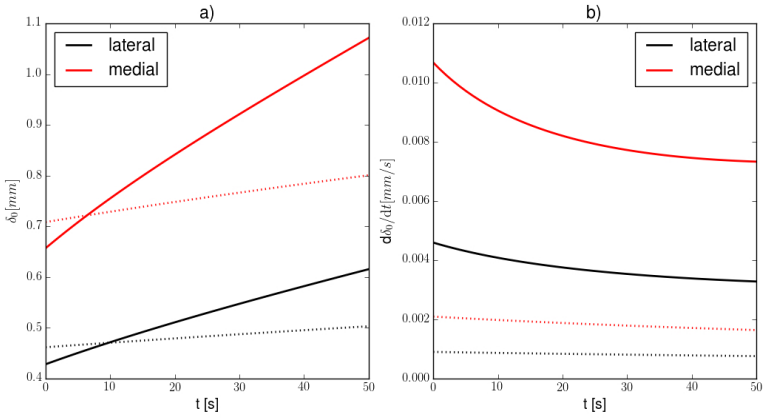

FIGURE 3.5: First 50s of a constant load $F = 700$N. Continuous lines illustrate the results for a TITH material, dotted ones indicate the isotropic homogeneous cartilage behaviour if averaged TITH stiffness and permeability are assigned. The medial compartment bears double as much load as the lateral one. a) Bones gap $\delta_0(t)$. b) Time-derivative of δ_0.

First we examine the case of a load deriving from a body weight of 700N at stance (about the European average according to Walpole et al. [169]), equally split between the two knees and distributed for 2/3 and 1/3 respectively on the medial and lateral compartments. It has been indeed measured that the medial compartment carries a much larger part of the load (Werner et al. [170], Halder et al. [171]). What we want to investigate is how an inhomogeneous distribution of stiffness and permeability may be able to improve the cartilage performance with respect to a homogeneous one whose properties present the same average across the

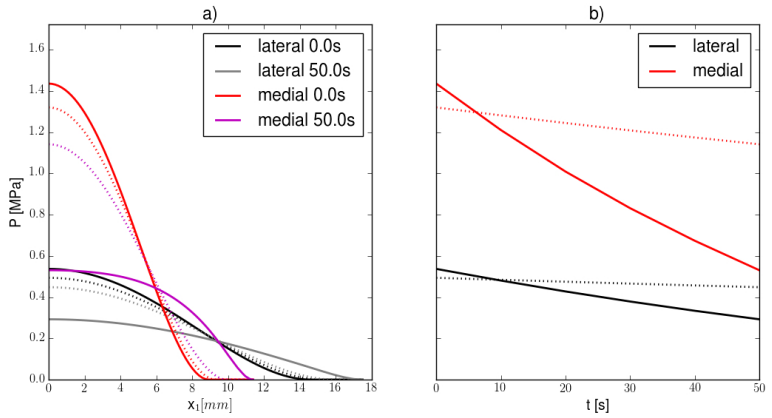

FIGURE 3.6: Contact pressure distribution and evolution under constant load. Dotted lines stand for the isotropic homogeneous model. a) Distribution along the axis x_1 containing the major semiaxis $a(t)$ of the elliptical contact area soon after the loading and after 50s. b) First 50s of the pressure in the center of the contact area of coordinates $x_1 = x_2 = 0$.

thickness. In a way, how an actual cartilage arranges its mechanical resources for carrying out its functions. The resulting gap $\delta_0(t)$ in Fig. 3.5 is compared with the solution of Argatov and Mishuris [55] for an isotropic homogeneous cartilage layer. For both the compartments, despite the initial value is smaller than according to such solution, δ_0 grows remarkably quicker. Besides, its derivative, at least in first seconds, decreases much faster, pronouncing such desirable property already addressed in Wu et al. [53]. In Fig. 3.6 we plot the contact pressure along the axis x_1 and its evolution in time. The results, in this case, exhibit not only a quantitative difference, but also a qualitative one. The curves in Fig. 3.6.a) for the TITH material do not deform homothetically during the expansion of the contact area like the homogeneous material would do, but the novel

formula Eq. (3.29) allow them to change shape by flattening them at the origin. Here the mechanical convenience for the body in developing an inhomogeneous layer appears evident in the sense that, stated that one of the main functions of cartilage is to lower the pressure peaks, such aim is accomplished via a more even distribution of the force inside the contact area together with a faster decrease of the maximum pressure. It is in fact intuitive that it descends from the presence of a compliant zone of high permeability and low stiffness close to the cartilage surface.

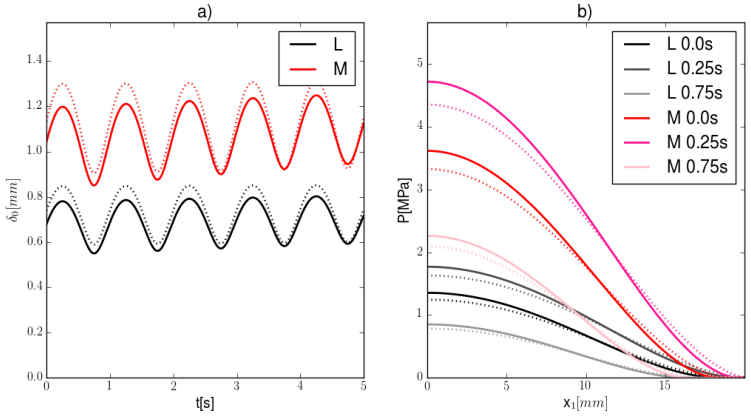

FIGURE 3.7: Bones gap and consequent contact pressure profiles under oscillatinf load. Dotted lines show the the response of the isotropic homogeneous material averaged in the sense we discuss in the current section. a) First five cycles of deformations in therms of δ_0. b) Contact pressure displayed at $t = 0$ and the first maximum and minimum peak of deformation.

The second load condition that we exemplify deals with a sinusoidal force of period 1s, similar to the frequency a normal human gait, and that oscillates on each knee between 0.5 and 1.5 of the same body weight of 700N. The portions absorbed by the two knee compartments stay the

same as in the previous benchmark. Fig. 3.7.a) shows the gap in the first five cycles for both compartments and compares it with the isotropic homogeneous solution homogenized as above. The oscillating part of $\delta_0(t)$ does not indicate a different behavior than the results obtained in Argatov and Mishuris [55], whereas it is clear that the steadier increase of the average trend is similar to the curves of Fig. 3.5.a). In the short five cycles interval examined here, the effect discussed with regard to Fig. 3.5.b) is not observable and in this case the difference between the continuous and dotted lines seems purely an outcome of the larger areas obtained for the isotropic homogeneous material with the particular homogenization criterion chosen in this Section. The oscillating deformation added onto a weakly increasing trend shows good agreement with the results of a similar load condition applied to two identical spherical homogeneous isotropic layers in Wu et al. [172].

3.4 Remarks

For the three-dimensional geometry described in Eq.(3.5), we were able to obtain the bones gap, the evolution of the contact area and the corresponding pressure distribution due to an arbitrary force applied onto the TITH biphasic cartilage layer treated in Vitucci et al. [72] (see Eqs.(3.19), (3.24), (3.29)). The asymptotic solution is retrieved in closed-form and its exact within the model assumptions. Observing the case of constant loading, the introduction of inhomogeneity and anisotropy allows to obtain, in time, a significantly different decrease of the peak contact pressure

and growth of the contact area with respect to an isotropic homogeneous material whose properties are simply the average of the TITH one (see examples in Figs. 3.5,3.6,3.7). This proves once more that the scientist who intends to model the behavior of cartilage needs to pay a great attention to the interpretation of the material properties provided by experiments. The results are qualitatively similar to the analytical ones obtained by Chidlow et al. [173] in the framework of functionally graded materials when dealing with an inhomogeneous elastic coating on top of an infinite half-space.

It seems remarkable that the ratio of the contact area and the bones gap is predicted to stay constant in time independently of the applied load as expressed in Eq.(3.36). Such proportionality should not be taken for granted even though it arises also in the well known Hertzian contact theory. Indeed a number of differences exist between our asymptotic formulation and the classical one, among which: the nature of our constitutive laws is biphasic and derives from mixture theory; the Hertzian contact involves half-spaces whereas ours deals with thin infinite thin layers; Hertz did not impose zero normal derivative to the contact pressure at the border of the contact area. About this last difference, if one tries to remove the zero pressure gradient condition in Eq.(3.11) from the problem, it is easy to show that an additional solution appears. It corresponds to an elliptically parabolic ditribution contact pressure. This means that the unicity of the solution is broken. Although a mathematical analysis might rigorously explain the reason, this is out of the scope of the present work. Our best guess is intimately related to the operator $\mathcal{G}$, which makes Eq.(3.10) an integro-differential equation on unknown

expanding domain. From a purely mechanical point of view, the boundary condition has been first introduced by Ateshian et al. [52] and later debated by Wu and Herzog [155], Hlaváček [174] without a definitive conclusion.

By making use of the above mentioned proportionality, together with assumptions on the ellipticity of the contact areas, it was possible to make very reasonable guesses about the originating contact radii which were neither published in the work Hosseini et al. [147] nor later. The intercepts of the linear regressions in Fig.3.3 were not zero though and it may derive from initial contact conditions that are different from the ones assumed by our model.

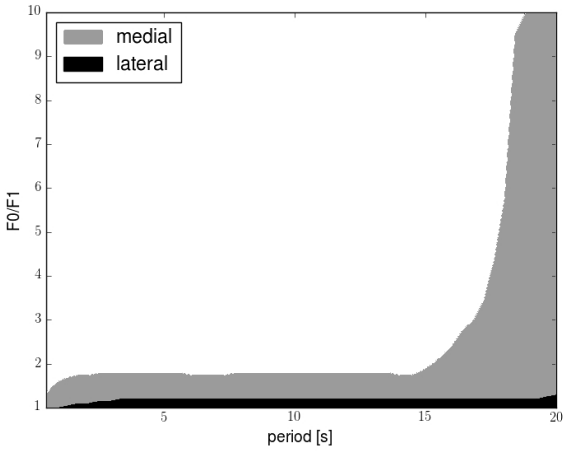

FIGURE 3.8: Negative pressure arising under five cycles of loading for different ratios between the constant and oscillatory part F_0 and F_1 of the force and different oscillation periods.

All the family of asymptotic solutions Ateshian et al. [52], Wu et al. [53], Argatov and Mishuris [55], Vitucci et al. [72], Argatov and Mishuris [139], Wu et al. [146] do not take into account the dependency of the permeability on the volumetric strain that has been well known since the study Mow et al. [50]. If this simplification of the equations permits the advantageous feature of closed-form, easily analyzable solutions, on the other hand it causes unbounded deformation. It can be seen, for instance, in Fig.3.8 that negative pressure may arise due to such unboundedness for high oscillating load portions and always for prolonged load application, visible on the right-hand side of the plot. Such values of the pressure are obviously unphysical and not acceptable, given that no adhesion is assigned to the layers surfaces. On the other hand, that the validity of the proposed gap is constrained to short time response is part of the model preconditions. Asymptotic formulas of the kind of Eq.(3.3) are in fact reliable under the assumption that the considered time is much smaller than the hydrogel characteristic time $\tau_{\text{gel}} = h^2/(A_{33}K_3)$ which takes the value of about 290s in the benchmarks of Sec.3.3. An asymptotic solution which includes the effect of strain-dependent permeability is currently under investigation and would presumably make the present model applicable also for later times.

The advances in imaging techniques allow nowadays to obtain very detailed measurements from *in vivo* experiments on articular cartilage. A considerable amount of studies have been published on the topic, among which Hosseini et al. [147], Herberhold et al. [175], Song et al. [176], Wan et al. [177], Li et al. [178], Bingham et al. [179], Shin et al. [180], Chan

et al. [181]. The field looks ready for enhancing early diagnoses of degenerative pathologies such as osteoarthritis with consequent benefits for the patients. In order to exploit such technological advantages, though, more extended studies need to be conducted. It would be seriously fruitful for the scientists working on mechanical modeling to see more data provided in these publications regarding at least the geometry of the contact areas and of the contact surfaces, the forces applied onto the single articular cartilages. This way a correct modeling could finally lead to real time analyses and standard procedures.

Chapter 4

Mechanics of intra-articular pressure

Degenerative pathologies of the diathrodial joints, e.g. osteoarthritis, affect tens of millions people worldwide. Population aging is prospected to worsen such a scenario even further in the next decades. Various physical factors and scales are known to contribute to the evolution of the diseased joint from a light inflammatory state up to cartilage disintegration. Nevertheless safe and efficient prevention and cures are not available yet.

In mechanics, a thorough attention has been dedicated to the modelling of the cartilage layers covering the bones in the contacting zone. Elastic, viscoelastic, multi-phasic constitutive models have been implemented in an attempt to predict the solicitations which can cause damage and allow it to progress.

Very little consideration has been given in the past to the mechanical role of the synovial membrane in constraining the lubricating fluid in the joint capsule. The reason lies in the common belief that no main mechanical function is provided by it, though no quantitative estimation has ever made available in literature.

In order to address this concern for the first time, we study the two-dimensional problem whose geometry is described in Fig. 4.1. A biphasic thin layer of cartilage is attached at a rigid bone extremity and shaped as a parabola. Unlike in Chapters 2 and 3, anisotropy and inhomogeneity are dropped here for reducing the numbers of parameters. An incompressible fluid fills the cavity and is prevented to escape by a linear elastic membrane. The unilateral contact is analyzed together with the hypotheses of absence of friction and homogeneous pressure of the fluid. Since the membrane elasticity is generally affected by inflammatory states, the preliminary results of such nonlinear problem are aimed to investigate the effects of the membrane stiffness on the contact development.

4.1 2D contact for biphasic cartilage

We analyze the uni-directional contact of a thin biphasic layer in 2D. The three-dimensional results by Ateshian et al. [52] can easily be reduced to the two-dimensional case by consider only one planar direction x. The problem is written as

$$\mathcal{K}\left[\frac{\partial^2 P(x,\cdot)}{\partial x^2}\right](t) = m\left(\frac{x^2}{2R} - \delta(t)\right) \qquad \text{for} \quad x \in [-a(t), a(t)], \quad (4.1)$$

where m and $\mathcal{K}$ account for material thickness and properties, δ is the contact separation, $y = x^2/(2R)$ is the equation of the parabola. One has to find $\delta(t)$, $a(t)$, the time dependent width of the contact, and $P(x,t)$, the contact pressure.

The integro-differential equation above must be supplied with boundary conditions. If at the border or the contact there is no external imposed pressure and the only load is represented by a vertical force f, then

$$P = 0, \qquad \frac{\partial P}{\partial x} = 0 \qquad \text{for} \quad x = \pm a(t), \tag{4.2}$$

$$\int_{-a(t)}^{a(t)} P(x,t)\,\mathrm{d}x = f(t) \qquad \forall t \geq 0. \tag{4.3}$$

The integral operator $\mathcal{K}$ is defined as

$$\mathcal{K}[Y](t) = Y(t) + \chi \int_0^t Y(\tau)\,\mathrm{d}\tau, \tag{4.4}$$

which is similar to Eq.(3.9), but missing the exponential convolutions typical of the inhomogeneous tissues of Chapter 2. The parameter χ is constant and collects problem parameters.

Firstly, we assume that the auxiliary function

$$p(x,t) = \mathcal{K}[P(x,\cdot)](t) \tag{4.5}$$

satisfies a priori the boundary conditions Eq.(4.2) as

$$p(x,t) = \bar{p}\left(a^2(t) - x^2\right)^2. \tag{4.6}$$

By substituting this into Eq.(4.1), we equate the coefficients which multiply the same degree of x in order to determine

$$\bar{p} = \frac{m}{24R}, \qquad \delta(t) = \frac{a^2(t)}{6R}. \tag{4.7}$$

Let us multiply Eq.(4.1) by $x^2/2$ and integrate it over the contact domain

$$\int_{-a(t)}^{a(t)} \frac{x^2}{2} \frac{\partial^2 p(x,t)}{\partial x^2} \,\mathrm{d}x = m \int_{-a(t)}^{a(t)} \frac{x^2}{2} \left(\frac{x^2}{2R} - \delta(t) \right) \mathrm{d}x. \tag{4.8}$$

The contact displacement scales with the square of the contact width, a common feature with the 3D contact as derived in Chapter 3. If one integrates the left-hand side by parts twice, this becomes

$$\int_{-a(t)}^{a(t)} p(x,t) \,\mathrm{d}x = \mathcal{K} \left[\int_{-a(t)}^{a(t)} P(x,t) \,\mathrm{d}x \right] (t) = \mathcal{K}[f](t), \tag{4.9}$$

via enforcing Eq.(4.3) and (4.2). By substituting Eq.(4.7) into the right-hand side of Eq.(4.8) and integrating explicitly, finally the time-dependent half-width of the contact domain is found to be

$$a(t) = \left(\frac{45R}{2m} \mathcal{K}[f](t) \right)^{1/5}. \tag{4.10}$$

It is perhaps worth noticing that in the case of 3D contact, due to one more dimension, the exponent of the left-hand side is one sixth. It is easily shown, for instance by using Laplace transformation, that the inverse operator

$$\mathcal{K}^{-1}[Y](t) = Y(t) - \chi \int_0^t Y(\tau) \mathrm{e}^{\chi(\tau - t)} \,\mathrm{d}\tau. \tag{4.11}$$

Hence, according to Eqs.(4.5) and (4.6), one also has the solution in terms of contact pressure

$$P(x,t) = \frac{m}{24R}\mathcal{K}^{-1}\left[\left(a^2(\cdot) - x^2\right)^2\right](t). \tag{4.12}$$

Nonzero pressure at the boundary Let us consider the the same problem as above, but let us change the boundary conditions of P from Eq.(4.2) to

$$P = P_a(t), \qquad \frac{\partial P}{\partial x} = 0 \qquad \text{for} \quad x = \pm a(t). \tag{4.13}$$

It means assigning a border value to the contact pressure while preserving its flatness, due to the peculiar surface stresses of biphasic layers as discussed in Chapter 3. In this case the guess on $p = \mathcal{K}P$ becomes

$$p(x,t) = \frac{m}{24R}\left(a^2(t) - x^2\right)^2 + p_a, \tag{4.14}$$

where $p_a = \mathcal{K}[P_a](t)$. See that the imposed P_a has no effect in terms of the contact displacement δ versus a relation, i.e. Eq.(4.7), as the second derivative of p_a is zero. By applying the same integration by parts as Eq.(4.8), one obtains now the equation for finding the half-width of the contact area

$$\frac{m}{45R}a^5(t) + 2\mathcal{K}[aP_a](t) - \mathcal{K}[f](t) = 0, \tag{4.15}$$

that is an integral quintic in a that can not be solved but numerically, in contrast to the case of zero border pressure in Eq.(4.10). Once $a(t)$ is known, the problem is considered to be solved also in terms of pressure

field by inverting Eq.(4.14) into

$$P(x,t) = P_a(t) + \frac{m}{24R}\mathcal{K}^{-1}\left[\left(a^2(\cdot) - x^2\right)^2\right](t). \tag{4.16}$$

4.2 Fluid-bone interaction in joint capsule

In the previous section, we have analyzed the unilateral contact and solved for the contact pressure also in the case of non-zero boundary conditions. Here, we make use of those results in order to couple the cartilage contact surrounded by pressurized fluid.

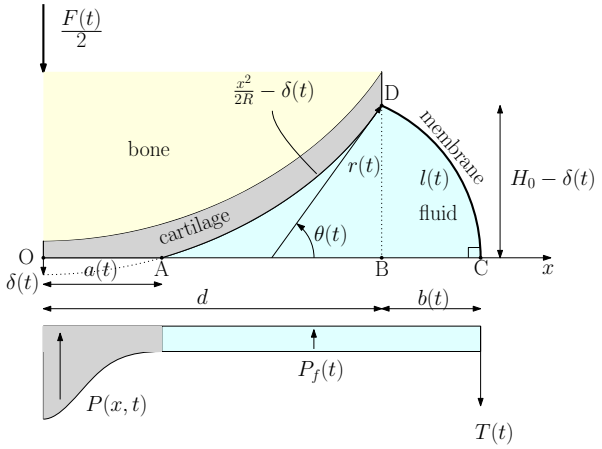

FIGURE 4.1: Problem description. Due to the parabolic shape of the cartilage surface, $H_0 = \frac{d^2}{2R}$.

Our aim is to quantify the role of the fluid-filled capsule in sustaining the load $F(t)$ applied to the joint. We enable the capsule fluid pressurization by means of an elastic membrane working as fluid constraint. The fluid

is incompressible and we neglect its fluid dynamics, i.e. the pressure P_f is constant it. The membrane elasticity is linear and it has no bending stiffness. Thus, its constitutive equations is simply stated via its stiffness S as

$$\frac{\mathrm{d}T}{\mathrm{d}l} = S, \tag{4.17}$$

with T and l being its tension and length.

4.2.1 Volume-Pressure relation: simplest case

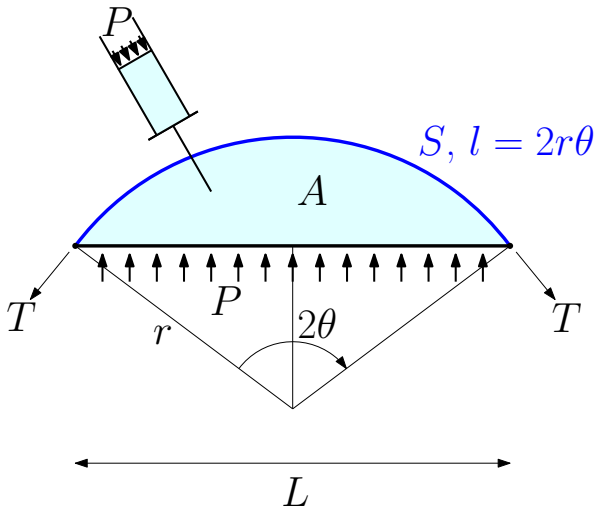

FIGURE 4.2: Inflation of an elastic membrane fixed to two extremes.

In order to analyze such a complex multi-body mechanism, it turns explicative to study a simpler scenario first. Let us consider the system in Fig.4.2. An elastic membrane of linear stiffness S is anchored to two extremities and it is unstressed when no fluid fills the capsule. Successively, some volume (area in 2D) A of incompressible fluid is injected in between

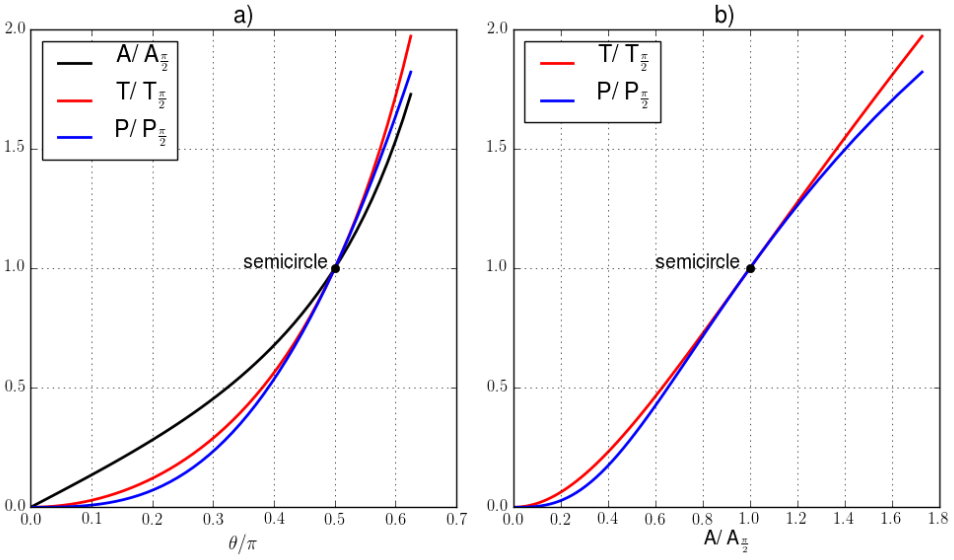

FIGURE 4.3: Normalized mechanical variable with respect to their value at $\theta = \pi/2$. a) Volume A, membrane tension T and fluid pressure P versus θ. b) Membrane tension and fluid pressure at increasing injected fluid.

the membrane and the rigid impermeable constraint. The extension of the membrane from L to l, which allows the fluid to flow in, requires a pressure P applied to the syringe. A balance must be achieved between the pressure contribution $2Pr\sin\theta$ and the membrane tension $2T\sin\theta$ according to

$$P = \frac{T}{r} = \frac{S}{r}(l - L) = 2S(\theta - \sin\theta). \tag{4.18}$$

It is worth noticing that the above equation is the Young-Laplace one, but modified in order to take into account that the membrane tension changes with strains. Besides, the injected volume relates to the system

geometry as

$$A = r^2 \left(\theta - \frac{\sin 2\theta}{2}\right) = \frac{L^2}{4\sin^2\theta}\left(\theta - \frac{\sin 2\theta}{2}\right). \tag{4.19}$$

The two equations above constitutes the parametric relation between A, P and T. After normalization, one can visualize them as in Fig.4.3. The flat configuration corresponds to $\theta = 0$, while the one where the constraint is the diameter of the semicircle containing the fluid happens at $\theta = \pi/2$.

Particularly, a curve of the kind in Fig.4.3b) can be used for estimating the synovial membrane stiffness during *in-vivo* measurements. The ideal procedure would require to measure the total volume of the synovial fluid and to assess the capsule geometry at given joint range via modern non invasive imaging techniques. Similarly as in Eq.(4.18), the fluid pressure would be now dependent only on the stiffness S. In real life applications, the membrane could not be considered linearly elastic (i.e., $S = S(l)$) either because of constitutive or geometric reasons. This would suggest the necessity of additional data such as measuring the membrane extension. We would like to point out that, even in such a scenario, the experimental setup would be compatible with *in-vivo* diagnosis. The similarities between our results and Nade and Newbold [82], Schwarz et al. [83], Yen et al. [84] are remarkable. Those studies repeatedly showed, indeed, a pronounced stiffening during inflation. In the *in vivo* tests by Jayson and Dixon [77, 78], Jawed et al. [79], Viitanen et al. [80], Myers and Palmer [81], the initial volume was not measured. We argue that the simplest explanation for change of stiffness for $P(V)$ at different flexion

angles and pathological conditions are due to that. Therefore, the differences spotted with the same membrane can be seen as shifts in the origin in Fig.4.3b). Swollen joints (with arthritis) or bent limbs present an increased starting volume in the experiment.

4.2.2 Full coupling mechanism of pressurized fluid and biphasic contact

With the goal of enforcing the fluid incompressibility, one has to ensure the area ACD in Fig. 4.1 remains constant. This can be split in two parts, Ω_{ABD} and Ω_{BCD}, whose contribution are respectively:

$$\begin{aligned} \Omega_{\mathrm{ABD}} = &= \int_{a(t)}^{d} \left(\frac{x^2}{2R} - \delta \right) \mathrm{d} = \frac{d^3 - a^3(t)}{6R} - \delta(t)(d - a(t)); \\ \Omega_{\mathrm{BCD}} &= \left(\theta(t) - \frac{\sin 2\theta(t)}{2} \right) \frac{r^2(t)}{2}. \end{aligned} \tag{4.20}$$

The conservation law results then

$$\frac{\mathrm{d}}{\mathrm{d}t}\Omega_{\mathrm{ABD}}\left(a(t), \delta(t), t\right) + \frac{\mathrm{d}}{\mathrm{d}t}\Omega_{\mathrm{BCD}}\left(\theta(t), r(t), t\right) = 0, \tag{4.21}$$

or, equivalently,

$$\Omega_{\mathrm{ABD}}\left(a(t), \delta(t), t\right) + \Omega_{\mathrm{BCD}}\left(\theta(t), r(t), t\right) = A_0, \tag{4.22}$$

if the area occupied by the fluid is known at a time $t = t_0$. If one wants to simulate the pressure volume experiment described in Subsection 4.2.1,

A_0 should also depend on time and be assigned by controlling the injection.

Furthermore, equilibrium has also to be guaranteed. We write it along the bottom line OA of the geometry in Fig. 4.1. The contribution of the biphasic layer, the fluid and the elastic membrane are on the left-hand side of

$$\begin{aligned}\frac{m}{45R}\mathcal{K}^{-1}\left[a^5\right](t) + a(t)P_f(t) + (d - a(t) + b(t))\,P_f(t) - T(t)\\ = \frac{m}{45R}\mathcal{K}^{-1}\left[a^5\right](t) + (d + b(t))\,P_f(t) - T(t) = \frac{F(t)}{2},\end{aligned} \tag{4.23}$$

for obtaining which Eq.(4.15) has been used, imposing that the contact pressure at the border of the contact area is the same as the fluid's. The unknown δ can be expressed as function of $a^2/(6R)$ via Eq.(4.7), therefore

$$r(t)\sin\theta(t) = \frac{d^2}{2R} - \frac{a(t)^2}{6R}. \tag{4.24}$$

The unknowns θ, r and b are also interdependent:

$$b(t) = (1 - \cos\theta(t))\,r(t). \tag{4.25}$$

The equilibrium of the membrane gives one more relation

$$P_f(t)r(t) = T(t) \qquad \forall t, \tag{4.26}$$

which is equivalent to Young-Laplace equation in 2D. Lastly, by integrating the constitutive equation of the membrane Eq.(4.17) in the present

case of circular configuration, one obtains

$$T(t) = T_0 + S(l(t) - l_0)), \tag{4.27}$$

where the subscript 0 refers to a known configuration at the time $t = t_0$. l is the membrane length

$$l(t) = r(t)\theta(t) = \left(\frac{d^2}{2R} - \delta(t)\right)\frac{\theta(t)}{\sin\theta(t)}. \tag{4.28}$$

Summarizing, we have two main equations, mass conservation and vertical equilibrium Eqs.(4.21) and (4.23), plus a set of five additional relations which allow to reduce the problem to the search of two functions of time, e.g. $a(t)$ and $\theta(t)$. Namely, by simple substitutions:

$$\begin{aligned} &\frac{d}{6R}(d^2 - a^2) + \left(\theta - \frac{\sin 2\theta}{2}\right)\frac{r^2(a,\theta)}{2} - A_0 = 0; \\ &\frac{m}{45R}\mathcal{K}^{-1}\left[a^5\right](t) + \left(\frac{d}{r(a,\theta)} - \cos\theta\right)T(a,\theta) - \frac{F(t)}{2} = 0. \end{aligned} \tag{4.29}$$

Reduction to one unknown In order to reduce the number of unknowns, one can solve the first of Eq.(4.29) for $a = a(\theta)$. Introducing, for instance, the auxiliary function

$$\Phi(\theta) = \frac{\theta - \frac{\sin 2\theta}{2}}{2\sin^2\theta}, \tag{4.30}$$

the mass conservation becomes a quadric in δ:

$$\Phi(\theta)\delta^2 - \left(d + \Phi(\theta)\frac{d^2}{R}\right)\delta - \left(A_0 - \frac{d^3}{6R} - \Phi(\theta)\frac{d^4}{4R^2}\right) = 0. \tag{4.31}$$

It's solution, coherent with the choice of

$$\theta \in [0; \pi], \tag{4.32}$$

is:

$$\delta(\theta) = \frac{a^2(\theta)}{6R} = \frac{d}{2\Phi} + \frac{d^2}{2R} - \sqrt{\left(\frac{d}{2\Phi} + \frac{d^2}{2R}\right)^2 + \frac{1}{\Phi}\left(A_0 - \frac{d^3}{6R} - \Phi\frac{d^4}{4R^2}\right)}, \tag{4.33}$$

which simplifies into $\delta = \frac{d^2}{6R} - \frac{A_0}{d}$ for $\theta = 0$.

Now, with $a(\theta)$ in one hand, the second equation in Eq.(4.29), i.e. the equilibrium balance, reduces to the search for θ from

$$\frac{m}{45R}\mathcal{K}^{-1}\left[a^5(\theta(\cdot))\right](t) + \left(\frac{d}{r(\theta(t))} - \cos\theta(t)\right)T(\theta(t)) - \frac{F(t)}{2} = 0 \tag{4.34}$$

at every time t. The latest is a highly non-linear Volterra integral equation of second kind and we could not shun a numerical approach for its solution.

Numerical scheme One solving strategy for Eq.(4.34) could consist in applying a standard algorithm for non-linear equations (e.g. Newton's scheme) at every time $t = t_i$. The only non-trivial issue regards the operator $\mathcal{K}^{-1}$ defined in Eq.(4.11). Defining $\theta_i = \theta(t_i)$ and $a_i = a(\theta_i)$,

one has

$$\begin{aligned}\mathcal{K}^{-1}\left[a^5\right](t_i) &= a_i^5 - \chi \mathrm{e}^{-\chi t_i}\left(\int_0^{t_{i-1}} a^5(\tau)\mathrm{e}^{\chi\tau}\,\mathrm{d}\tau + \int_{t_{i-1}}^{t_i} a^5(\tau)\mathrm{e}^{\chi\tau}\,\mathrm{d}\tau\right)\\ &\approx a_i^5 - \frac{\chi}{2}\mathrm{e}^{-\chi t_i}\left(\sum_{j=1}^{i-1}\underbrace{(a_j^5 + a_{j-1}^5)(t_j - t_{j-1})}_{g_j} + \underbrace{(a_i^5 + a_{i-1}^5)(t_i - t_{i-1})}_{g_i(a_i)}\right)\\ &= a_i^5 - \frac{\chi}{2}\mathrm{e}^{-\chi t_i}\left(\sum_{j=1}^{i-1} g_j + g_i(a_i)\right) \qquad \forall i \in \mathbb{N} > 0.\end{aligned} \tag{4.35}$$

The numerical procedure is thus established, at the time t_i, for finding the unknown $\theta_i = \theta(t_i)$, as

$$\begin{aligned}&\frac{m}{45R}\left(a_i^5 - \frac{\chi}{2}\mathrm{e}^{-\chi t_i}\left(\sum_{j=1}^{i-1} g_j + g_i(a_i)\right)\right)\\ &+\left(\frac{d}{r(\theta_i)} - \cos\theta_i\right)T(\theta_i) - \frac{F(t_i)}{2} = 0,\end{aligned} \tag{4.36}$$

where one would update the forcing term $F(t_i)$ and the cumulated integral $\sum_{j=1}^{i-1} g_j$ at every step. In our attempt, this strategy has not turned successful and its results have shown highly dependent on time step size without a sound hint of convergence towards benchmark analytical solutions. The explanation for it is beyond the scope of the present work, but evidently ascribes to what, in the study of differential equations, would be called stiffness.

Our alternative endeavor has been borne by means of an implicit method. We have discretized the time in N time steps and assigned a trial values

to the θ_i. These θ_i represent the degrees of freedom of the discrete method and the choice is equivalent to adopt linear basis functions for θ. Let us write Eq.(4.34) in the synthetic form

$$F_r(\theta(t), t) - \frac{F(t)}{2} = 0, \tag{4.37}$$

where the sum F_r of all the reactive forces of the system, i.e. the contact pressure, the fluid pressure and the membrane tension, have to balance the assigned external force. If one approximates

$$F_r(\theta, t) \approx F_r(\theta_0, \theta_1, \ldots, \theta_N, t), \tag{4.38}$$

where θ_0 is given by initial conditions, then Eq.(4.37) can be numerically solved as the minimization problem

$$\min_{\theta_1,\ldots,\theta_N} \sum_{i=1}^{N} \left(F_r(\theta_0, \theta_1, \ldots, \theta_N, t_i) - \frac{F(t_i)}{2} \right)^2. \tag{4.39}$$

Such an approach has succeeded in our particular case of Eq.(4.34) and tested against benchmark solutions (see below Eqs.(4.40) and (4.41)) in reaching pre-assigned accuracy. If the required time step is small, i.e. the number N is large, though, Eq.(4.39) might require evaluation and inversion of large N-by-N Jacobians in the degrees of freedom and the computation might become expensive. A fix can be the subdivision of the total time in smaller subintervals and the iterative application of the method.

4.3 Numerical results

Here we explore numerically the consequence of the pressurized fluid on the mechanical behavior of the joint.

The solution to the problem Eq.(4.29) can be obtained independently on the application of the minimization procedure described by Eq.(4.39) in two liming scenarios:

1. negligible contribution of the fluid. It is the case, for example, when the membrane tension $T \to 0$. In this case, the mass conservation condition becomes irrelevant. The membrane can extend indefinitely and without the fluid arising. Only the second of Eq.(4.29), the vertical equilibrium, has to be solved and it gives

$$a(t) = \left(\frac{45R}{2m}\mathcal{K}[F](t)\right)^{1/5}. \tag{4.40}$$

2. negligible contribution of the contact to balance. This is the case when the fluid pressure and the membrane tension support all the load $F(t)$, for instance because the biphasic material is extremely soft ($m \to 0$). If the cartilage layer does not contribute to sustain the load, the mass conservation is unvaried. The balance Eq.(4.23), instead, must not include the first term anymore. It leads to

$$\left(\frac{d}{r(\theta)} - \cos\theta\right) T(\theta) - \frac{F(t)}{2} = 0, \tag{4.41}$$

which is not an integral equation any longer, reducing to a non-linear equation in only θ (or a), at every time.

Such a preliminary considerations allows us to obtain analytical solutions for both checking our computations and comparing our results to what would happen if cartilage and synovial membrane acted alone.

To the best of our knowledge, mechanical characterization has not been carried out on the properties of the synovial membrane. Within the scope of this work, we are interested in reasonable guesses. Looking for example at Wegst and Ashby [182], Moeendarbary and Harris [183] and considering the membrane to have a similar stiffness as tendons, one could expect the membrane Young's modulus to be of the order of a hundred times the one of cartilage. For a healthy human, the membrane is about five times thicker the articular cartilage layer (e.g. Smith and Wechalekar [184]). Let us call s the ratio between the cartilage and the membrane Young's moduli

$$s = E_m/E_c. \tag{4.42}$$

Then the parameter S of Eq.(4.17) is expressed as

$$S = \frac{s}{l_0} E_c 5 h_c \tag{4.43}$$

with the dimensionless s to be chosen of the order of 10^2.

If not specified, the cartilage E_c and permeability k_c are the same as the isotropic homogeneous ones used in Sec.3.3. Also, the thickness h_c is 1.3mm. The curvature radius of the articular surface R is 25mm and

$d/R = 1$. Following Ateshian et al. [52], Argatov and Mishuris [139], the parameters of Eqs.(4.1)-(4.4) are

$$m = \frac{3E_c}{2h_c^3}, \qquad \chi = \frac{3E_c k_c}{2h_c^2}. \tag{4.44}$$

Since the asymptotic solution Eq.(4.1) is valid only for a large contact width-tissue thickness ratio, the load F can not coherently start from zero. Hence, there is an initial non-zero contact width $2a_0$ and pressure. For the sake of simplicity, within the numerical benchmarks, we consider that the membrane is unstressed at $t = 0$, when its length $l = l_0$: the prestress T_0 is not needed and than set to zero together with the initial fluid pressure. The initial a_0 is obtained via Eq.(4.40). The membrane is not straight at this time, but described by an initial angle $\theta_0 = \pi/4$.

As in Sec.3.3 we simulate a constant three-dimensional body weight of 700N. In order to translate it into a two-dimensional setting, we distribute it on a rectangle with an aspect ratio of 10 and a width of $2a_0$.

Firstly, we want to investigate the sheer effect of the membrane stiffness. In Fig.4.4, the contact displacement is shown for different values of s. It is clear that the contact becomes increasingly stiff when the membrane is able to exert a considerable confining effect. Within the fluid-cartilage bearing, it is interesting to evaluate which part of the external load is destined effectively to the cartilage if one considers the presence of the synovial membrane. The most immediate way for doing it is via Eq.(4.15). Since the cavity fluid pressure $P_f(t)$ and the half-width of the contact

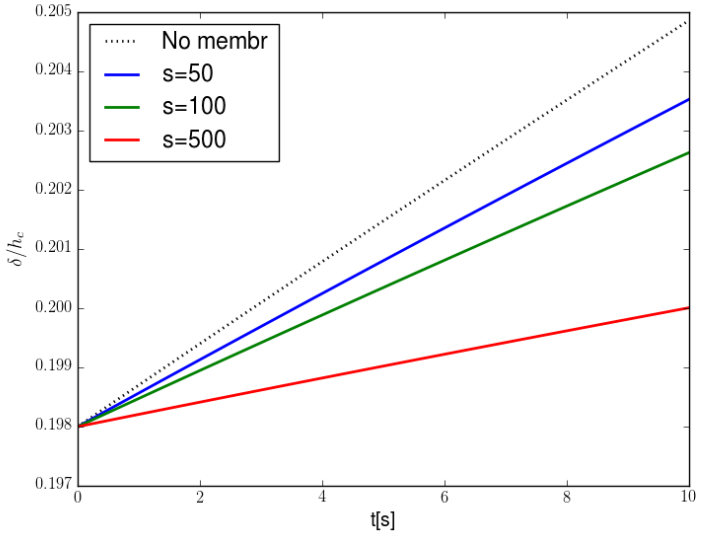

FIGURE 4.4: Influence of the membrane stiffness on the contact displacement under a constant force. The ratio s ranges between 50 and 500. The black lines refer to the limiting cases: the dotted one simulates the absence of fluid confinement Eq.(4.40), the thick one is in the case that only capsule pressurization sustains the load.

$a(t)$ are known, the effective force on the cartilage is

$$F_c(t) = \frac{m}{45R}\mathcal{K}^{-1}[a^5](t) + 2a(t)P_f(t). \tag{4.45}$$

A conspicuous influence of a stiff membrane in slowing down $\delta(t)$ would suggest that the contact is absorbing a small portion of the external load F. Nevertheless, in Fig.4.8 we observe that, in the first 10s, even the presence even of a membrane with $s = 500$ is not subtracting the cartilage much more than 3% of the burden. The situation is pretty similar with regards to the peak pressure reduction thanks to the pressurization

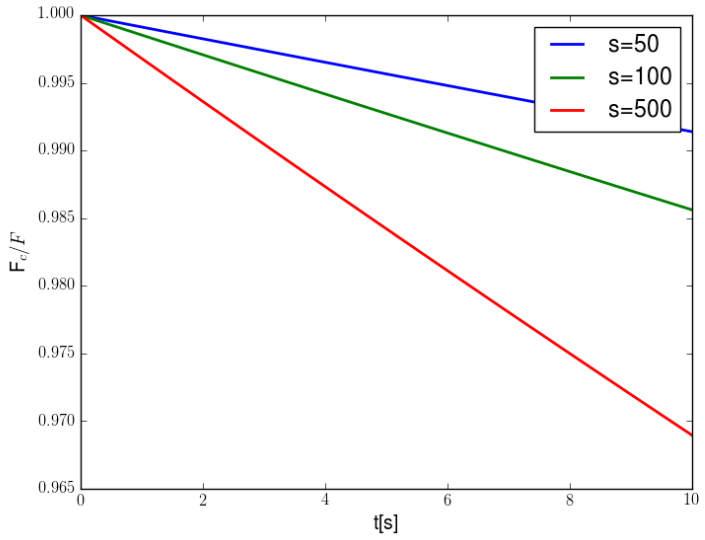

FIGURE 4.5: Influence of the membrane stiffness on the effective force portion absorbed by cartilage. The ratio s ranges between 50 and 500. One on the vertical axis is the reference case without membrane (i.e. $s = 0$).

of the joint capsule (see Fig.4.9). Only a modest advantage in terms of cartilage solicitation arises when the synovial membrane is impermeable under a constant vertical load for healthy humans, for whom the present material properties are representative. Secondly, we attempt to estimate what might change for a joint affected by arthritis or similar dysfunctions which are associated to degeneration of cartilage. Experimental investigations were conducted by Herzog et al. [11], Mäkelä et al. [12] on healthy and osteoarthritic joints of mammals. In both cases, it was very manifest that damaged cartilage sees stiffness decreasing, permeability increasing. In order to numerically reproduce such a scenario

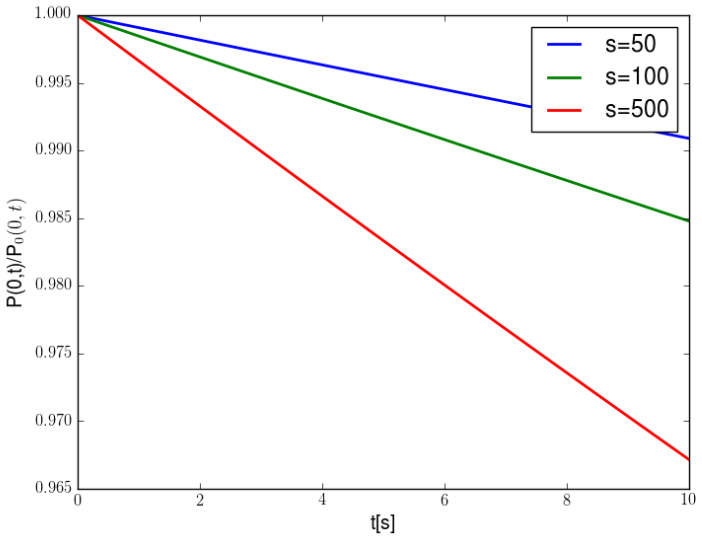

FIGURE 4.6: Influence of the membrane stiffness on the contact peak pressure $P(0,t)$ in the middle of the contact area. The ratio s ranges between 50 and 500. The pressure is normalized with respect to the peak pressure $P_0(0,t)$ which would occur in the reference case without membrane (i.e. $s = 0$).

in our model, we use a ten-fold increment in cartilage permeability with respect to the previous benchmark. This is the same order or magnitude of the experimental findings cited above. The Figs.4.7,4.8,4.9 show that in the case of osteoarthritic joints the effectiveness of an impermeable capsule is dramatic. The load part which is transferred past the joint via the cartilage contact can be reduced up to 10-15% if the membrane is 100 times stiffer than the solid part of the biphasic tissue. Coupling these results with reduced cartilage Young's modulus E_c are even more dramatic and not shown here.

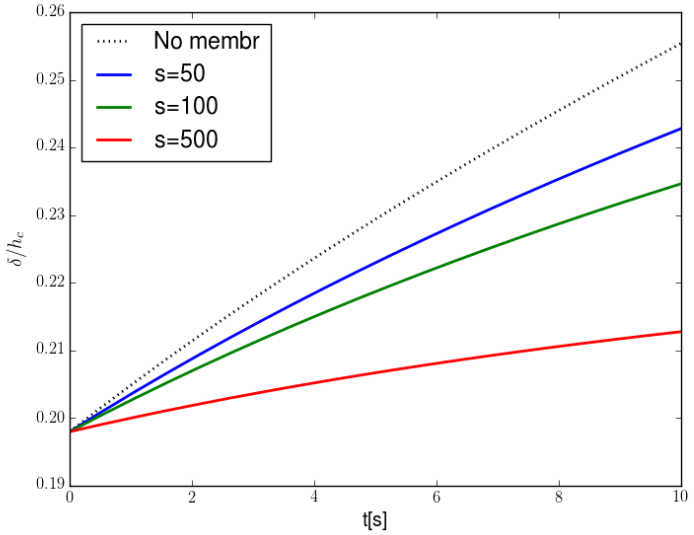

FIGURE 4.7: Osteorthritic joints: influence of the membrane stiffness on the contact displacement under a constant force. The ratio s ranges between 50 and 500. The black lines refer to the limiting cases: the dotted one simulates the absence of fluid confinement Eq.(4.40), the thick one is in the case that only capsule pressurization sustains the load.

Fig.4.10 shows the evolution of intra-articular pressure and membrane tension in the case of increased cartilage permeability. We notice a reasonable agreement, at least in terms of order of magnitude, with the in-vivo measurements of synovial fluid pressure by Jawed et al. [79]. The entity of membrane tension does not seem to be any close to the strength of ligaments (e.g. Wegst and Ashby [182]), which means that the functionality of capsule mechanism can be effectively maintained.

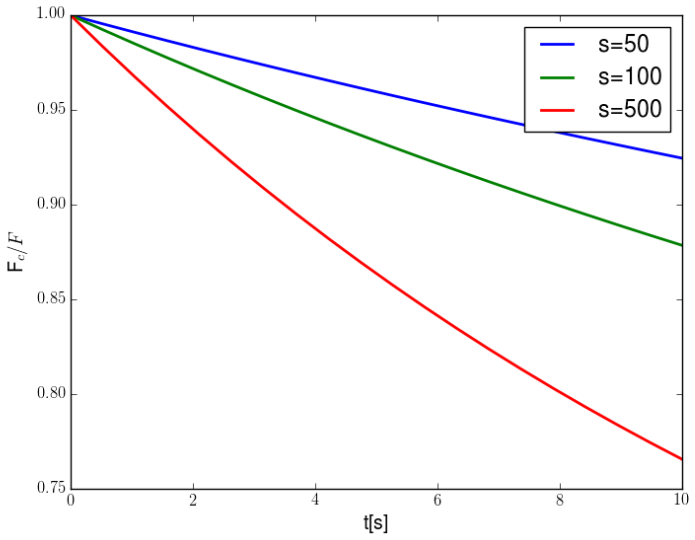

FIGURE 4.8: Osteorthritic joints: influence of the membrane stiffness on the effective force portion absorbed by cartilage. The ratio s ranges between 50 and 500. One on the vertical axis is the reference case without membrane (i.e. $s = 0$).

4.4 Remarks

High intra-articular pressure has been regularly measured in patients affected by articular disorders. We wonder whether it is high pressure which causes cartilage damage or rather a deteriorated articular articular surface which necessitates for an increase in cavity pressure. It has been asked whether we understand enough about capsules mechanics and relation to the body optimum Rutherford [185].

In order to answer such a question, we set a two-dimensional problem

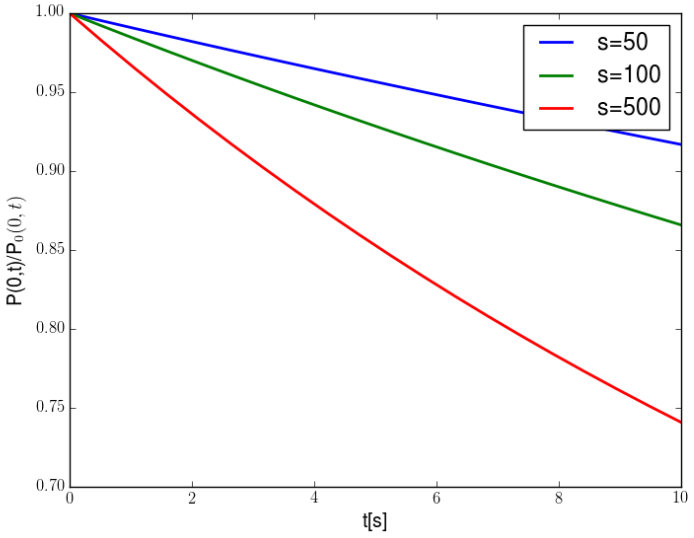

FIGURE 4.9: Osteorthritic joints: theoretical prediction of the influence of membrane stiffness on the contact peak pressure $P(0,t)$ in the middle of the contact area. The ratio s ranges between 50 and 500. The pressure is normalized with respect to the peak pressure $P_0(0,t)$ which would occur in the reference case without membrane (i.e. $s = 0$).

inside the joint where: the cartilagineous tissue is modelled as biphasic, isotropic and homogeneous; the intra-articular fluid is inviscid; the synovial membrane is impermeable and linearly elastic. The governing equations are mass conservation and equilibrium.

It turns out that, as contact displacement and contact width are univocally related, mass conservation is not time dependent and provides a relation between bone approach and shape of the membrane. With this in hand, equilibrium, which is history dependent because of the biphasic

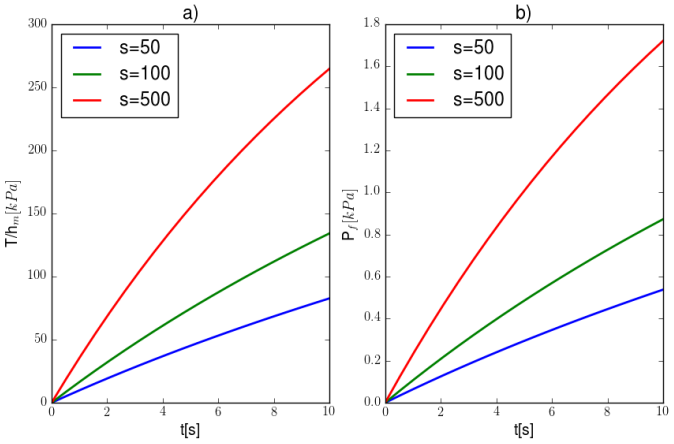

FIGURE 4.10: Osteorthritic joints: theoretical prediction of a) membrane stress obtained as T/h_m and b) intra-articular pressure P_f.

nature of cartilage, can be stated as an Volterra integral equation to be solved numerically.

Following the experience of Ferguson et al. [93, 94], we question whether, besides the disadvantage of stressing the membrane, there is at least one direct mechanical advantage for swelling and pressurization in joints. We examine joints where the labrum is not responsible for constraining the fluid and, instead of having a thin film, a consistent volume is present. The parameter responsible for pressurization, according to the elastic version of Laplace's law in Eq.(4.18) is the membrane stiffness.

We observe numerically that the coupled mechanism of contact and pressurization is not much more fruitful than just contact. For the simulated diseased joints, though, it becomes essential that the mechanism of intra-articular self-pressurization stays functional. This can happen, of course,

at the expensed of membranal elongation and stress, which might be the origin of pain. If new intra-articular fluid is injected into the cavity by the organism, the pressure would increase even further. Hence, the external load would be transmitted even more decisively via the intra-articular fluid than via direct contact.

Besides, the synovial membrane thickens when ligaments are damaged. After some time, the cartilage is damaged (Lukoschek et al. [186]). In this work's perspective it might be inferred that the thickening is not the cause of articular disorders, but a late attempt of saving the cartilage by increasing its stiffness. Both effusion and membrane thickening are rather a sign than a self-standing problem.

Further work can be done for studying lubrication inside the contact and investigating the dependence of friction of high fluid pressure at the border of the contact.

Chapter 5

Analysis of residual stresses in thermoelastic multilayer cylinders

We solve here the general plane strain axisymmetric problem of deformation in thermoelasticity which involves a cylinder inscribed into a series of concentric rings. The scientific interest in this configuration springs from practical applications such as layered or fiber-reinforced ceramics. The former analysis performed by Stucu [112] presented a simple recursive algorithm which considers only two concentric cylinders at a time. More recent investigations (Zhang et al. [113], Vedeld and Sollund [114]) extended the analysis to 3D residual stresses and pressurized hollow cylinders, while the contact between the layers was ideal. Our simple analytical solution can be advantageously adopted for following the residual

stresses which derive from the difference of the interfacing materials or from the provided prestresses and very thin layers can be substituted via appropriate transmission conditions. Qualitative observations can be addressed by examining different components distribution inside the multilayer structure. Particularly, a graded distribution with respect to thermal expansion coefficients is illustrated. The engineering concern is mainly about the possibility allowed by the design to give place to compressive zones. Holding on the same structure and simply modifying Young's modulus of one of the layers, the additional effect of the presence of a soft layer is studied.

5.1 Mechanical Model

The equilibrium, constitutive and kinematic equations in linear thermoelasticity for an isotropic material are

$$\nabla \cdot \boldsymbol{\sigma} = 0, \tag{5.1}$$

$$\boldsymbol{\sigma} = \mathbf{C}(\boldsymbol{\varepsilon} - \mathbf{I}\hat{\alpha}\Delta T), \tag{5.2}$$

$$\boldsymbol{\varepsilon} = \frac{1}{2}\left(\nabla \mathbf{u} + \nabla \mathbf{u}^T\right), \tag{5.3}$$

where $\boldsymbol{\sigma}$, $\boldsymbol{\varepsilon}$ and $\mathbf{u}$ are the stress tensor, the strain tensor and the displacement vector; $\mathbf{C}$, $\mathbf{I}$ the stiffness and and the identity tensors; $\hat{\alpha}$ and ΔT the coefficient of thermal expansion and the difference between the current temperature and the strain reference one. If two materials (1) and (2) are in contact by means of a very thin interphase, this can be classified

differently depending on the relationships between its elastic properties and the surrounding media and mathematically substituted by transmission conditions (see our Section 2 and the publications Klarbring and Movchan [30], Mishuris [31], Avila-Pozos et al. [187], Benveniste [188]). The interval of thickness at which the interphase does not influence the effective homogenized properties of a composite, together with the correlations between different imperfection models has been for instance addressed in Sevostianov et al. [115]. Sticking to the definitions given by Benveniste and Miloh [189], three cases are considered in the present work: perfect, *spring-type* (soft) and *membrane-type* (stiff) interfaces.

Let us consider the linear elastic deformation problem of a long axisymmetric structure undergoing an axisymmetric thermal and mechanical loading, so that its behavior can be adequately described in as axisymmetric plane strain. The only coordinate along which variable quantities arise is the radial one, say r, being θ and z respectively the angular and axial coordinates; λ, E and ν the material Lamé's first parameter, Young's modulus and Poisson ratio. Our scope is to generalize the problem of a cylinder encircled by an arbitrary number n of concentric layers, each of them characterized by possibly different thermomechanical parameters. An assigned uniform load or displacement on the outer border is also considered.

General number of layers The solution for each of the $n+1$ bodies (i) is written by the fields Eq.(5.4) and (5.5). If $\alpha^{(i)} = (1+\nu^{(i)})\hat{\alpha}^{(i)}$ is the coefficient of thermal expansion in plane strain for the i-th body

(proportional to the classical coefficient $\hat{\alpha}$), then

$$u_{rr}^{(i)} = (a^{(i)} + \alpha^{(i)}\Delta T^{(i)})r + \frac{b^{(i)}}{r}, \tag{5.4}$$

$$\sigma_{rr}^{(i)} = \frac{\lambda^{(i)}}{\nu^{(i)}}\left[a^{(i)} - (1-2\nu^{(i)})\frac{b^{(i)}}{r^2}\right], \qquad (i = 0, 1..., n). \tag{5.5}$$

The superscript (0) labels the inner cylinder and $b^{(0)} = 0$ descends from the symmetry condition. If the materials are not in mutual contact in their undeformed configuration they are assembled in such a way that the external radius of the i-th element is forced elastically to fit the internal radius of the $(i+1)$-th one – namely *prestressed*. It would be the case, for instance, of a cylinder which is inserted into a heated up ring before a homogeneous temperature is reached by the composite. The initial geometry of the multilayer body is completely described by the inner cylinder radius $R_2^{(0)}$ and by the internal and external radii $R_1^{(i)}$ and $R_2^{(i)}$ for each i-th ring $(i = 1, 2, ..., n)$, with the subscripts 1 and 2 meaning *internal* and *external* (see Fig.5.1).

In presence of soft contact, the equality of the radial displacements at the two sides of an interface is not guaranteed. Let $\beta^{(i)}$ be both the radial softness of the thin connecting layer (i) between the components (i) and $(i-1)$. *Spring-type* transmission conditions lead to the boundary value problem:

$$u_2^{(i-1)} - u_1^{(i)} + \sigma_1^{(i)}\beta^{(i)} = R_1^{(i)} - R_2^{(i-1)}, \tag{5.6}$$

$$\sigma_2^{(i-1)} - \sigma_1^{(i)} = 0, \tag{5.7}$$

with $i = 1, 2, ..., n$. From now on, where not specified, we refer simply to stresses σ and displacements u indicating radial ones, omitting subscripts for the coordinate system. The conditions in Eq.(5.7) can be efficiently adopted, also in dynamics, to represent a thin interphase layer whose stiffness is smaller than the surrounding materials. The introduction of such an interphase is indeed absolutely common for arresting crack propagation, as discussed at the beginning of Section 1.3. The right-hand side of Eq.(5.6) can turn useful in the case of stiffer interfaces, when the necessity may arise of preserving the interphase gap via springs, e.g. in order to correctly estimate the scattering amplitude under dynamic loadings (Huang et al. [190]). If the i-th interface, instead, is of *membrane type* with stiffness $\gamma^{(i)}$, the previous two equations are substituted via:

$$u_2^{(i-1)} - u_1^{(i)} = R_1^{(i)} - R_2^{(i-1)}, \tag{5.8}$$

$$\sigma_2^{(i-1)} - \sigma_1^{(i)} + \gamma^{(i)}(u_1^{(i)} + R_1^{(i)}) = 0. \tag{5.9}$$

An ideal contact is taken into account simply setting $\beta^{(i)}$ and $\gamma^{(i)}$ to zero. The outer boundary condition (BC) both in terms of axisymmetric uniform load $\overline{\sigma}$ (σ-BC) or radial uniform displacement $\overline{u}$ (u-BC) can be added by the equation:

$$\sigma_2^{(n)} = \overline{\sigma} \quad \text{or} \quad u_2^{(n)} = \overline{u} \tag{5.10}$$

Being the $n+1$ unknowns $a^{(0)}$ and the n couples $a^{(i)}$-$b^{(i)}$, the problem is completely stated by the set of $2n$ equations Eq.(5.6)-Eq.(5.7) or Eq.(5.8)-Eq.(5.9) plus Eq.(5.10). For the sake of conciseness, it is useful to the

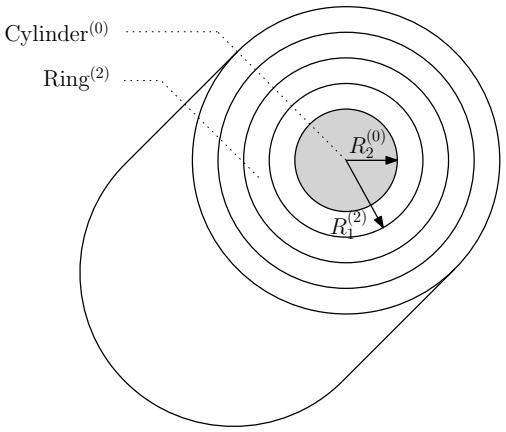

FIGURE 5.1: Schematic undeformed configuration of a non-prestressed cylinder surrounded by multiple rings.

define the following vectors and matrices ($i = 1, 2, ..., n$):

$$\mathbf{M}_2^{(0)} = \begin{bmatrix} R_2^{(0)} \\ \frac{\lambda^{(0)}}{\nu^{(0)}} \end{bmatrix}; \qquad \mathbf{M}_2^{(i)} = \begin{bmatrix} R_2^{(i)} & \frac{1}{R_2^{(i)}} \\ \frac{\lambda^{(i)}}{\nu^{(i)}} & -\frac{\lambda^{(i)}}{{R_2^{(i)}}^2}\frac{1-2\nu^{(i)}}{\nu^{(i)}} \end{bmatrix}; \tag{5.11}$$

$$\mathbf{M}_1^{(i)} = \begin{cases} \text{soft interface:} & \begin{bmatrix} R_1^{(i)} - \frac{\beta^{(i)}\lambda^{(i)}}{\nu^{(i)}} & \frac{1}{R_1^{(i)}} + \frac{\beta^{(i)}\lambda^{(i)}}{{R_1^{(i)}}^2}\frac{1-2\nu^{(i)}}{\nu^{(i)}} \\ \frac{\lambda^{(i)}}{\nu^{(i)}} & -\frac{\lambda^{(i)}}{\nu^{(i)}}\frac{1-2\nu^{(i)}}{{R_1^{(i)}}^2} \end{bmatrix} \\ \text{stiff interface:} & \begin{bmatrix} R_1^{(i)} & \frac{1}{R_1^{(i)}} \\ \frac{\lambda^{(i)}}{\nu^{(i)}} - \gamma^{(i)}R_1^{(i)} & -\frac{\lambda^{(i)}}{{R_1^{(i)}}^2}\frac{1-2\nu^{(i)}}{\nu^{(i)}} - \frac{\gamma^{(i)}}{R_1^{(i)}} \end{bmatrix} \end{cases}; \tag{5.12}$$

$$\mathbf{B}_2^{(n)} = \begin{cases} \text{with } \sigma\text{-BC:} & \frac{\lambda^{(n)}}{\nu^{(n)}}\begin{bmatrix} 1 & -\frac{(1-2\nu^{(n)})}{{R_2^{(n)}}^2} \end{bmatrix} \\ \text{with } u\text{-BC:} & \begin{bmatrix} 1 & \frac{1}{R_2^{(n)}} \end{bmatrix} \end{cases}. \tag{5.13}$$

The whole set of $2n$ conditions takes the form

$$\mathbf{M}\mathbf{a} = \mathbf{d}, \tag{5.14}$$

where the following assembly holds:

$$\mathbf{M} = \begin{bmatrix} \mathbf{M}_2^{(0)} & -\mathbf{M}_1^{(1)} & & & & & & & \\ & \mathbf{M}_2^{(1)} & -\mathbf{M}_1^{(2)} & & & & & & \\ & & \ddots & \ddots & & & & & \\ & & & \mathbf{M}_2^{(i-1)} & -\mathbf{M}_1^{(i)} & & & & \\ & & & & \ddots & \ddots & & & \\ & & & & & \mathbf{M}_2^{(n-1)} & -\mathbf{M}_1^{(n)} & \\ & & & & & & & \mathbf{B}_2^{(n)} \end{bmatrix}; \tag{5.15}$$

$$\mathbf{a}^T = \begin{bmatrix} a^{(0)} & a^{(1)} & b^{(1)} & \cdots & a^{(i)} & b^{(i)} & \cdots & a^{(n)} & b^{(n)} \end{bmatrix}. \tag{5.16}$$

The known terms are collected in the vector $\mathbf{d}$, whose components are

$$\begin{aligned} d_{2i-1} &= (1+\alpha^{(i)}\Delta T^{(i)})R_1^{(i)} - (1+\alpha^{(i-1)}\Delta T^{(i-1)})R_2^{(i-1)}, \\ d_{2i} &= \begin{cases} 0 & \text{(soft interface)} \\ -\gamma^{(i)}R_1^{(i)}(1+\alpha^{(i)}\Delta T^{(i)}) & \text{(stiff interface)} \end{cases}, \\ d_{2n+1} &= \begin{cases} \overline{\sigma} & \text{for } \sigma\text{-BC} \\ \overline{u} - \alpha^{(n)}\Delta T^{(n)}R_2^{(n)} & \text{for } u\text{-BC} \end{cases}, \end{aligned} \tag{5.17}$$

with $i = 1, 2, ..., n$. From a computational point of view it is useful to underline that $\mathbf{M}$ is a bidiagonal block matrix. Consequently a sweep method (see 5.2, Linkov and Filippov [191], Mishuris [192]) can be developed for its inversion, which takes into account that $\mathbf{B}_2(n) \in \mathbb{R}^{1\times 2}$ and

$\mathbf{M}_2^{(0)} \in \mathbb{R}^{2\times 1}$ are not invertible. It is clear that, once found the $2n+1$ constants contained in $\mathbf{a}$, they can be used for knowing displacements and stresses of every point of the domain.

If one needs to solve the similar problem of a hollow cylinder instead of a full one, it is sufficient ensure the first unknown $a^{(0)}$ to fulfill the internal boundary conditions in terms, for instance, of pressure or radial displacement constraints (see Eq.(5.4)-(5.5)). In that case the present solution enriches the work developed in Vedeld and Sollund [114] in the framework of pipe and vessels design through the availability of prestresses and imperfect interfaces.

5.2 A Sweep Method

Based on the approach adopted in Linkov and Filippov [191] for layered systems and expanded in Mishuris [192] to wedged-layered domains, for the sake of computational efficiency, we propose here a sweep method to solve the linear system stated in Eq.(5.14). Condensing the writing, we

set here the following abbreviations:

$$\begin{cases} \mathbf{M}_i = \mathbf{M}_2^{(i)}; \\ \mathbf{G}_i = -\mathbf{M}_1^{(i)}; \\ \mathbf{B} = \mathbf{B}_2^{(n)}; \\ a_0 = a^{(0)}; \qquad \mathbf{a}_i = \begin{bmatrix} a^{(i)} \\ b^{(i)} \end{bmatrix}; \\ d_e = d_{2n+1}; \qquad \mathbf{d}_i = \begin{bmatrix} d_{2i-1} \\ d_{2i} \end{bmatrix}; \end{cases} \tag{5.18}$$

Therefore, the system can be expressed as

$$\begin{bmatrix} \mathbf{M}_0 & \mathbf{G}_1 & & & \\ & \mathbf{M}_1 & \mathbf{G}_2 & & \\ & & \ddots & \ddots & \\ & & & \mathbf{M}_{n-1} & \mathbf{G}_n \\ & & & & \mathbf{B} \end{bmatrix} \begin{bmatrix} a_0 \\ \mathbf{a}_1 \\ \mathbf{a}_2 \\ \vdots \\ \mathbf{a}_n \end{bmatrix} = \begin{bmatrix} \mathbf{d}_1 \\ \mathbf{d}_2 \\ \vdots \\ \mathbf{d}_n \\ d_e \end{bmatrix}. \tag{5.19}$$

It is a bidiagonal block matrix. $\mathbf{B} \in \mathbb{R}^{1\times 2}$ and $\mathbf{M}_0 \in \mathbb{R}^{2\times 1}$ are not invertible, thus the method shown here is devised to fix this features. As start of forward sweeping, the second matrix equation is substituted by $\mathbf{G}_1\mathbf{M}_1^{-1}$ times itself minus the first equation. The variable $\mathbf{a}_1$ is eliminated, the variable a_0 appears:

$$-\mathbf{M}_0 a_0 + \mathbf{G}_1\mathbf{M}_1^{-1}\mathbf{G}_2\mathbf{a}_2 = \mathbf{G}_1\mathbf{M}_1^{-1}\mathbf{d}_2 - \mathbf{d}_1. \tag{5.20}$$

Or, defining $\mathbf{G}'_2 = \mathbf{G}_1\mathbf{M}_1^{-1}\mathbf{G}_2$ and $\mathbf{d}'_2 = \mathbf{G}_1\mathbf{M}_1^{-1}\mathbf{d}_2 - \mathbf{d}_1$:

$$-\mathbf{M}_0 a_0 + \mathbf{G}'_2\mathbf{a}_2 = \mathbf{d}'_2. \tag{5.21}$$

The method is substantially based on vanishing $\mathbf{a}_{i-1}$ and including a_0 in the i-th equation ($i = 2, ..., n$). The forward sweep, posed that $\mathbf{G}'_1 = \mathbf{G}_1$ and $\mathbf{d}'_1 = \mathbf{d}_1$, is therefore described by the following recursive formulae:

$$\text{for } i = 2, ..., n \quad \begin{cases} \mathbf{G}'_i = \mathbf{G'}_{i-1}{\mathbf{M}_{i-1}}^{-1}\mathbf{G}_i \\ \mathbf{d}'_i = \mathbf{G'}_{i-1}{\mathbf{M}_{i-1}}^{-1}\mathbf{d}_i - \mathbf{d}'_{i-1} \end{cases}, \tag{5.22}$$

so that the i-th equation takes the form

$$(-1)^n\mathbf{M}_0 a_0 + \mathbf{G}'_i\mathbf{a}_i = \mathbf{d}'_i. \tag{5.23}$$

The n-th Eq.(5.23), combined with the outer boundary condition, gives the 3×3 linear set of equations

$$\begin{cases} (-1)^i\mathbf{M}_0 a_0 + \mathbf{G}'_n\mathbf{a}_n = \mathbf{d}'_n \\ \mathbf{B}\mathbf{a}_n = d_e \end{cases}, \tag{5.24}$$

whose solution is

$$\begin{bmatrix} a_0 \\ \mathbf{a}_n \end{bmatrix} = \begin{bmatrix} (-1)^n\mathbf{M}_0 & \mathbf{G}'_n \\ 0 & \mathbf{B} \end{bmatrix}^{-1} \begin{bmatrix} \mathbf{d}'_n \\ d_e \end{bmatrix}. \tag{5.25}$$

With $\mathbf{a}_n$ in hand, a backward sweep can be started which finds the remaining $n-1$ vector variables

$$\mathbf{a}_i = \mathbf{M}_i^{-1}(\mathbf{d}_{i+1} - \mathbf{G}_{i+1}\mathbf{a}_{i+1}), \tag{5.26}$$

for $i = n-1, ..., 1$. It is probably worth to mention that the matrices $\mathbf{M}_i^{-1}$ are already computed during the forward sweep.

5.3 Residual Stresses in Multilayer Ceramics

The first benchmark computed via the present analytical exact solution is a multilayer structure of radius $R_2^{(n)} = 1\text{m}$. The i-th interface is situated at $r = iR_2^{(n)}/5$ except for the third one which at $0.4\text{m} + t$. The thickness t of the second layer is 2cm in the case A and is 2mm in the case B. The Young modulus and Poisson's ratio and the thermal load of the whole body are 30GPa, 0.222 and 907°K; the coefficient of thermal expansion is alternately $40°K^{-1}$ and $8°K^{-1}$ from the central component outwards. The plot in Fig.5.2 shows the good agreement, for the case A, of the results both in terms of radial and hoop stresses if compared to a finite element (FE) simulation. For the case B such comparison would remain, for practical purposes, unvaried. The situation changes if one refers to the errors. The dimensionless error of the FE solution with respect to

the analytical one (AN) for the stresses σ_{ii} $(i = r, \theta)$ is calculated as

$$\mathrm{err}_i = \frac{\sqrt{\sum (\sigma_{ii}^{(\mathrm{FE})} - \sigma_{ii}^{(\mathrm{AN})})^2}}{\max |\sigma_{ii}^{(\mathrm{AN})}|}.$$

In Fig.5.3 one can observe that, due to the tenfold reduced thickness of the layer (2) in the case B, the mesh required in a FE analysis to approximate the exact solution at the same level of accuracy is much finer than in the case A. As evident consequence, a highly increased computational effort is required and special domain decomposition techniques may be required (e.g. Dornisch et al. [193]). This is, after all, the reason for the introduction of imperfect interface conditions in presence of very thin layers in a similar fashion as derived in Klarbring and Movchan [30], Mishuris [31], Avila-Pozos et al. [187], Benveniste [188], Benveniste and Miloh [189]. The advantages of such mathematical approach have been widely exploited in engineering computations, demonstrating to be highly effective via finite and boundary elements analysis, by the way, applied to the design of elastic and piezoelectric structures (Geis et al. [194], Mishuris et al. [195, 196]), materials tests (Öchsner et al. [34]) or to improve the numerical performances in thermo-diffusive contact problems (Wrobel and Mishuris [197, 198]).

The simple mechanical model explored in the Section5.1 proves to be fruitful in characterizing a multilayer cylindrical ceramic structure, particularly attaining to production precautions. The layers are obtained usually by overlapping different ceramic powders and sintering the previously compacted so-called *green body* (e.g. Rahaman [199]). The goal

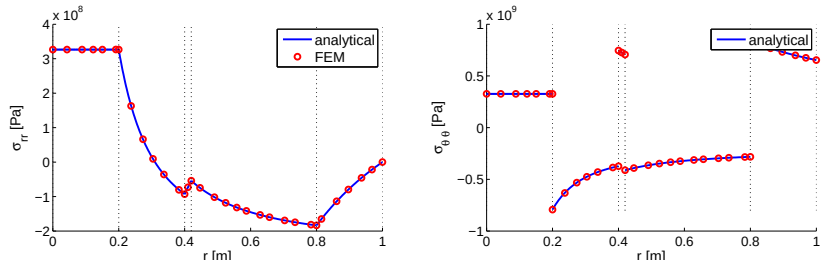

FIGURE 5.2: Comparison of the residual σ_{rr} and hoop $\sigma_{\theta\theta}$ stresses obtained for the case A by means of the analytical solution and a FE analysis run with COMSOL Multiphysics®. The mesh consists of 22710 triangular elements.

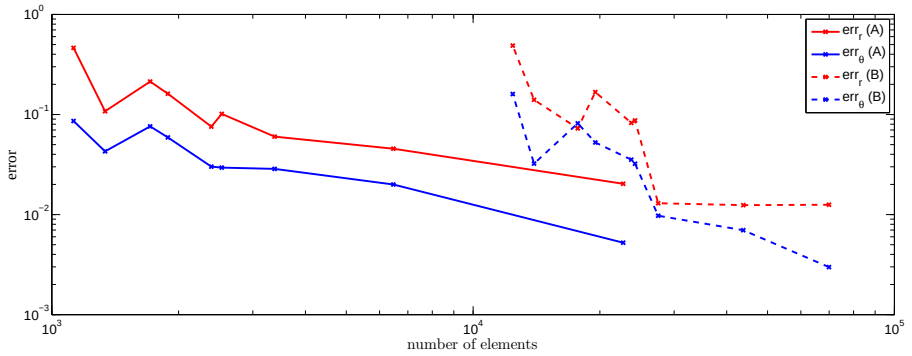

FIGURE 5.3: Convergence of the FE simulation run through COMSOL Multiphysics® toward the analytical solutions. The case A shows the results for a thin layer of 20mm, the case B of 2mm placed in a full cylinder of radius 1m.

is to fuse the constituent grains together. A cooling process starts thereafter, which must be accurately controlled in order not to give place to destructive fractures due to unexpected self-stress (Jagota and Hui [200]).

Lugovy et al. (Lugovy et al. [101]) presented the concept of *joining temperature* T_{join}: a temperature below which, during the cooling process,

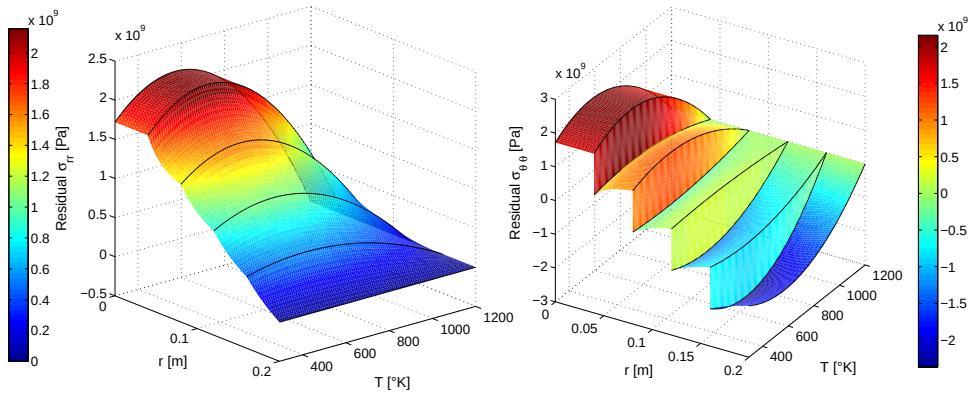

FIGURE 5.4: Evolution of the residual stresses with decreasing temperature from T_{join} to T_{room}. $E = E_{\text{ref}}(T)$ everywhere, $\hat{\alpha}^{(j)} = (5-j)\hat{\alpha}_{\text{ref}}(T)$ with $j = 0:4$.

two phases start to deform together under an ideal contact condition. The materials difference in thermal expansion properties and stiffness are the main origin of residual stresses inside the final product and such mismatches evolve during the temperature reduction. For the computation, we assume that:

- the thermal expansion coefficients increase with the temperature, both Young's moduli and the stress resistance vice versa, while Poisson's ratios remain constant with that respect (Lugovy et al. [100], Bruls et al. [201]);
- the above dependencies are linear;
- the cooling is performed relatively slowly so that the temperature gradient inside the structure at every moment is negligible.

It should be remarked that, in this analysis, the temperature has to be lower than the one at which the phase changes occur, since the positions of the interfaces must be known. It has been indeed proofed, based on thermodynamical considerations, that the combination of interface conditions Eq.(5.6)-(5.7) or Eq.(5.8)-(5.9) and boundary conditions Eq.(5.10) require to be treated accurately in the case of phase transition in order to ensure the stability of the solution (see Yeremeyev et al. [202]).

The geometry of the system for the following two benchmarks at the joining temperature is the same: a multilayer cylinder of radius 20cm is composed of equally spanned layers. Poisson's ratio is 0.3 everywhere. A joining temperature $T_{\text{join}} = 1200.15°\text{K}$ is considered for every interface. The reference temperature-dependent thermal expansion coefficient and Young's modulus are $\hat{\alpha}_{\text{ref}}(T) = 10^{-6}(1.5+0.037T)°\text{K}^{-1}$ and $E_{\text{ref}} = (390-0.02T)\text{Gpa}$. The structure is cooled uniformly down to room temperature $T_{room} = 293.15°\text{K}$ and the differences in material properties give place to residual stresses during the process. Attention is payed to the surface stresses which can be responsible of toughening at the macroscale or of changing the elastic response of the material at nanoscale, as for instance discussed by Altenbach et al. [203], Eremeyev [204].

Five different materials are assembled whose thermal expansion coefficients decrease 5 times from the surface layer toward the inner cylinder while every other parameter is kept constant along the radius. Such an arrangement causes the temperature stresses upon cooling plotted in Fig.5.4. It has been shown in Bermejo et al. [98], Rao et al. [99] that

the presence of compressive residual stresses results advantageous for enhancing crack bifurcation if the compression is perpendicular to the crack growth. Considering a fracture which propagates from the external surface inwards, the presence of residual compressive hoop stresses in the superficial layers is able to increase the fracture toughness. The scope appears to be reached thanks to the special arrangement hypothesized here. On the other hand, one can observe that tensile radial stresses at the interfaces may raise the risk of delamination. Moreover, the shielding from radial crack growth is not guaranteed in the case the crack nucleates in the core of the structure, which may be the understanding key, for instance, of the disintegrating fracture of Prince Rupert's drops (Calvert et al. [109], Johnson and Chandrasekar [110]).

The structure for which the residual stresses are shown in Fig.5.5 constituted of a graded material in the sense of thermal expansion coefficient. It ranges linearly along the radius from $\hat{\alpha}_{\text{ref}}$ at the symmetry axis to $5\hat{\alpha}_{\text{ref}}$ at the external surface – thus on the contrary as the example of Fig.5.4 – and discretized into 100 layers. As explained in Section 1.3, a common artifice to arrest the crack propagation is the provision of weak interlayers inside a brittle structure. The materials used to this purpose for engineering application or found in nature (e.g. see Munch et al. [205]) often present lower stiffness than the surrounding ones and larger failure strain with the result of an increased fracture work. In this benchmark, one of the layers is a soft thin circular layer introduced in the middle of the overall radius and it is characterized by a value of Young's modulus of $10^{-3}E_{\text{ref}}$, where E_{ref} is assigned to each other component. The behavior of such structure upon cooling, pictured in hatched surfaces in Fig.5.5,

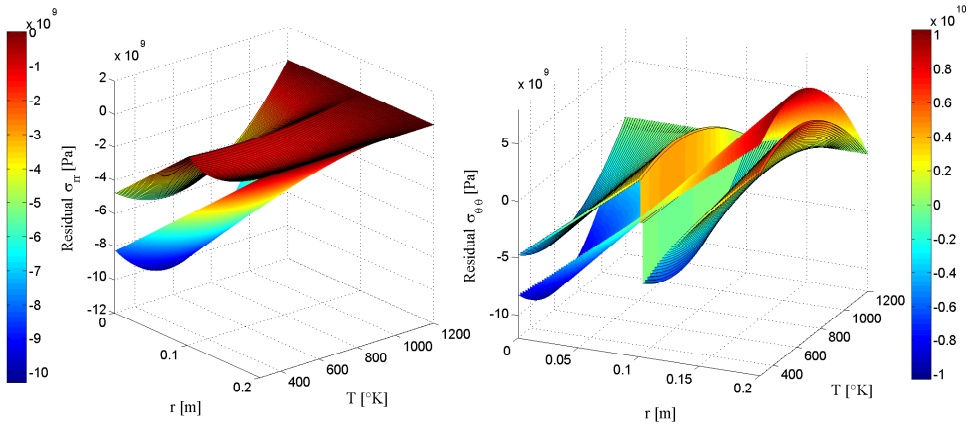

FIGURE 5.5: Evolution of radial and hoop residual stresses with decreasing temperature from T_{join} to T_{room} for a graded material in terms of thermal expansion coefficients whose αdecreases 5 times from the outer surface to the symmetry axis. Comparison between homogeneous Young's modulus E_{ref} (unshaded surfaces) and inhomogeneous with a soft internal layer of $E = 10^{-3}E_{\text{ref}}$ (hatched surfaces).

is compared to the same structure in absence of the soft layer, plotted in unshaded surface in the same figure. The effect of the soft element is a jump in the hoop stresses which allows to reduce, as expected, the surface tension of the cylinder, as well as approaching a compressive zone to the same surface which may work, as discussed dealing with the previous benchmark, to arrest a radial crack. However, it must be noticed that the residual radial compression is weakened, which is crucial when protecting the structure from delamination. It is the engineer who must choose, in the design phase, to what kind of danger risk the product will be most probably subjected during its service life and adopt an appropriate safety criterion, pragmatically via an optimization process.

5.4 Remarks

The plain strain deformation problem for a multilayer cylinder composed of an inner cylinder inscribed by a general number of annular layers is solved analytically in the case of mechanical loads or constraint and thermal expansion. The proposed solution includes also prestresses and three kinds of interface transmission conditions: perfect, membrane-type and spring-type. The reasons for the introduction of the aforementioned feature are made clear through a study of the disadvantages of a FE solution in presence of thin layers due to important mesh refinement required in the vicinity of the interfaces (see Fig.5.3). In that case, indeed, the computational efforts for reaching an acceptable accuracy largely increase with the reduced ratio between the thin layer size and the adjacent ones. The set of linear equations deriving from the present formulation has been solved efficiently applying a sweep method and illustrated in 5.2. The method was adopted for studying the uniform cooling of multilayer cylinders whose composing materials start to deform together below their joining temperature and whose thermoelastic parameters are temperature-dependent. Based on literature considerations regarding fracture toughness of composites, mainly ceramics, selected numerical examples show how different arrangements of thermal expansion coefficients or the inclusion of soft layers inside a stiffer environment are able to create residual stresses which can shield the structure from crack propagation.

Chapter 6

Conclusions

This work arises from the necessity of obtaining reliable mechanical predictions for structures containing thin layers. These are ubiquitous both in natural and man made objects. They are developed for performing highly specific tasks without representing bulky supplements to the main body.

Their central role requires adequate attention in mechanics. Nevertheless, when thin layers need to be incorporated in larger models, they can entail either disproportionate computational costs or return unreliable predictions. An escape can be found by pushing the mathematical analysis as far as possible and by designing ad hoc techniques. This thesis shows a number of applications where such an approach can be successfully put into practice. Interphases typical of mechanics and biomechanics are studied via appropriate governing equations and solutions are found

which can serve either for understanding their functioning or for designing artificial biomimetic devices.

A main effort is dedicated to the analysis of animal articular joints. Within this context, the most debated functional thin layer is articular cartilage. This soft tissue covers the bones extremity and works for improving the durability of the joint. Whereas bones are a masterwork of robustness and lightweight, they are extremely fragile and prone to wear. Cartilage is a complex stratum where different solid constituents, mainly fibers and matrix, are arranged in a way to allow fluid to fill the pores and circulate through them without leaving the surface. The results is a pressurized composite that can absorb shocks, distribute loads and lubricate the joint with near zero friction.

Its performance is guaranteed by many peculiarities, among whose anisotropy and inhomogeneity play as protagonists. The prevalent direction of the fibers, their size and the matrix porosity all vary considerably through the thickness. This causes the emerging mechanical stiffness and permeability to also be depth dependent.

We have provided, in Chapter 2, the first analytical solution for an inhomogeneous biphasic tissue in terms of surface load versus deformation. The result is achieved by exploiting the thinness of the layer in an asymptotic formulation. The retrieved closed-form formulae can be seen as fully-fledged transmission conditions and thus they might be used in order to implement zero-thickness interphase elements in more traditional mechanical analysis such as finite elements. Internal stresses can be predicted by also taking into account the distinction between solid and

interstitial fluid, anisotropy and inhomogeneity. This is key if one considers that cartilage is avascular, with low chances of regenerating, and that its eventual damage is to be attributed to tear and wear phenomena.

Next step is quite straightforward. We have used the results of the deformation problem of a single layer in order to investigate the evolution of the contact between two articular surfaces. Such challenge can not be tackled by means of known existing solutions because they all refer to half-spaces, i.e. the indented surface belongs to an infinitely thick body. In Chapter 3, we have considered a three-dimensional geometry where elliptic paraboloids are covered by anisotropic, inhomogeneous biphasic tissues. We have solved the problem, which mathematically arises in the form of integral-differential equations, again in closed-form. By means of the resulting relations, we have found an undiscovered explanation of in-vivo measurements obtained by imaging human knees in real time. Furthermore, we have hypothesized that the specific distribution of material properties in animal cartilage is an optimal arrangement for spreading the loads onto the subchondral bone by comparing our novel results with the existing ones for isotropic homogeneous models.

Further work in this subject and formulation can be done at minimum in two directions. Firstly, it has been known for decades that cartilage permeability is dependent on its strain. It is indeed intuitive that, upon compression, the interstitial pores shrink and fluid flow becomes more difficult. Our constitutive equations can be modified in order to account for this. The model would be able to describe larger deformations at longer times.

Secondly, a more technical side of the approach can be deepened. If the solution is concretely embedded in special zero-thickness elements, more realistic geometries for the contact can be implemented in a numerical scheme. This would be a fundamental step that would allow to take advantage of the near nil computational costs in order to perform fast assessments. The goal of obtaining real time patient-specific diagnoses to degenerative joint pathologies would be some closer.

Articular cartilage is part of the synovial joint in company of various other tissues. One of those is the synovial membrane. This envelops the kernel of the joint by keeping the confluent bones and avoiding loss of fluid that fills the cavity. This fluid contains some nutrients and lubricates the contact. In the past there has been some interest in understanding whether more engaging tasks are carried out by it. The debate is not conclusive. In Chapter 4, we hypothesize that, if the membrane is stiff enough, such a fluid can pressurize at the expenses of membrane stress and provide some enhanced redistribution of the load. In order to test the hypothesis, we create a simplified two-dimensional model. Whereas not the case for healthy joints, it results that for diseased cartilage the contribution of the coupled mechanism can be relevant. In theory, animals can effectively use fluid pressurization for subtracting part of the burden from the surface-to-surface contact.

This claim has surely to be confronted by experimental validation before being considered conclusive. Existing imaging techniques can already be used to track contact displacement and cartilage deformation. Intra-articular pressure measurements have been done decades ago. By

using in-silico models, contact pressure can be predicted. Comparative tests between healthy and diseased joints, with effective and non effective constraining synovial membranes can reveal the entity of the double mechanism investigated.

From a mathematical point of view, the three-dimensional case can be studied and we expect that the main challenge can descend from the mechanics of the membrane. The axis-symmetric case is at hand though. Furthermore, it would be interesting to estimate the influence of the articular pressure on cartilage lubrication. The thin film of fluid which allows highly reduced friction in the contact obeys the theory of lubrication. The results that we have obtained for the fluid in the cavity would be used as moving boundary conditions for the lubrication equations.

When particular parts of human articular joints need to be replaced, ideal candidates are materials with similar friction features. Ceramics, for instance, perfectly match such a description. They are chemically inert, bio-compatible and can be easily shaped at will. They guarantee longer performances than metals. Crucially, various layers can be easily created with different powders and compositions in order to accomplished different physical tasks. One can engineer a multilayer which, imitating nature, is very porous inside and denser on the outer surface where wear should be avoided. A variety of combinations can be fine tuned for improving toughness, thermal, piezo-electrical properties and so on.

These materials have a main flaw in being brittle and complicated to test once they have been fired together. If internal cracks develop, possibly

at the interfaces between different powders, they can hardly be spotted. Careful and controlled production processes become inescapable.

In Chapter 5, we have solved the axis-symmetric thermoelastic problem of a general number of layers assembled together. The model also includes imperfect contact between adjacent layers whose parameter can be useful for incorporating transmission conditions deriving by the presence of thin interphases. All the strata have arbitrary thermal coefficients and elastic properties. The external solicitation can be exerted either by constrained displacement or load. We have discussed how residual stresses can arise upon steady-state changes of temperature which have beneficial or detrimental effects globally.

The model can be augmented in order to consider different physics and geometry. It can be used for explaining and predicting residual stresses. Once the axis-symmetric assumption is removed, fracture propagation can be studied and the results applied in order to design robust and efficient structures. A particularly puzzling phenomenon yet to be effectively modelled is self-sustaining fracture. Mechanical energy accumulates in the form of residual stresses upon differential phase transition. The equilibrium is unstable and even a minimal perturbation sees a self-destruction wave exploding all the piece without external energy being introduced. The study of this fascinating phenomenon would lay a bridge between the model of Chapter 5 and the analyses of dynamic fracture propagation in Appendix B.

In conclusion, various thin functional layers have been studied. Their mechanics has been described by appropriate governing equations. The chosen mathematical strategies for the solution of relevant problems in mechanics and biomechanics have been shown. Effective numerical schemes have been implemented when closed-form solutions were not achievable. Real world phenomena have been investigated by means of the constructed models. Physical relevance of constitutive parameters has been highlighted via benchmarks. Technological applications and experimental validations, deriving from analytical and numerical observations, have been prospected.

Appendix A

How the Fibonacci sequence and the golden ratio describe the pulling of an elastic chain

A semi-infinite chain is made of infinite equally spaced nodes of coordinates x_n connected to each other and to a rigid substrate via identical elastic bonds of stiffness k as in Fig.A.1. The equilibrium of the n-th node for small displacements fulfills

$$k(u_{n-1} - u_n) - ku_n + k(u_{n+1} - u_n) = 0 \qquad \rightarrow \qquad 3u_n = u_{n-1} + u_{n+1}. \tag{A.1}$$

If an external force F is applied at the extreme point x_0, every displacement u_n can be described in cascade as sum of a contribution due to the

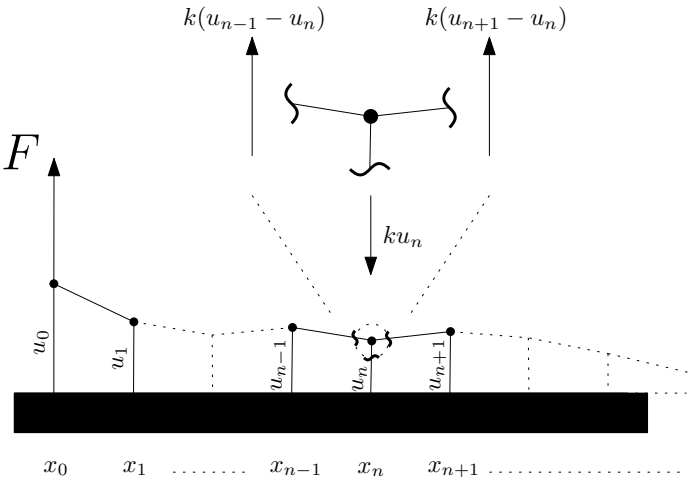

FIGURE A.1: System geometry and applied load.

force and one due to the displacement of the first point u_0 as

$$u_n = -c_{2n-1}\frac{F}{k} + c_{2n}u_0 \tag{A.2}$$

because of the linearity of the problem. A sequence c_n is created which, by equating the coefficients of F/k and u_0 at every x_n, allows to turn Eq.(A.1) into the infinite set of simultaneous equations:

$$\begin{cases} c_{2n+1} + c_{2n-3} - 3c_{2n-1} = 0 & \text{(A.3)} \\ c_{2n+2} + c_{2n-2} - 3c_{2n} = 0 & \text{(A.4)} \end{cases}$$

Simple subsequent arithmetical substitutions are required in order to show that the recurrence relation

$$c_{2n} = c_{2n-1} + c_{2n-2} \tag{A.5}$$

automatically satisfies Eqs.(A.3)–(A.4). In other words, the coefficients c_{2n-1} and c_{2n-2} are two adjacent terms of a sequence which possesses the same recurrence relation as the Fibonacci sequence. The two seed values are established together with the equilibrium of the first node

$$\frac{u_1}{u_0} = -\frac{F}{ku_0} + 2, \tag{A.6}$$

according to which, by comparison Eq.(A.2),

$$c_1 = 1 \qquad \text{and} \qquad c_2 = 2 \tag{A.7}$$

Thus the sequence c_n results in fact the Fibonacci sequence if u_0 is used as unit measure of the lengths and ku_0 of the forces. The displacement of a point infinitely far from the force must be zero because the finite work of the force at x_0 can not cause an infinite potential energy. Setting to zero Eq.(A.2) at infinity, gives

$$\frac{F}{ku_0} = \lim_{n\to+\infty} \frac{c_{2n}}{c_{2n-1}} = \varphi. \tag{A.8}$$

A golden ratio force is necessary to lift x_0 up of one with unitary bond stiffness. The stiffness of the structure at x_0 is φ times bigger than the one of the constituent bonds. For every n, the displacement is then finally retrieved as

$$\frac{u_n}{u_0} = -c_{2n-1}\varphi + c_{2n} = \varphi^{-2n}. \tag{A.9}$$

The vertical displacements of the first ten nodes of the chain, calculated as above, are displayed in Fig.A.2. At this point one may object that the global equilibrium of the structure is not enforced. The center of gravity

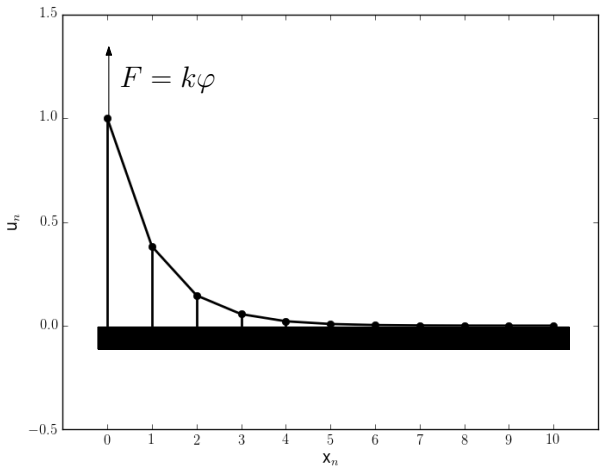

FIGURE A.2: Vertical deformation of the chain under a force $k\varphi$.

of the constraints reactions and of the external force do not coincide and give origin to a couple M. It can be determined writing the momentum balance with pole in x_0:

$$\frac{M}{ku_0} = \sum_{n=1}^{+\infty} n\frac{u_n}{u_0} = \sum_{n=1}^{+\infty} n\left(-c_{2n-1}\varphi + c_{2n}\right) \tag{A.10}$$

by applying Eq.(A.9). The relation between the golden ratio and the terms of the Fibonacci sequence

$$c_n = \frac{\varphi^n - (-\varphi)^{-n}}{2\varphi - 1} \tag{A.11}$$

allows to transform the momentum balance into

$$\frac{M}{ku_0} = \varphi \sum_{n=1}^{+\infty} n\varphi^{-2n} = \varphi, \tag{A.12}$$

since it is easy to proof that the infinite sum above converges to one. Now a question arises: how can one apply a momentum to the structure in exam if the nodes do not bear it? The answer is straightforward: an horizontal force $T = \varphi k u_0$ can tense the chain if applied at the ku_0 elongated node x_0 together with $F = \varphi k u_0$. This way, horizontal displacements w_n appear and, since the horizontal balance can be written exactly in the same way as Eqs.(A.1)–(A.2), the result will be identical to Eq.(A.9):

$$\frac{w_n}{w_0} = -c_{2n-1}\varphi + c_{2n}. \tag{A.13}$$

Summarizing: in the only possible equilibria for the analyzed semi-infinite chain pulled by its end, the applied force and the nodal displacements are all oriented at 45 to the up-left. The modulus of the applied force and of the first node displacement are proportional according to φk, while the other displacements moduli are proportionals to the first one according to the recurrence relation $-c_{2n-1}\varphi + c_{2n}$ described by Fibonacci numbers c_n. Of course, a different way one can use the same derivation is considering symmetries. If the vertical force is applied along an axis of horizontal symmetry of and infinite chain, the rotational unbalance disappears since the ground reactions ku_n will be the same on the left- and on the right-hand sides of the force at same distances $|x_n|$.

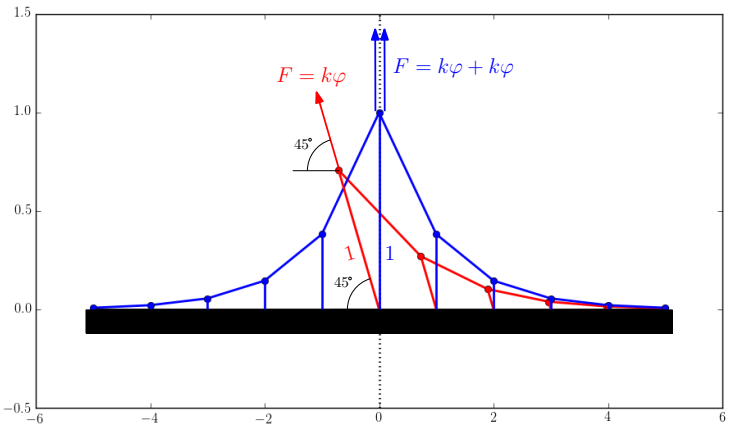

FIGURE A.3: The same force $k\varphi$ pulls two semi-infinite chains of equal bonds stiffness k: one is alone (red) and the other belongs to ans infinite chain with horizontal symmetry under the force (blue). Five nodes per side are shown at equilibrium.

Appendix B

Influence of fracture criteria on dynamic fracture propagation

The extent to which time-dependent fracture criteria affect the dynamic behavior of fracture in a discrete structure is discussed in this Appendix. The simplest case of a semi-infinite isotropic chain of oscillators has been studied. Two history-dependent criteria are compared to the classical one of threshold elongation for linear bonds. The results show that steady-state regimes can be reached in the low subsonic crack speed range where it is impossible according to the classical criterion. Repercussions in terms of load and crack opening versus velocity are explained in detail. A strong qualitative influence of history-dependent criteria is observed at

low subsonic crack velocities, especially in relation to achievable steady-state propagation regimes.

Before addressing the problem of the propagation, the behavior of a single link is discussed hereafter. A linear elastic spring can be quasi-statically elongated to failure and its final elongation value, u_s, supposed to be known constant. The simplest and most common failure criterion neglects dynamic effects on the spring resistance. It identifies the displacement u as critical when

$$\min t : \quad u(t) = u_s, \tag{B.1}$$

by which the time $t = t_f$ when the fracture occurs can be found.

A fracture event, though, in many materials turns out to be not simply determined by an instantaneous threshold value for some energy measure like the maximum elongation established above. We deal in the present work with non-instantaneous fracture criteria which nevertheless do not change the material stiffness. The rate with which a body is deformed or an integral measure of the deformation energy provided to a bond before it breaks are examined: the incubation time (IT) and the Tuler-Butcher (TB) criteria.

According to the first of those formulations, the average stress, or equivalently the average linear elastic stretch, over a period of time preceding the breakage is considered as the cause of fracture. Such a period is actually called the incubation time τ. The criterion, originally formulated in terms of stresses in Petrov and Utkin [125], can be written for the elastic

bond in object in terms of the elongation as

$$\min t: \quad \frac{1}{\tau}\int_{t-\tau}^{t} u(\theta)\,\mathrm{d}\theta = u_s. \tag{B.2}$$

Notice that u_s is still the threshold elongation of the spring when measured statically.

On the other hand, it has been observed that cumulative damage can also be the cause of fracture. A way to quantify it is via the Tuler-Butcher criterion discussed in Tuler and Butcher [129]. Again, one linear elastic bond is statically tested until it breaks at $u = u_s$. In a TB material, u_s represents the elongation to be exceeded in dynamics as

$$\min t: \quad \int_{0}^{t} \mathrm{H}(u(\theta) - u_s)\left(\frac{u(\theta)}{u_s} - 1\right)^2 \mathrm{d}\theta = D \tag{B.3}$$

before the fracture occurs at $t = t_f$. Here, $\mathrm{H}(u - u_s)$ is the Heaviside step function by which it is possible to write that only the work of the overstretch $u - u_s$ contributes to damage. Note that also this criterion was originally formulated in terms of stresses and that the exponent two was left general in the original formulation, but turns out to be such in most experiments. In this way the physical meaning of the criterion is that a maximum work has to be done by an external overload on the spring before it collapses. Looking at Eq.(B.3), it turns out that, as for the IT criterion, TB materials can be regarded as one possible extension of ideal brittleness. The latter can be retrieved indeed by setting the cumulated energetic damage D to zero. The criterion has found fruitful applications in analyzing spallation, impact loading, thermal shock caused fracture in

rocks, glass, aluminum, copper (see Boustie and Cottet [130], Wei et al. [131], Grady [132]).

In order to illustrate the peculiarities of the criteria, one can imagine applying a ramp displacement of rate r at $t = 0$ to three links with the same static strength u_s but different failure behavior. The ideally brittle one would break at $t_f = u_s/r$ as soon as its elongation reaches u_s. The IT spring would break, accordingly to Eq.(B.2), at $t_f = u_s/r + \tau/2$ if $r < 2u_s/\tau$ or at $t_f = \sqrt{2u_s\tau/r}$ otherwise, thus establishing a distinction between low and high deformation rates. The criterion shows a delayed failure causing an ultimate elongation bigger than the static one in this loading condition. In the case of a non-monotonic load, though, such delay might result in an elongation at failure which is smaller than the static one or during unloading (see Volkov et al. [126]). The TB criterion also predicts a delayed failure, but at $t_f = u_s/r + u_s\sqrt[3]{3D^2/r^2}$ according to (B.3). The difference with the IT case is that, now, an oscillating load which is strong enough to break the spring in statics will also do it in dynamics. Notice in fact that a constantly increasing cumulated damage would sooner or later surpass D (see left-hand side in Eq.(B.3)).

The rest of the Appendix is devoted to the model of a fracture in a structured medium subjected to the aforementioned criteria and their effects on the stable regimes of propagation. The results are expressed in terms of trapped lattice energy, applied remote force and crack tip opening.

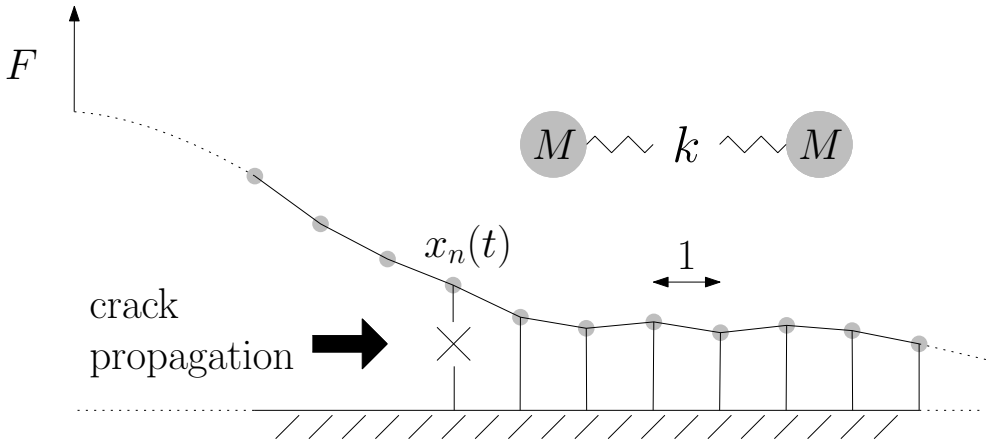

FIGURE B.1: Crack propagation in an infinite discrete chain. An infinite number of masses M separated by a unitary distance are linked to each other and to a rigid substrate via linear elastic springs of stiffness k. A force F applied at a remote distance breaks the links and the crack propagates to the right.

B.1 Background

Consider an infinite number of masses M linked to each other and to a rigid substrate via linear elastic springs of length 1 and stiffness k. A force F, applied at infinite distance, introduces energy into the system and finally breaks the links causing the crack to propagate to the right in Fig. B.1. If $x_n(t)$ is the link that fails at the time t, the equilibrium for a generic oscillator at $x = x_i$ in terms of its displacement $u_i(t)$ holds as

$$\frac{M}{k}\frac{\mathrm{d}^2 u_i}{\mathrm{d}t^2} = u_{i+1} + u_{i-1} - (2 + H(i-n))\, u_i, \tag{B.4}$$

where the Heaviside step function $H(i-n)$ allows for the combination of the equation for the detached ($i < n$) and intact part ($i \geq n$) of the

chain.

Only fracture with a constant speed v, i.e. steady-state fracture, is analyzed here. In such a way the problem is reduced to the long known settings of Slepyan and Troyankina [206], Slepyan [207]. The fracture can travel slower than sound in the broken structure, that is

$$v < v_c, \qquad v_c = \sqrt{\frac{k}{M}}. \tag{B.5}$$

As a result of the steady-state assumption we search for a solution in terms of the unknown function

$$u(x_i - vt) = u_i(t), \tag{B.6}$$

for any i and $t > 0$.

Further on we adopt a coordinate system which moves together with the crack tip

$$\eta = x - x_n(t) = x - vt, \tag{B.7}$$

in a way that the crack tip sits conveniently always at $\eta = 0$. By using such new moving frame, the coordinate η accounts for time and position simultaneously. Thus, the equation of motion Eq.(B.4) for $u(\eta)$ can be written in the broken ($\eta < 0$) and intact ($\eta \geq 0$) sides of the tip as:

$$\frac{\mathrm{d}^2 u(\eta)}{\mathrm{d}\eta^2} = \frac{u(\eta+1) + u(\eta-1) - (2 + H(\eta))\, u(\eta)}{v^2/v_c^2}. \tag{B.8}$$

With the help of the mathematical tools of Fourier transform and Wiener-Hopf technique, such an equation has been repeatedly solved for this and more complex structures, for example in Marder and Gross [121], Slepyan et al. [208], Kresse and Truskinovsky [209], Nieves et al. [210], Gorbushin and Mishuris [211], such to give the displacement profile $u(\eta)$ which travels along the structure at a given steady-state crack speed v. If one intends to describe the trajectory of a single mass during time, one has to just apply Eq.(B.6).

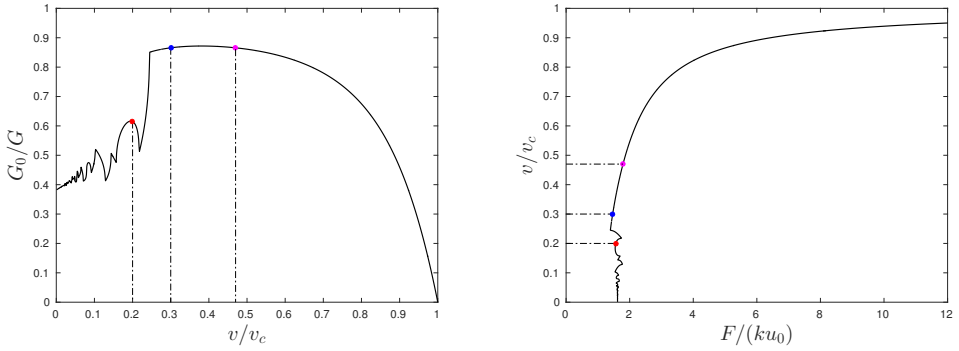

(A) Energy release rate. (B) Force versus crack speed.

FIGURE B.2: Existence of steady state solutions for the fracture propagation problem in a discrete chain as in Slepyan and Troyankina [206]. The dimensionless energy release rate and remotely applied force are plotted as functions of the normalized crack speed. For the displacement profiles of the points highlighted on the curves see Fig.B.3.

The concept of energetic lattice trapping of a structured material was originally introduced in Thomson et al. [212] and it can be quantified by the ratio G/G_0 not smaller than unity. Such energy may be introduced into the system in different ways. Analytical relations for the energy release rate G for every crack velocity have been retrieved in Slepyan and

Troyankina [206]. The quantity

$$G_0 = \frac{ku_0^2}{2} \tag{B.9}$$

is the link strain energy which is released locally at the crack tip at the moment of fracture, where $u_0 = u(0)$. For the examined chain, G_0/G has been plotted in Fig. B.2a. In our work we assume that the energy derives from a constant force F far away and the consequent crack speed has been recently derived in Gorbushin and Mishuris [213] as

$$\frac{F}{ku_0} = \sqrt{2\frac{G}{G_0}\frac{v_c + v}{v_c - v}} := \Phi(v) \tag{B.10}$$

and plotted in Fig. B.2b. Note that the same curve also implies that the limiting velocity v_c can not be reached via a finite force besides requiring an infinite energy release rate (as from Fig. B.2a).

The assumption that the crack propagates at a constant speed also requires some additional consideration. In particular it means, for a given oscillator i sitting at x_i, that it is not allowed to break before all the links situated at $x < x_i$ do (links on the left-hand side of Fig.B.1). From the propagation point of view, it must be clarified that a regime which involves nucleation of daughter cracks ahead of the mother crack tip ($\eta > 0$) is non-admissible. The detachment of the chain has to progress continuously. We shall discuss in the next sections how drastically the failure criteria change the admissible scenarios of stable detachment velocity.

B.1.1 Ideally brittle links

If the links are ideally brittle, the critical condition to be reached at the crack tip at the instant of fracture before further propagation

$$u_0 = u_s \tag{B.11}$$

is independent of the fracture propagation speed. With such a condition, that is when u_0 and u_s are interchangeable, the diagrams of force and energy release rate in Figs. B.2 are directly applicable. Furthermore, in this case, the condition of admissibility is easily checked i.e. that no points for $\eta > 0$ are lifted higher than the crack tip. Looking at Fig. B.3, one can notice that for such materials, configurations occurring at low v are unphysical since there are points ahead of the crack tip where the failure criterion has been encountered already before the arrival of the fracture front itself and thus must be labelled as not admissible. Discussions on the matter have been dealt in Marder and Gross [121], Gorbushin and Mishuris [211, 213]. For example, the speed $0.2v_c$ does not fulfill such requirement, then this must be discarded as non-admissible. On the contrary, the speeds $0.3v_c$ and $0.47v_c$ are admissible. Observing all the $u(\eta)$ profiles, for the isotropic chain the minimum velocity of the crack corresponds to about $0.27v_c$ and all larger subsonic velocities are admissible (see Fig. B.4). It is perhaps worth pointing out that such limit is smaller than the minimum energy release rate, which sits at about $0.38v_c$. This implies that a single G may correspond to two possible steady-states like $0.3v_c$ and $0.47v_c$. Such speeds, anyway, correspond to

two different loads (see Fig. B.2b). The highest of the two speeds is achieved uniquely by means of a larger force.

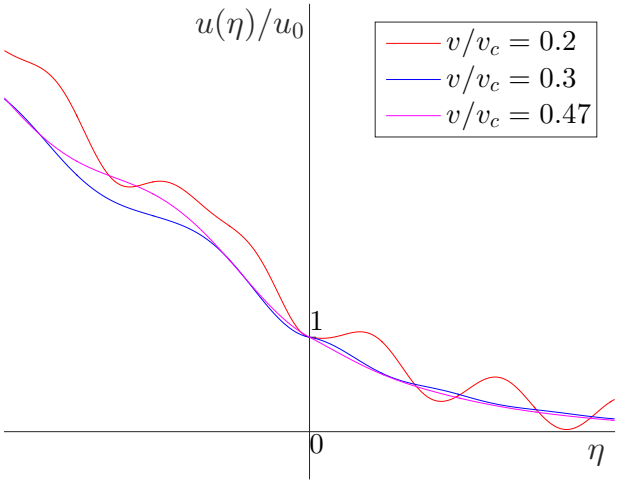

FIGURE B.3: Dimensionless steady-state displacements profiles. The crack speed $0.2v_c$ shows $u(\eta) > u_s$ in the intact region $\eta > 0$ ahead of the crack tip. It means that such velocity of the fracture wave is not admissible according to the instantaneous fracture criterion.

B.2 Problem and methods

When dealing with non-instantaneous criteria for fracture, the crack opening before fracture depends on the crack speed. In general,

$$u(0, v) = u_0(v) \tag{B.12}$$

must be determined accordingly to the new fracture parameters and does not simply equal u_s as for the ideal brittle criterion Eq.(B.11). In this way, also the energy released locally at the crack tip $G_0(v) = ku_0^2(v)/2$ is a function of the crack speed. Further on we express F as a multiple of the force required to break the spring in a static test via the function

$$\frac{F}{ku_s} = \Phi(v)\frac{u_s}{u_0(v)}, \tag{B.13}$$

which differs from the general Eq.(B.10) where the denominator incorporates the elongation at failure, independently on the particular fracture criterion adopted. The reason is conceptual and follows from the possibility of conducting experiments. For obtaining the same crack speed, the loading condition, indeed, must be accurately designed depending on how the failure happens (i.e. within the context of this Appendix, which fracture criterion better describes the constituent material). We stick to the ratio G/G_0, instead of introducing a hypothetical $G_s = ku_s^2/2$, because the energy release rate incorporates the type of the structure and its deformation properties (in the present case a linear elastic chain) and can hardly be measured. Moreover, in this way, as we will discuss further in the continuation, the dependency of G/G_0 remains untouched by the particular fracture criterion characterizing the links, while the force versus velocity relation depends on the particular criterion.

B.2.1 Incubation time criterion

The incubation time failure criterion Eq.(B.2) can be applied to the chain by a change of variable according to Eq.(B.7) which leads to

$$\Psi(v,\tau) := \frac{1}{v\tau}\int_0^{v\tau} \frac{u(\eta,v)}{u_0(v)}\,\mathrm{d}\eta = \frac{u_s}{u_0}. \tag{B.14}$$

The normalization by the displacement at the crack tip u_0 is convenient because, in the ideally brittle case, the crack opening u_0 before fracture was known in every case and given by the maximum elongation criterion, now it is unknown and dependent on velocity. The shape $u(\eta,v)/u_0(v)$ of the deformation profile, though, is given once and for all as it does not depend on the particular value of the crack opening. The advantage is that, once one calculates the shape at a certain velocity from the solution of Slepyan and Troyankina [206], this can be used for all the possible steady-state fracture criteria. If τ goes to zero, that is the material is ideally brittle, Eq.(B.14) returns $u_0 = u_s$ coherently. By this respect, one can say that IT materials are an extension of ideally brittle ones by means of τ. Moreover, for steady-state propagation, the length $v\tau$ is constant in time and thus incubation time can be considered as a non-local criterion as well as a non-instantaneous one.

B.2.2 Tuler-Butcher criterion

In order to deal with the usual moving coordinate frame Eq.(B.7) and a steady-state regime of velocity v, the TB criterion Eq.(B.3) can be

transformed into the equation

$$\int_0^{+\infty} \frac{\mathrm{H}(u(\eta,v)-u_s)}{vD} \frac{(u(\eta,v)-u_s)^2}{u_0(v)^2}\,\mathrm{d}\eta = \frac{u_s^2}{u_0^2}. \tag{B.15}$$

Taking advantage of the invariance of $u(\eta,v)/u_0(v)$ with respect to η, the function

$$\Lambda(v,D) = \frac{u_s}{u_0} \tag{B.16}$$

can be obtained as solution of Eq.(B.15).

B.3 Results

In order to have dimensionless strength parameters, from this section on we express u_s in units of the distance between the masses, whereas D and τ are expressed in units of the same distance divided by the sound velocity v_c.

B.3.1 Incubation time criterion

The steady-state analogue of the incubation time criterion in Eq.(B.14), which also defines the function $\Psi(v,\tau)$, solves the issue of calculating the crack opening, given τ and u_s

$$u_0 = \frac{u_s}{\Psi(v,\tau)}. \tag{B.17}$$

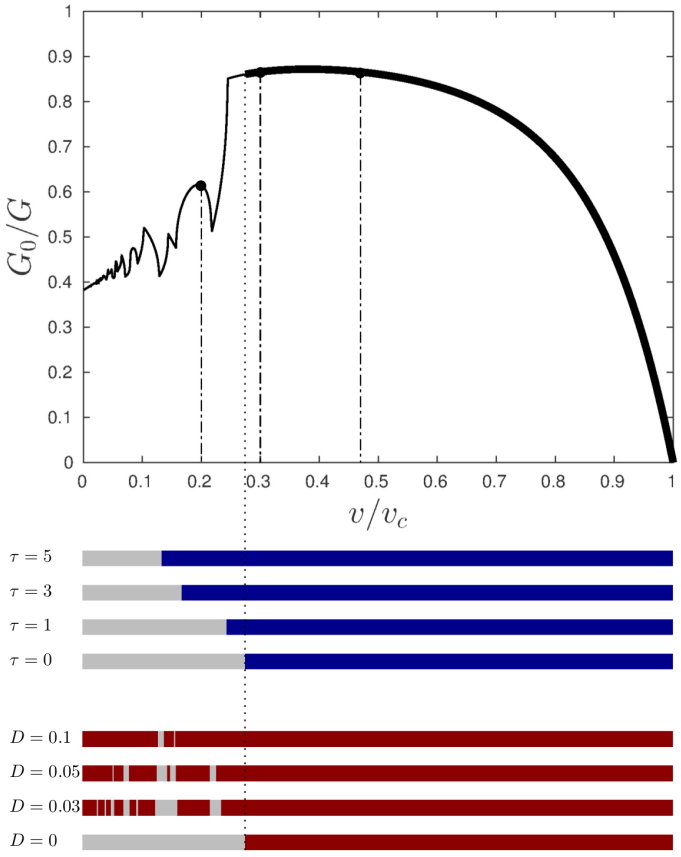

FIGURE B.4: Influence of fracture criteria on admissible regimes. The plot on the top shows the admissible regimes for ideally brittle links. Grey segments of the admissible bars indicate non-admissible crack speeds, blue bars refer to IT achievable steady-states, red bars to TB ones.

Speaking of the force to apply for achieving a certain steady-state velocity, substituting Eq.(B.17) into Eq.(B.13) gives

$$\frac{F}{ku_s} = \frac{\Phi(v)}{\Psi(v,\tau)}. \tag{B.18}$$

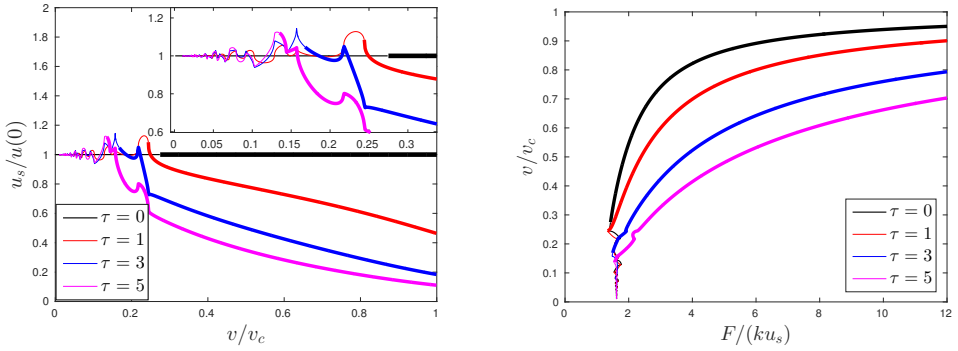

(A) Function $\Psi(v, \tau)$ versus velocity (see Eq.(B.14)).

(B) Force versus crack speed (see Eq.(B.18)).

FIGURE B.5: Effects of incubation time τ on crack opening and applied force compared with the ideally brittle case. Thick lines stand for admissible regimes. a) The function $\Psi(v, \tau) = u_s/u(0) = u_s/u_0$ measures how much the crack opening differs from the case of an ideally brittle chain. b) The crack speed dependent opening $u(0) = u(0, v)$ expressed through $\Psi(v, \tau)$ changes the prediction of the force to apply in order to cause a certain velocity.

The behavior of the function $\Psi(v, \tau)$ influences the way τ modifies the crack opening with respect to the ideally brittle one ($\tau \to 0$) and this is shown in Fig.B.5a. A linear elastic bond which exhibits a non-zero incubation time will in general allow a bigger crack opening at the instant of fracture. Crack openings smaller than u_s, though, are admissible at low velocities due to rapid oscillations and negative $\partial u/\partial t$ close to the tip (see Fig.B.6). The influence of τ on the force is plotted in Fig.B.5b. Given the result of the static test on the spring u_s, if the goal is achieving a certain velocity v, an IT type material predicts that the steady-state regime would be reached in general via a bigger force than one could expect if τ is neglected. The region where the relation between force and velocity

is not bijective is stretched to the right and the difference in velocities for the same force decreases steadily while raising the incubation time. Note that τ does not play any role in the limiting case of zero velocity of propagation, where the force produces the same results as for the ideally brittle spring (see Eq.(B.14) for $v \to 0$). In order to verify the analytical

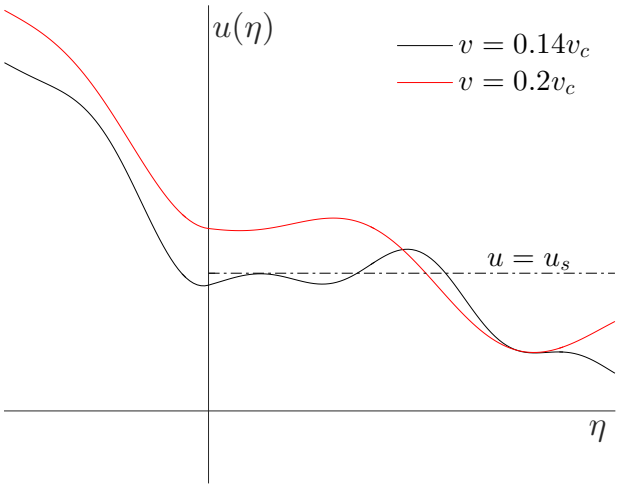

FIGURE B.6: Crack opening for small velocities and high incubation times. With $\tau = 5$, the crack tip opening u_0 for the admissible speed $v = 0.14v_c$ is predicted to be smaller than the static strength u_s. For comparison, $v = 0.2v_c$ shows the most common situation of $u_0 > u_s$. See also Fig. B.5a.

solution, we searched for the steady-state regimes via solving Eq.(B.8) by a finite difference scheme similarly as in Gorbushin and Mishuris [213] where the same numerical procedure is extensively explained. A chain of 2000 masses was loaded with a distant vertical constant force. The instant of fracture for a link was identified according to the condition

Eq.(B.2). After iterating, the next failures tended to occur at constant time pace and such an interval was used for calculating the stable crack speed for a given force. The analytical solution is perfectly matched and the numerical approach confirms that a steady-state propagation is not achievable at low velocities (results not shown).

This kind of computation is quite heavy because of the algorithm adopted to identify the time of fracture at every location x_i. Before a steady fracture propagation is reached, indeed, during the transient regime, the history $u_i(t)$ in the last interval τ must be recorded and the integral Eq.(B.3) updated for every x_i. This marks a principal difference with the instantaneous traditional criterion in which case the quick check $u \leq u_s$ is sufficient. We have tried to simplify the procedure via making the criterion pseudo-instantaneous. Theoretically, Eq.(B.17) should be valid only for steady-state fracture. Nevertheless, if one estimates the instantaneous crack velocity $\tilde{v}(t)$ from the last two failures, the criterion can be artificially reduced to $u \leq u_0(\tilde{v}, \tau)$ instead of calculating the integral Eq.(B.17) at all. Such an attempt has been proven to be effective beyond expectations for the particular studied problem in achieving the same steady-states as in theory and the rigorous numerical simulation for same applied load.

Another crucial effect of $\tau > 0$ on the crack propagation is that it monotonically enlarges the regions of achievable steady-states as illustrated in Fig. B.4. For instance, the speed $0.2v_c$, that is non-admissible for an ideally brittle material with critical elongation parameter u_s, can be reached with $\tau = 3$ and bigger.

B.3.2 Tuler-Butcher criterion

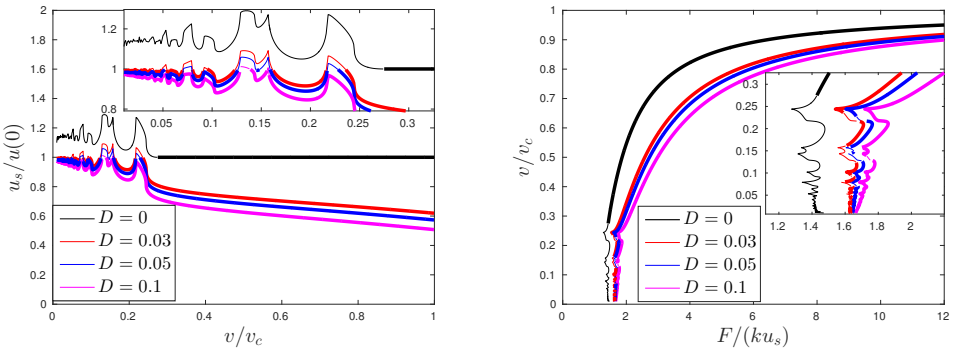

(A) Function $\Lambda(v, D)$ versus crack speed (see Eq.(B.15)).

(B) Force versus crack speed (see Eq.(B.20)).

FIGURE B.7: Effects of overload maximum work D on crack opening and applied force compared with the ideally brittle case. Thin lines represent unphysical steady-states. a) The function $u_s/\Lambda(v, D)$ measures how much the crack opening differs from an ideally brittle chain. b) The crack speed dependent opening u_0 expressed through $\Lambda(v, D)$ changes the prediction of the force to apply in order to cause a certain velocity.

By means of Eq.(B.16), one can retrieve the crack opening

$$u_0 = \frac{u_s}{\Lambda(v, D)} \tag{B.19}$$

associated to all the combinations of crack speed and D. As consequence, keeping the force proportional to the material property u_s instead of the velocity dependent crack opening, Eq.(B.13) becomes

$$\frac{F}{ku_s} = \frac{\Phi(v)}{\Lambda(v, D)}. \tag{B.20}$$

The plots in Fig.B.7 allow us to visualize how the dynamic strength parameter D affects the chain behavior. As observed for IT materials, the immediate impact of TB damage accumulation results in an augmented crack opening at equal crack speed as an ideally brittle material showing the same static strength u_s, at least in the range of medium or high v/v_c (see Fig.B.7a). The force needed for obtaining a desired velocity is depicted in Fig.B.7b. It is evident that the capability of the material to bear a certain work of the overstretch before failure, i.e. bigger D, makes the chain detachment increasingly slower for same F/ku_s. A structure of TB bonds can be predicted to be dynamically tougher than its ideally brittle counterpart. For $D \to 0$ and low fracture speed the complex structure does not respond like an ideally brittle one. Looking at Fig.B.8, indeed, one can notice that for low v, i.e. in the range where $u(\eta)$ does not decrease monotonically ahead of the crack tip, the criterion in the form Eq.(B.15) may return $u_0 < u_s$. Such a feat differs from all the cases analyzed in this work: single bonds as well as the ideally brittle and IT crack tips always fail for $u \geq u_s$. However, in the cases where the latter inequality is violated in a TB link, we obtain non-admissible steady-state propagation regimes. A point can be made, therefore, that a theoretical limit for the crack opening is for a TB material to satisfy $u_0 \geq u_s$.

Like for incubation time materials, as it can be seen in Fig. B.4, new zones of admissibility appear in the low velocity region for larger D. Nevertheless, there is a significant qualitative difference with the incubation time situation: such admissible intervals emerge small and scattered, but then, with increasing D, expand gradually and merge until every subsonic crack speed can be obtained for D close to unity.

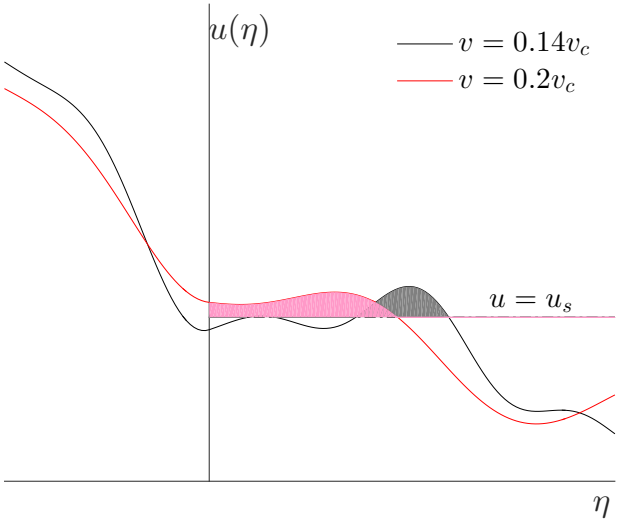

FIGURE B.8: Crack opening at low velocities for small D. The profile $u(\eta)$ for two fracture speeds at $D = 0.03$ is shown. The shaded faces represent the areas where the integral Eq.(B.15) must be computed. The result for $v = 0.14v_c$ shows how $u_0 < u_s$ means that the chain detaches ahead of $\eta = 0$ making that crack speed non-admissible. See also Fig.B.7a.

B.4 Remarks

The dynamic fracture propagation in discrete structures has been investigated in a considerable amount of possible scenarios (see references above) but the influence of failure criteria different from a threshold stress has not gained the attention that it deserves despite the fact that non-instantaneous criteria have already been shown to be reliable in continuum mechanics (e.g. as recently discussed in Alves and Lobo [214]). As

a first step to fill this gap, two time-dependent criteria have been analyzed in detail when applied to the dynamic fracture propagation of a chain of oscillators and they have been compared to the classical ideal brittle fracture. In both cases, enhanced admissibility have appeared at low crack speeds and mapped in Fig. B.4. An increasing incubation time τ enlarges the admissibility continuously but never covers all the subsonic crack speeds. More than that, a TB material which requires a larger work of the overstretch for fracture and characterized by a bigger D also creates completely new zones of achievable steady-states and it is predicted that all the subsonic range is possible if $D \gtrsim 0.13$.

Speaking of the steady-state crack opening, the time-dependent criteria cause a delay in fracture after reaching the static strength of the bonds. This means that in most cases one should expect $u_0 > u_s$ like it would happen when monotonically elongating a single spring. At low v, though, this is not the behavior caused by a constant force applied on a complex structure. Ample and rapid oscillations ahead of the crack tip cause the delayed fracture to happen at $u_0 < u_s$. While such propagation regimes are admissible at high τ for incubation materials, the same is not true for TB ones (see Figs.B.6-B.8). The mathematical form of the latter failure criterion indeed excludes such steady-states on the grounds that daughter cracks would jeopardize the steady-state assumption. In short, a theoretical limit has been found which states that for a TB chain a dynamic fracture can propagate at constant speed only if $u_0 \geq u_s$.

As intuition suggests, the two examined non-instantaneous criteria make the structure tougher than the corresponding ideal brittle one with the

same static strength u_s. Thus, for obtaining a certain velocity v one needs a bigger force if τ or D increase. In this way, the curves in Figs.B.5b-B.7b result also in an important practical application. With a few experiments on materials whose u_s has been independently measured, the couples F-v allow for the material characterization in terms of the second fracture parameter τ or D at least if stable crack speeds are retrieved in the monotonic interval of the curves (medium and high v/v_c).

The velocity dependent energy release rate ratio G/G_0 is a solution which is irrespective of the particular fracture criterion adopted. It is also valid regardless of the way the energy is introduced into the system. In the present work we use a constant force as the external load. However, in case one prefers to implement different kind of loading, like for instance in Marder and Gross [121] when dealing with lattices, or for example to facilitate a specific experimental procedure, the relation between the new load and the crack speed has to be evaluated, while the energy - crack speed diagram remains the same.

Two numerical integration schemes have been used to solve the set of governing equations in the IT scenario and compared with the analytical solution derived in the present work. The first of these verified the criterion condition in its integral form Eq.(B.2) at every time step for all the unbroken bonds. Such an approach enables one to simulate also the transient regimes before a steady-state is reached. The steady-states were achieved only in the admissible regions of Fig.B.4 and there the force-velocity relations agreed perfectly with the ones in Fig.B.5b. The second test was performed by adopting a pseudo-static failure criterion:

a dynamic threshold elongation $u_0(\tilde{v}, \tau)$ was established based on the instantaneous crack velocity $\tilde{v}$ and Eq.(B.17). This simplified algorithm performed much faster than the first one, and still returned correct results. For this specific structure at least then, it seems that many of the conclusions drawn here can still be valid in the transient regimes.

Beyond the particular scope of this study, various propagation regimes, in absence of crack arrest, can appear: steady-state, other regular ones (clustering or forerunning as discussed in Nieves et al. [210], Mishuris et al. [215, 216], Slepyan et al. [217, 218], Nieves et al. [219]) or chaotic regimes. The realization of one or another heavily depends on the loading type, its intensity and on the structure itself. However, when the problem is faced from a mathematical point of view, assumptions of steady-state regimes have always been made in order to obtain simple solutions. With the analytical results in one hand, an a posteriori examination is required which identifies where the solution fulfills the assumptions and constraints: only that part of the solution is labeled as *admissible*. Generally speaking, though, it does not mean that all those regimes will emerge in practice as steady-state. In most of the cases it happens; nevertheless, as it has been shown in numerical simulations, other ordered regimes of propagation may arise such as clustering. In such circumstances, the steady-state velocity predicted theoretically reveals as the average speed at which the cluster moves (see Nieves et al. [210], Mishuris et al. [216], Nieves et al. [219] on the matter).

We have not treated the problem of branching in the present settings of history-dependent criteria. It has turned out already in Marder and

Gross [121], Gorbushin and Mishuris [213, 220] that such instabilities can become relevant at high crack speeds. In the considered geometry, loading condition and material parameters, the branching mostly happens along the crack surfaces but not on the crack line ahead. That is evident from the solution profile $u(\eta)$ for $v/v_c = 0.2$ in Fig.B.3. If the horizontal springs show the same dynamic resistance as the vertical ones, their fracture can precede the chain detachment from the substrate, making a steady-state propagation impossible and sensibly reducing the limiting speed with respect to v_c. The admissibility check would imply that, for none of the consecutive oscillators, the difference $u_{i+1} - u_i$) does reach the condition imposed by the fracture criterion. More complex scenarios may occur with structures characterized by flexural stiffness, heterogeneities or localized feeding waves (see e.g. Nieves et al. [210], Mishuris et al. [216], Nieves et al. [219]). Furthermore, a steady-state regime can be unattainable, resulting in unstable or alternating velocities, when the structure is not loaded far from the crack tip, but via accumulated energy in the form of residual stresses of the bonds (Ayzenberg-Stepanenko et al. [221]). Complications have also been object of investigation in the framework of bridged cracks by Mishuris et al. [215].

In conclusion, the fracture criteria considered here sensibly affect the dynamic propagation of cracks in discrete structures. The effects are particularly important both in terms of force vs velocity relations and in new regimes of admissibility at low crack speeds. Succinctly, by the present results, we are able to underline two main messages:

- it is at low speed regimes that an experimental investigation should

be carried out more carefully for understanding whether it is necessary to incorporate history-dependent fracture criteria in the dynamic fracture model;

- the energy release rate ratio and shapes of the displacement profiles as functions of the velocity are invariants, in linear theory, and can promptly be used and adapted to the most suitable fracture criterion for the analyzed problem.

The possible outlook of this research is the application of the approach to a) more complex lattice structures (inhomogeneous, triangle ones) as in Mishuris et al. [222], Nieves et al. [223]; b) highly ordered bi-dimensional lattices, for instance to crack propagation in graphene layers (see Tsai et al. [119], Xiao et al. [224]) or c) to the unbinding of long protein chains whose analysis has been made feasible by the improvements in the field of atomic force microscopy and for which the bonds strength has already shown to be eminently dependent on the strain rate (Merkel et al. [225], Hinterdorfer and Dufrêne [226]). As the discretization, the considered here model can be useful for modeling of the peel test of flexible films (see e.g. Wei and Hutchinson [227], Nase et al. [228]).

Bibliography

[1] Gerard A Ateshian, Corinne R Henak, and Jeffrey A Weiss. Toward patient-specific articular contact mechanics. *Journal of biomechanics*, 48(5):779–786, 2015.

[2] Scott J Hollister. Porous scaffold design for tissue engineering. *Nature materials*, 4(7):518–524, 2005.

[3] W Michael Lai, JS Hou, and Van C Mow. A triphasic theory for the swelling and deformation behaviors of articular cartilage. *Journal of biomechanical engineering*, 113(3):245–258, 1991.

[4] Benjamin Loret and Fernando MF Simões. Articular cartilage with intra- and extrafibrillar waters–mass transfer and generalized diffusion. *European Journal of Mechanics-A/Solids*, 26(5):759–788, 2007.

[5] Frederick H Silver, Gino Bradica, and Alfred Tria. Do changes in the mechanical properties of articular cartilage promote catabolic destruction of cartilage and osteoarthritis? *Matrix Biology*, 23(7):467–476, 2004.

[6] Martin Lotz and Richard F Loeser. Effects of aging on articular cartilage homeostasis. *Bone*, 51(2):241–248, 2012.

[7] Joseph A Buckwalter, Henry J Mankin, Alan J Grodzinsky, et al. Articular cartilage and osteoarthritis. *Instructional Course Lectures-American Academy of Orthopaedic Surgeons*, 54:465, 2005.

[8] Nigel Arden and Michael C Nevitt. Osteoarthritis: epidemiology. *Best practice & research Clinical rheumatology*, 20(1):3–25, 2006.

[9] A Shane Anderson and Richard F Loeser. Why is osteoarthritis an age-related disease? *Best practice & research Clinical rheumatology*, 24(1): 15–26, 2010.

[10] Johannes WJ Bijlsma, Francis Berenbaum, and Floris PJG Lafeber. Osteoarthritis: an update with relevance for clinical practice. *The Lancet*, 377(9783):2115–2126, 2011.

[11] W Herzog, S Diet, E Suter, P Mayzus, TR Leonard, C Müller, JZ Wu, and M Epstein. Material and functional properties of articular cartilage and patellofemoral contact mechanics in an experimental model of osteoarthritis. *Journal of Biomechanics*, 31(12):1137–1145, 1998.

[12] JTA Mäkelä, SK Han, W Herzog, and RK Korhonen. Very early osteoarthritis changes sensitively fluid flow properties of articular cartilage. *Journal of biomechanics*, 48(12):3369–3376, 2015.

[13] LP Li, J Soulhat, MD Buschmann, and A Shirazi-Adl. Nonlinear analysis of cartilage in unconfined ramp compression using a fibril reinforced poroelastic model. *Clinical Biomechanics*, 14(9):673–682, 1999.

[14] Rami K Korhonen, Mikko S Laasanen, Juha Töyräs, Reijo Lappalainen, Heikki J Helminen, and Jukka S Jurvelin. Fibril reinforced poroelastic model predicts specifically mechanical behavior of normal, proteoglycan depleted and collagen degraded articular cartilage. *Journal of biomechanics*, 36(9):1373–1379, 2003.

[15] W Wilson, CC Van Donkelaar, B Van Rietbergen, and R Huiskes. A fibril-reinforced poroviscoelastic swelling model for articular cartilage. *Journal of biomechanics*, 38(6):1195–1204, 2005.

[16] W Wilson, CC Van Donkelaar, R Van Rietbergen, and R Huiskes. The role of computational models in the search for the mechanical behavior and damage mechanisms of articular cartilage. *Medical engineering & physics*, 27(10):810–826, 2005.

[17] RA Day and DM Potts. Zero thickness interface elementsnumerical stability and application. *International Journal for numerical and analytical methods in geomechanics*, 18(10):689–708, 1994.

[18] Y Capdeville and J-J Marigo. Shallow layer correction for spectral element like methods. *Geophysical Journal International*, 172(3):1135–1150, 2008.

[19] Reinaldo Rodríguez-Ramos, Federico J Sabina, Raúl Guinovart-Díaz, and Julián Bravo-Castillero. Closed-form expressions for the effective coefficients of a fiber-reinforced composite with transversely isotropic constituents-i. elastic and square symmetry. *Mechanics of Materials*, 33 (4):223–235, 2001.

[20] Julián Bravo-Castillero, Raúl Guinovart-Dıaz, Federico J Sabina, and Reinaldo Rodrıguez-Ramos. Closed-form expressions for the effective coefficients of a fiber-reinforced composite with transversely isotropic constituents–ii. piezoelectric and square symmetry. *Mechanics of Materials*, 33(4):237–248, 2001.

[21] Raúl Guinovart-Dıaz, Julián Bravo-Castillero, Reinaldo Rodrıguez-Ramos, and Federico J Sabina. Closed-form expressions for the effective

coefficients of fibre-reinforced composite with transversely isotropic constituents. i: Elastic and hexagonal symmetry. *Journal of the Mechanics and Physics of Solids*, 49(7):1445–1462, 2001.

[22] Raúl Guinovart-Díaz, Reinaldo Rodríguez-Ramos, Julián Bravo-Castillero, Federico J Sabina, José A Otero-Hernández, and Gerard A Maugin. A recursive asymptotic homogenization scheme for multi-phase fibrous elastic composites. *Mechanics of materials*, 37(11):1119–1131, 2005.

[23] Federico J Sabina, Reinaldo Rodrıguez-Ramos, Julián Bravo-Castillero, and Raúl Guinovart-Dıaz. Closed-form expressions for the effective coefficients of a fibre-reinforced composite with transversely isotropic constituents. ii: Piezoelectric and hexagonal symmetry. *Journal of the Mechanics and Physics of Solids*, 49(7):1463–1479, 2001.

[24] H Berger, S Kari, U Gabbert, R Rodriguez-Ramos, J Bravo-Castillero, R Guinovart-Diaz, FJ Sabina, and GA Maugin. Unit cell models of piezoelectric fiber composites for numerical and analytical calculation of effective properties. *Smart Materials and Structures*, 15(2):451, 2006.

[25] R Guinovart-Díaz, R Rodriguez-Ramos, J Bravo-Castillero, FJ Sabina, and GA Maugin. Closed-form thermoelastic moduli of a periodic three-phase fiber-reinforced composite. *Journal of Thermal Stresses*, 28(10): 1067–1093, 2005.

[26] Julián Bravo-Castillero, Reinaldo Rodríguez-Ramos, Houari Mechkour, José A Otero, and Federico J Sabina. Homogenization of magneto-electro-elastic multilaminated materials. *The Quarterly Journal of Mechanics and Applied Mathematics*, 61(3):311–332, 2008.

[27] Héctor Camacho-Montes, FJ Sabina, Julián Bravo-Castillero, Raúl Guinovart-Díaz, and Reinaldo Rodríguez-Ramos. Magnetoelectric coupling and cross-property connections in a square array of a binary composite. *International Journal of Engineering Science*, 47(2):294–312, 2009.

[28] Peter Bövik. On the modelling of thin interface layers in elastic and acoustic scattering problems. *The Quarterly Journal of Mechanics and Applied Mathematics*, 47(1):17–42, 1994.

[29] AB Movchan and NV Movchan. *Mathematical modelling of solids with nonregular boundaries*, volume 3. CRC Press, 1995.

[30] Anders Klarbring and AB Movchan. Asymptotic modelling of adhesive joints. *Mechanics of Materials*, 28(1):137–145, 1998.

[31] G Mishuris. Imperfect transmission conditions for a thin weakly compressible interface. 2D problems. *Archives of Mechanics*, 56(2):103–115, 2004.

[32] Y Benveniste. A general interface model for a three-dimensional curved thin anisotropic interphase between two anisotropic media. *Journal of the Mechanics and Physics of Solids*, 54(4):708–734, 2006.

[33] Clara Sussmann, Dan Givoli, and Yakov Benveniste. Combined asymptotic finite-element modeling of thin layers for scalar elliptic problems. *Computer Methods in Applied Mechanics and Engineering*, 200(47): 3255–3269, 2011.

[34] Andreas Öchsner, Michal Stasiek, Gennady Mishuris, and José Grácio. A new evaluation procedure for the butt-joint test of adhesive technology: Determination of the complete set of linear elastic constants. *International Journal of Adhesion and Adhesives*, 27(8):703–711, 2007.

[35] Ivan I Argatov and Federico J Sabina. Small-scale indentation of an elastic coated half-space: influence of poissons ratios on the substrate effect. *International Journal of Engineering Science*, 81:33–40, 2014.

[36] M Dalla Riva and G Mishuris. Existence results for a nonlinear transmission problem. *Journal of Mathematical Analysis and Applications*, 430(2):718–741, 2015.

[37] Benjamin Cerfontaine, Anne-Catherine Dieudonné, Jean-Pol Radu, Frédéric Collin, and Robert Charlier. 3d zero-thickness coupled interface finite element: Formulation and application. *Computers and Geotechnics*, 69:124–140, 2015.

[38] JR Parsons and J Black. The viscoelastic shear behavior of normal rabbit articular cartilage. *Journal of Biomechanics*, 10(1):21–29, 1977.

[39] CG Armstrong. An analysis of the stresses in a thin layer of articular cartilage in a synovial joint. *Engineering in medicine*, 15(2):55–61, 1986.

[40] BR Simon, RS Coats, and SL-Y Woo. Relaxation and creep quasilinear viscoelastic models for normal articular cartilage. *Journal of Biomechanical Engineering*, 106:159–164, 1984.

[41] I Argatov, AU Daniels, G Mishuris, S Ronken, and D Wirz. Accounting for the thickness effect in dynamic spherical indentation of a viscoelastic layer: Application to non-destructive testing of articular cartilage. *European Journal of Mechanics-A/Solids*, 37:304–317, 2013.

[42] JJ Garcia, NJ Altiero, and RC Haut. An approach for the stress analysis of transversely isotropic biphasic cartilage under impact load. *Journal of Biomechanical Engineering*, 120:608–613, 2008.

[43] NS Selyutina, II Argatov, and GS Mishuris. On application of fung's quasi-linear viscoelastic model to modeling of impact experiment for articular cartilage. *Mechanics Research Communications*, 67:24–30, 2015.

[44] Luca Placidi, Francesco Dell'Isola, Nicoletta Ianiro, and Giulio Sciarra. Variational formulation of pre-stressed solid–fluid mixture theory, with an application to wave phenomena. *European Journal of Mechanics-A/Solids*, 27(4):582–606, 2008.

[45] Uwe-Jens Görke, Sonja Kaiser, Anke Bucher, and Reiner Kreißig. A consistent mixed finite element formulation for hydro-mechanical processes in saturated porous media at large strains based on a generalized material description. *European Journal of Mechanics-A/Solids*, 32:88–102, 2012.

[46] Gerard A Ateshian, Nadeen O Chahine, Ines M Basalo, and Clark T Hung. The correspondence between equilibrium biphasic and triphasic material properties in mixture models of articular cartilage. *Journal of biomechanics*, 37(3):391–400, 2004.

[47] Qingen Meng, Shuqiang An, Robin A Damion, Zhongmin Jin, Ruth Wilcox, John Fisher, and Alison Jones. The effect of collagen fibril orientation on the biphasic mechanics of articular cartilage. *Journal of the Mechanical Behavior of Biomedical Materials*, 65:439–453, 2017.

[48] Michael A Soltz and Gerard A Ateshian. A conewise linear elasticity mixture model for the analysis of tension-compression nonlinearity in

articular cartilage. *Journal of biomechanical engineering*, 122(6):576–586, 2000.

[49] Gerhard A Holzapfel and Ray W Ogden. On the tension–compression switch in soft fibrous solids. *European Journal of Mechanics-A/Solids*, 49:561–569, 2015.

[50] VC Mow, SC Kuei, WM Lai, and CG Armstrong. Biphasic creep and stress relaxation of articular cartilage in compression: theory and experiments. *Journal of biomechanical engineering*, 102(1):73–84, 1980.

[51] II Argatov. Mathematical modeling of linear viscoelastic impact: Application to drop impact testing of articular cartilage. *Tribology International*, 63:213–225, 2013.

[52] G A Ateshian, W M Lai, W B Zhu, and VC Mow. An asymptotic solution for the contact of two biphasic cartilage layers. *Journal of biomechanics*, 27(11):1347–1360, 1994.

[53] JZ Wu, W Herzog, and M Epstein. An improved solution for the contact of two biphasic cartilage layers. *Journal of biomechanics*, 30:371–375, 1997.

[54] II Argatov and GS Mishuris. Axisymmetric contact problem for a biphasic cartilage layer with allowance for tangential displacements on the contact surface. *European Journal of Mechanics-A/Solids*, 29(6):1051–1064, 2010.

[55] Ivan Argatov and Gennady Mishuris. Elliptical contact of thin biphasic cartilage layers: Exact solution for monotonic loading. *Journal of biomechanics*, 44(4):759–761, 2011.

[56] II Argatov and GS Mishuris. Contact problem for thin biphasic cartilage layers: perturbation solution. *The Quarterly Journal of Mechanics and Applied Mathematics*, 64(3):297–318, 2011.

[57] AF Quinonez, JL Summers, J Fisher, and ZM Jin. An analytical solution for the radial and tangential displacements on a thin hemispherical layer of articular cartilage. *Biomechanics and Modeling in Mechanobiology*, 10: 283–293, 2011.

[58] JR Barber. Contact problems for the thin elastic layer. *International Journal of Mechanical Sciences*, 32:129–132, 1990.

[59] AW Eberhardt, LM Keer, JL Lewis, and V Vithoontien. An analytical model of joint contact. *Journal of Biomechanical Engineering*, 112:407–413, 1990.

[60] A Pérez-González, C Fenollosa-Esteve, JL Sancho-Bru, FT Sánchez-Marín, M Vergara, and PJ Rodríguez-Cervantes. A modified elastic foundation contact model for application in 3d models of the prosthetic knee. *Medical Engineering & Physics*, 30:387–398, 2008.

[61] YC Lin, RT Haftka, NV Queipo, and BJ Fregly. Surrogate articular contact models for computationally efficient multibody dynamic simulations. *Medical Engineering & Physics*, 32:584–594, 2010.

[62] Ivan Argatov and Gennady Mishuris. Frictionless elliptical contact of thin viscoelastic layers bonded to rigid substrates. *Applied Mathematical Modelling*, 35(7):3201–3212, 2011.

[63] Ivan Argatov. Development of an asymptotic modeling methodology for tibio-femoral contact in multibody dynamic simulations of the human knee joint. *Multibody System Dynamics*, 28(1-2):3–20, 2012.

[64] M Rahman and G Newaz. Boussinesq type solution for a transversely isotropic half-space coated with a thin film. *International Journal of Engineering Science*, 38:807–822, 2000.

[65] Robert M Schinagl, Donnell Gurskis, Albert C Chen, and Robert L Sah. Depth-dependent confined compression modulus of full-thickness bovine articular cartilage. *Journal of Orthopaedic Research*, 15(4):499, 1997.

[66] Ramaswamy Krishnan, Seonghun Park, Felix Eckstein, and Gerard A Ateshian. Inhomogeneous cartilage properties enhance superficial interstitial fluid support and frictional properties, but do not provide a homogeneous state of stress. *Journal of biomechanical engineering*, 125 (5):569–577, 2003.

[67] Salvatore Federico, Alfio Grillo, Guido La Rosa, Gaetano Giaquinta, and Walter Herzog. A transversely isotropic, transversely homogeneous microstructural-statistical model of articular cartilage. *Journal of biomechanics*, 38(10):2008–2018, 2005.

[68] Salvatore Federico and Walter Herzog. On the anisotropy and inhomogeneity of permeability in articular cartilage. *Biomechanics and modeling in mechanobiology*, 7(5):367–378, 2008.

[69] Gerard A Ateshian, Vikram Rajan, Nadeen O Chahine, Clare E Canal, and Clark T Hung. Modeling the matrix of articular cartilage using a continuous fiber angular distribution predicts many observed phenomena. *Journal of biomechanical engineering*, 131(6):061003, 2009.

[70] Salman Chegini and Stephen J Ferguson. Time and depth dependent poissons ratio of cartilage explained by an inhomogeneous orthotropic

fiber embedded biphasic model. *Journal of biomechanics*, 43(9):1660–1666, 2010.

[71] Yuriy Tokovyy and Chien-Ching Ma. Analytical solutions to the axisymmetric elasticity and thermoelasticity problems for an arbitrarily inhomogeneous layer. *International Journal of Engineering Science*, 92: 1–17, 2015.

[72] Gennaro Vitucci, Ivan Argatov, and Gennady Mishuris. An asymptotic model for the deformation of a transversely isotropic, transversely homogeneous biphasic cartilage layer. *Mathematical Methods in the Applied Sciences*, 2016. doi: 10.1002/mma.3895. URL http://dx.doi.org/10.1002/mma.3895.

[73] Markus Heß. A simple method for solving adhesive and non-adhesive axisymmetric contact problems of elastically graded materials. *International Journal of Engineering Science*, 104:20–33, 2016.

[74] Markus Hess and Valentin L Popov. Method of dimensionality reduction in contact mechanics and friction: a user's handbook. ii. power-law graded materials. *Facta Universitatis, Series: Mechanical Engineering*, 14(3):251–268, 2016.

[75] Gennaro Vitucci and Gennady Mishuris. Three-dimensional contact of transversely isotropic transversely homogeneous cartilage layers: A closed-form solution. *European Journal of Mechanics-A/Solids*, 65:195–204, 2017.

[76] JR Ralphs and M Benjamin. The joint capsule: structure, composition, ageing and disease. *Journal of anatomy*, 184(Pt 3):503, 1994.

[77] MIV Jayson and AStJ Dixon. Intra-articular pressure in rheumatoid arthritis of the knee. *Ann. Rheum. Dis*, 29:266, 1970.

[78] MI Jayson and A St Dixon. Intra-articular pressure in rheumatoid arthritis of the knee. 3. pressure changes during joint use. *Annals of the rheumatic diseases*, 29(4):401, 1970.

[79] Shahid Jawed, Karl Gaffney, and David R Blake. Intra-articular pressure profile of the knee joint in a spectrum of inflammatory arthropathies. *Annals of the rheumatic diseases*, 56(11):686–689, 1997.

[80] MJ Viitanen, AM Wilson, HP McGuigan, KD Rogers, and SA May. Effect of foot balance on the intra-articular pressure in the distal interphalangeal joint in vitro. *Equine veterinary journal*, 35(2):184–189, 2003.

[81] DB Myers and DG Palmer. Capsular compliance and pressure-volume relationships in normal and arthritic knees. *Bone & Joint Journal*, 54 (4):710–716, 1972.

[82] S Nade and PJ Newbold. Pressure-volume relationships and elastance in the knee joint of the dog. *The Journal of physiology*, 357(1):417–439, 1984.

[83] N Schwarz, M Leixnering, R Hopf, and S Jantsch. Pressure-volume ratio in human cadaver hip joints. *Archives of orthopaedic and traumatic surgery*, 107(5):322–325, 1988.

[84] Chi-Hung Yen, Hon-Bong Leung, and Paul Yun-Tin Tse. Effects of hip joint position and intra-capsular volume on hip joint intra-capsular pressure: a human cadaveric model. *Journal of orthopaedic surgery and research*, 4(1):8, 2009.

[85] H Fahrer, HU Rentsch, NJ Gerber, Ch Beyeler, Ch W Hess, and B Grunig. Knee effusion and reflex inhibition of the quadriceps. a bar to effective retraining. *Bone & Joint Journal*, 70(4):635–638, 1988.

[86] Michael R Torry, Michael J Decker, Randall W Viola, Dennis D OConnor, and J Richard Steadman. Intra-articular knee joint effusion induces quadriceps avoidance gait patterns1. *Clinical Biomechanics*, 15(3):147–159, 2000.

[87] Jon T Hopkins, Christopher D Ingersoll, B Andrew Krause, Jeffrey E Edwards, and Mitchell L Cordova. Effect of knee joint effusion on quadriceps and soleus motoneuron pool excitability. *Medicine & Science in Sports & Exercise*, 33(1):123–126, 2001.

[88] JD Spencer, KC Hayes, and Ian J Alexander. Knee joint effusion and quadriceps reflex inhibition in man. *Archives of physical medicine and rehabilitation*, 65(4):171–177, 1984.

[89] Pierre Geborek, Ulrich Moritz, and FA Wollheim. Joint capsular stiffness in knee arthritis. relationship to intraarticular volume, hydrostatic pressures, and extensor muscle function. *The Journal of rheumatology*, 16(10):1351–1358, 1989.

[90] Corinne R Henak, Benjamin J Ellis, Michael D Harris, Andrew E Anderson, Christopher L Peters, and Jeffrey A Weiss. Role of the acetabular labrum in load support across the hip joint. *Journal of biomechanics*, 44(12):2201–2206, 2011.

[91] Jocelyn N Todd, Travis G Maak, Gerard A Ateshian, Steve A Maas, and Jeffrey A Weiss. Hip chondrolabral mechanics during activities of daily

living: Role of the labrum and interstitial fluid pressurization. *Journal of Biomechanics*.

[92] SJ Ferguson, John Timothy Bryant, R Ganz, and K Ito. An in vitro investigation of the acetabular labral seal in hip joint mechanics. *Journal of biomechanics*, 36(2):171–178, 2003.

[93] SJ Ferguson, JT Bryant, R Ganz, and K Ito. The acetabular labrum seal: a poroelastic finite element model. *Clinical Biomechanics*, 15(6): 463–468, 2000.

[94] SJ Ferguson, JT Bryant, R Ganz, and K Ito. The influence of the acetabular labrum on hip joint cartilage consolidation: a poroelastic finite element model. *Journal of biomechanics*, 33(8):953–960, 2000.

[95] Hans Gregersen, GS Kassab, and YC Fung. Determination of membrane tension during balloon distension of intestine. *MCB-TECH SCIENCE PRESS-*, 1:191–200, 2004.

[96] Peter V Giannoudis, Haralambos Dinopoulos, and Eleftherios Tsiridis. Bone substitutes: an update. *Injury*, 36(3):S20–S27, 2005.

[97] Anna Tampieri, Simone Sprio, Andrea Ruffini, Giancarlo Celotti, Isidoro Giorgio Lesci, and Norberto Roveri. From wood to bone: multi-step process to convert wood hierarchical structures into biomimetic hydroxyapatite scaffolds for bone tissue engineering. *Journal of Materials Chemistry*, 19(28):4973–4980, 2009.

[98] R Bermejo, C Baudín, R Moreno, L Llanes, and AJ Sánchez-Herencia. Processing optimisation and fracture behaviour of layered ceramic composites with highly compressive layers. *Composites Science and Technology*, 67(9):1930–1938, 2007.

[99] Masaru Palakurthi Rao, AJ Sanchez-Herencia, GE Beltz, RM McMeeking, and FF Lange. Laminar ceramics that exhibit a threshold strength. *Science*, 286(5437):102–105, 1999.

[100] M Lugovy, V Slyunyayev, N Orlovskaya, G Blugan, J Kuebler, and M Lewis. Apparent fracture toughness of Si 3 N 4-based laminates with residual compressive or tensile stresses in surface layers. *Acta Materialia*, 53(2):289–296, 2005.

[101] M Lugovy, N Orlovskaya, V Slyunyayev, G Gogotsi, J Kübler, and AJ Sanchez-Herencia. Crack bifurcation features in laminar specimens with fixed total thickness. *Composites Science and Technology*, 62(6): 819–830, 2002.

[102] Esteban P Busso, Yuri Tkach, and Rowland P Travis. Thermally induced failure of multilayer ceramic structures. *Philosophical Magazine A*, 81 (8):1979–1995, 2001.

[103] Nina Orlovskaya, Mykola Lugovy, Vladimir Subbotin, Oleksandr Radchenko, Jane Adams, Munjal Chheda, James Shih, Jag Sankar, and Sergey Yarmolenko. Robust design and manufacturing of ceramic laminates with controlled thermal residual stresses for enhanced toughness. *Journal of Materials Science*, 40(20):5483–5490, 2005.

[104] Vincenzo M Sglavo and Massimo Bertoldi. Design and production of ceramic laminates with high mechanical resistance and reliability. *Acta Materialia*, 54(18):4929–4937, 2006.

[105] Michael G Pontin and Fred F Lange. Crack bifurcation at the surface of laminar ceramics that exhibit a threshold strength. *Journal of the American Ceramic Society*, 88(5):1315–1317, 2005.

[106] Michael G Pontin, Masa P Rao, Antonio J Sánchez-Herencia, and Fred F Lange. Laminar ceramics utilizing the zirconia tetragonal-to-monoclinic phase transformation to obtain a threshold strength. *Journal of the American Ceramic Society*, 85(12):3041–3048, 2002.

[107] WJ Clegg, K Kendall, N McN Alford, TW Button, and JD Birchall. A simple way to make tough ceramics. *Nature*, 347(6292):455–457, 1990.

[108] Anna Karina F Costa, Robert D Kelly, Garry JP Fleming, Alexandre Luiz S Borges, and Owen Addison. Laminated ceramics with elastic interfaces: A mechanical advantage? *Journal of dentistry*, 43(3):335–341, 2015.

[109] Paul Calvert, Joe Cesarano, Haripin Chandra, Hugh Denham, Sridhar Kasichainula, and Ranji Vaidyanathan. Toughness in synthetic and biological multilayered systems. *Philosophical Transactions of the Royal Society of London A: Mathematical, Physical and Engineering Sciences*, 360(1791):199–209, 2002.

[110] W Johnson and S Chandrasekar. Rupert's glass drops: Residual-stress measurements and calculations and hypotheses for explaining disintegrating fracture. *Journal of Materials Processing Technology*, 31(3): 413–440, 1992.

[111] Gennaro Vitucci and Gennady Mishuris. Analysis of residual stresses in thermoelastic multilayer cylinders. *Journal of the European Ceramic Society*, 36(9):2411–2417, 2016.

[112] Muzaffer Stucu. A recursive concentric cylinder model for composites containing coated fibers. *International Journal of Solids and Structures*, 29(2):197–213, 1992.

[113] XC Zhang, BS Xu, HD Wang, Y Jiang, and YX Wu. Prediction of three-dimensional residual stresses in the multilayer coating-based systems with cylindrical geometry. *Composites science and technology*, 66(13): 2249–2256, 2006.

[114] Knut Vedeld and Håvar A Sollund. Stresses in heated pressurized multilayer cylinders in generalized plane strain conditions. *International Journal of Pressure Vessels and Piping*, 120:27–35, 2014.

[115] I Sevostianov, R Rodriguez-Ramos, R Guinovart-Diaz, J Bravo-Castillero, and FJ Sabina. Connections between different models describing imperfect interfaces in periodic fiber-reinforced composites. *International Journal of Solids and Structures*, 49(13):1518–1525, 2012.

[116] Farid F Abraham, Jeremy Q Broughton, N Bernstein, and E Kaxiras. Spanning the continuum to quantum length scales in a dynamic simulation of brittle fracture. *EPL (Europhysics Letters)*, 44(6):783, 1998.

[117] Fouad Atrash and Dov Sherman. Evaluation of the thermal phonon emission in dynamic fracture of brittle crystals. *Physical Review B*, 84 (22):224307, 2011.

[118] JE Bolander and N Sukumar. Irregular lattice model for quasistatic crack propagation. *Physical Review B*, 71(9):094106, 2005.

[119] Jia-Lin Tsai, Shi-Hua Tzeng, and Yu-Jen Tzou. Characterizing the fracture parameters of a graphene sheet using atomistic simulation and continuum mechanics. *International Journal of Solids and Structures*, 47 (3):503–509, 2010.

[120] Nicholas J Glassmaker, Anand Jagota, Chung-Yuen Hui, William L Noderer, and Manoj K Chaudhury. Biologically inspired crack trapping for enhanced adhesion. *Proceedings of the National Academy of Sciences*, 104(26):10786–10791, 2007.

[121] Michael Marder and Steve Gross. Origin of crack tip instabilities. *Journal of the Mechanics and Physics of Solids*, 43(1):1–48, 1995.

[122] N Bernstein and DW Hess. Lattice trapping barriers to brittle fracture. *Physical review letters*, 91(2):025501, 2003.

[123] David A Kessler and Herbert Levine. Does the continuum theory of dynamic fracture work? *Physical Review E*, 68(3):036118, 2003.

[124] Erik Bitzek, James R. Kermode, and Peter Gumbsch. Atomistic aspects of fracture. *International Journal of Fracture*, 191(1):13–30, 2015. doi: 10.1007/s10704-015-9988-2. URL http://dx.doi.org/10.1007/s10704-015-9988-2.

[125] Yu V Petrov and AA Utkin. Dependence of the dynamic strength on loading rate. *Materials Science*, 25(2):153–156, 1989.

[126] GA Volkov, Yu V Petrov, and AA Utkin. On some principal features of data processing of spall fracture tests. *Physics of the Solid State*, 59(2): 310–315, 2017.

[127] Yu V Petrov. Incubation time criterion and the pulsed strength of continua: fracture, cavitation, and electrical breakdown. In *Doklady Physics*, volume 49, pages 246–249. Springer, 2004.

[128] AA Gruzdkov and Yu V Petrov. Cavitation breakup of low-and high-viscosity liquids. *Technical Physics*, 53(3):291–295, 2008.

[129] Floyd R Tuler and Barry M Butcher. A criterion for the time dependence of dynamic fracture. *International Journal of Fracture Mechanics*, 4(4): 431–437, 1968.

[130] M Boustie and F Cottet. Experimental and numerical study of laser induced spallation into aluminum and copper targets. *Journal of applied physics*, 69(11):7533–7538, 1991.

[131] Shen Wei, Fan Qun-bo, Wang Fu-chi, and Ma Zhuang. Modeling of micro-crack growth during thermal shock based on microstructural images of thermal barrier coatings. *Computational Materials Science*, 46 (3):600–602, 2009.

[132] Dennis E Grady. Length scales and size distributions in dynamic fragmentation. *International Journal of Fracture*, 163(1):85–99, 2010.

[133] K Ravi-Chandar and WG Knauss. An experimental investigation into dynamic fracture: III. On steady-state crack propagation and crack branching. *International Journal of Fracture*, 26(2):141–154, 1984.

[134] Jay Fineberg, Steven P Gross, M Marder, and Harry L Swinney. Instability in dynamic fracture. *Physical Review Letters*, 67(4):457, 1991.

[135] Jens A Hauch, Dominic Holland, MP Marder, and Harry L Swinney. Dynamic fracture in single crystal silicon. *Physical Review Letters*, 82 (19):3823, 1999.

[136] Michele Brun, Gian Felice Giaccu, Alexander B Movchan, and Leonid I Slepyan. Transition wave in the collapse of the san saba bridge. *Frontiers in Materials*, 1:12, 2014.

[137] Kinetic King. The kinetic king detonates a guinness world-record stick bomb – 2250 sticks! URL https://www.youtube.com/watch?v=jiWxU3jXOFc.

[138] Nikolai Gorbushin, Gennaro Vitucci, Grigory Volkov, and Gennady Mishuris. Influence of fracture criteria on dynamic fracture propagation in a discrete chain. *International Journal of Fracture*, 209(1-2): 131–142, 2018.

[139] Ivan Argatov and Gennady Mishuris. *Contact Mechanics of Articular Cartilage Layers*. Springer, 2015.

[140] II Argatov and GS Mishuris. An asymptotic model for a thin biphasic poroviscoelastic layer. *The Quarterly Journal of Mechanics and Applied Mathematics*, 68(3):289–297, 2015.

[141] Salvatore Federico, Alfio Grillo, and Shoji Imatani. The linear elasticity tensor of incompressible materials. *Mathematics and Mechanics of Solids*, 20(6):643–662, 2015.

[142] Travis J Klein, Manu Chaudhry, Won C Bae, and Robert L Sah. Depth-dependent biomechanical and biochemical properties of fetal, newborn, and tissue-engineered articular cartilage. *Journal of biomechanics*, 40 (1):182–190, 2007.

[143] Christopher CB Wang, Clark T Hung, and Van C Mow. An analysis of the effects of depth-dependent aggregate modulus on articular cartilage stress-relaxation behavior in compression. *Journal of Biomechanics*, 34 (1):75–84, 2001.

[144] ALICE Maroudas, PETER Bullough, SAV Swanson, and MAR Freeman. The permeability of articular cartilage. *Journal of Bone & Joint Surgery, British Volume*, 50(1):166–177, 1968.

[145] Ivan Argatov and Gennady Mishuris. Articular contact mechanics from an asymptotic modeling perspective: a review. *Frontiers in Bioengineering and Biotechnology*, 4:83, 2016.

[146] JZ Wu, W Herzog, and J Ronsky. Modeling axi-symmetrical joint contact with biphasic cartilage layers–an asymptotic solution. *Journal of biomechanics*, 29(10):1263–1281, 1996.

[147] Ali Hosseini, Samuel K Van de Velde, Michal Kozanek, Thomas J Gill, Alan J Grodzinsky, Harry E Rubash, and Guoan Li. In-vivo time-dependent articular cartilage contact behavior of the tibiofemoral joint. *Osteoarthritis and cartilage*, 18(7):909–916, 2010.

[148] SI Barry and M Holmes. Asymptotic behaviour of thin poroelastic layers. *IMA journal of applied mathematics*, 66(2):175–194, 2001.

[149] Fuqian Yang. Asymptotic solution to axisymmetric indentation of a compressible elastic thin film. *Thin Solid Films*, 515(4):2274–2283, 2006.

[150] Gerhard A Holzapfel and Ray W Ogden. *Biomechanics: Trends in Modeling and Simulation*, volume 20. Springer, 2016.

[151] Václav Klika, Eamonn A Gaffney, Ying-Chun Chen, and Cameron P Brown. An overview of multiphase cartilage mechanical modelling and its role in understanding function and pathology. *Journal of the mechanical behavior of biomedical materials*, 62:139–157, 2016.

[152] GE Kempson, MAR Freeman, and SAV Swanson. The determination of a creep modulus for articular cartilage from indentation tests on the human femoral head. *Journal of biomechanics*, 4(4):239–250, 1971.

[153] AF Mak. The apparent viscoelastic behavior of articular cartilagethe contributions from the intrinsic matrix viscoelasticity and interstitial fluid flows. *Journal of biomechanical engineering*, 108(2):123–130, 1986.

[154] Sergei Rogosin, Gennady Mishuris, Anna Koroleva, and Anastasiya Vinakurava. Analysis of the unilateral contact problem for biphasic cartilage layers with an elliptic contact zone and accounting for tangential displacements. *Mathematical Modelling and Analysis*, 21(5):585–609, 2016.

[155] JZ Wu and W Herzog. On the pressure gradient boundary condition for the contact of two biphasic cartilage layers. *Journal of biomechanics*, 33 (10):1331–1332, 2000.

[156] II Argatov and GS Mishuris. A closed-form solution of the three-dimensional contact problem for biphasic cartilage layers. *preprint arXiv:1009.4490*, 2010.

[157] D Dowson and JQ Yao. Elastohydrodynamic lubrication of soft-layered solids at elliptical contacts: part 2: film thickness analysis. *Proceedings of the Institution of Mechanical Engineers, Part J: Journal of Engineering Tribology*, 208(1):43–52, 1994.

[158] Miroslav Hlaváček. Elliptical contact on elastic incompressible coatings. *Engineering Mechanics*, 15(4):249–261, 2008.

[159] Bertram Alexander Auld. *Acoustic fields and waves in solids*. Ripol Classic, 1973.

[160] Christopher C-B Wang, Nadeen O Chahine, Clark T Hung, and Gerard A Ateshian. Optical determination of anisotropic material properties of bovine articular cartilage in compression. *Journal of biomechanics*, 36(3):339–353, 2003.

[161] Kathryn E Keenan, Lampros C Kourtis, Thor F Besier, Derek P Lindsey, Garry E Gold, Scott L Delp, and Gary S Beaupre. New resource for the computation of cartilage biphasic material properties with the interpolant response surface method. *Computer methods in biomechanics and biomedical engineering*, 12(4):415–422, 2009.

[162] JZ Wu and W Herzog. Elastic anisotropy of articular cartilage is associated with the microstructures of collagen fibers and chondrocytes. *Journal of biomechanics*, 35(7):931–942, 2002.

[163] Mark R Buckley, Attila J Bergou, Jonathan Fouchard, Lawrence J Bonassar, and Itai Cohen. High-resolution spatial mapping of shear properties in cartilage. *Journal of biomechanics*, 43(4):796–800, 2010.

[164] Federica Boschetti, Giancarlo Pennati, Francesca Gervaso, Giuseppe M Peretti, and Gabriele Dubini. Biomechanical properties of human articular cartilage under compressive loads. *Biorheology*, 41(3-4):159–166, 2004.

[165] Federica Boschetti and Giuseppe M Peretti. Mechanical properties of normal and osteoarthritic human articular cartilage. *Journal of Biomechanics*, 41:S171, 2008.

[166] S Martelli and V Pinskerova. The shapes of the tibial and femoral articular surfaces in relation to tibiofemoral movement. *Bone & Joint Journal*, 84(4):607–613, 2002.

[167] Sun I Kim and Tae S Suh. *World Congress of Medical Physics and Biomedical Engineering 2006: August 27-Septmber 1, 20006 COEX Seoul, Korea*, volume 14. Springer Science & Business Media, 2007.

[168] Rainer Siebold, Jeremie Axe, James J Irrgang, Kanglai Li, Scott Tashman, and Freddie H Fu. A computerized analysis of femoral condyle radii in acl intact and contralateral acl reconstructed knees using 3d ct. *Knee surgery, sports traumatology, arthroscopy*, 18(1):26–31, 2010.

[169] Sarah Catherine Walpole, David Prieto-Merino, Phil Edwards, John Cleland, Gretchen Stevens, and Ian Roberts. The weight of nations: an estimation of adult human biomass. *BMC public health*, 12(1):1, 2012.

[170] Frederick W Werner, David C Ayers, Lorin P Maletsky, and Paul J Rullkoetter. The effect of valgus/varus malalignment on load distribution in total knee replacements. *Journal of biomechanics*, 38(2):349–355, 2005.

[171] Andreas Halder, Ines Kutzner, Friedmar Graichen, Bernd Heinlein, Alexander Beier, and Georg Bergmann. Influence of limb alignment on mediolateral loading in total knee replacement. *The Journal of Bone & Joint Surgery*, 94(11):1023–1029, 2012.

[172] JZ Wu, W Herzog, and M Epstein. Joint contact mechanics in the early stages of osteoarthritis. *Medical engineering & physics*, 22(1):1–12, 2000.

[173] SJ Chidlow, WWF Chong, and M Teodorescu. On the two-dimensional solution of both adhesive and non-adhesive contact problems involving functionally graded materials. *European Journal of Mechanics-A/Solids*, 39:86–103, 2013.

[174] M Hlaváček. A note on an asymptotic solution for the contact of two biphasic cartilage layers in a loaded synovial joint at rest. *Journal of biomechanics*, 32(9):987–991, 1999.

[175] C Herberhold, S Faber, T Stammberger, M Steinlechner, R Putz, KH Englmeier, M Reiser, and F Eckstein. In situ measurement of articular cartilage deformation in intact femoropatellar joints under static loading. *Journal of biomechanics*, 32(12):1287–1295, 1999.

[176] Yongnam Song, JM Greve, DR Carter, S Koo, and NJ Giori. Articular cartilage mr imaging and thickness mapping of a loaded knee joint before and after meniscectomy. *Osteoarthritis and cartilage*, 14(8):728–737, 2006.

[177] Lu Wan, Richard J de Asla, Harry E Rubash, and Guoan Li. In vivo cartilage contact deformation of human ankle joints under full body weight. *Journal of orthopaedic research*, 26(8):1081–1089, 2008.

[178] Guoan Li, Lu Wan, and Michal Kozanek. Determination of real-time in-vivo cartilage contact deformation in the ankle joint. *Journal of biomechanics*, 41(1):128–136, 2008.

[179] JT Bingham, R Papannagari, SK Van de Velde, C Gross, TJ Gill, DT Felson, HE Rubash, and G Li. In vivo cartilage contact deformation in the healthy human tibiofemoral joint. *Rheumatology*, 47(11): 1622–1627, 2008.

[180] Choongsoo S Shin, Richard B Souza, Deepak Kumar, Thomas M Link, Bradley T Wyman, and Sharmila Majumdar. In vivo tibiofemoral cartilage-to-cartilage contact area of females with medial osteoarthritis

under acute loading using mri. *Journal of Magnetic Resonance Imaging*, 34(6):1405–1413, 2011.

[181] Deva D Chan, Luyao Cai, Kent D Butz, Stephen B Trippel, Eric A Nauman, and Corey P Neu. In vivo articular cartilage deformation: noninvasive quantification of intratissue strain during joint contact in the human knee. *Scientific reports*, 6, 2016.

[182] UGK Wegst and MF Ashby. The mechanical efficiency of natural materials. *Philosophical Magazine*, 84(21):2167–2186, 2004.

[183] Emad Moeendarbary and Andrew R Harris. Cell mechanics: principles, practices, and prospects. *Wiley Interdisciplinary Reviews: Systems Biology and Medicine*, 6(5):371–388, 2014.

[184] Malcolm D Smith and Mihir D Wechalekar. The synovium. 2014.

[185] Derek James Rutherford. Intra-articular pressures and joint mechanics: Should we pay attention to effusion in knee osteoarthritis? *Medical hypotheses*, 83(3):292–295, 2014.

[186] M Lukoschek, MB Schaffler, DB Burr, RD Boyd, and EL Radin. Synovial membrane and cartilage changes in experimental osteoarthrosis. *Journal of orthopaedic research*, 6(4):475–492, 1988.

[187] Orlando Avila-Pozos, A Klarbring, and AB Movchan. Asymptotic model of orthotropic highly inhomogeneous layered structure. *Mechanics of Materials*, 31(2):101–116, 1999.

[188] Y Benveniste. The effective mechanical behaviour of composite materials with imperfect contact between the constituents. *Mechanics of Materials*, 4(2):197–208, 1985.

[189] Y Benveniste and T Miloh. Imperfect soft and stiff interfaces in two-dimensional elasticity. *Mechanics of Materials*, 33(6):309–323, 2001.

[190] W Huang, SI Rokhlin, and YJ Wang. Analysis of different boundary condition models for study of wave scattering from fiber-matrix interphases. *The Journal of the Acoustical Society of America*, 101(4):2031–2042, 1997.

[191] Alexander Linkov and Nikolay Filippov. Difference equations approach to the analysis of layered systems. *Meccanica*, 26(4):195–209, 1992.

[192] GS Mishuris. 2-D boundary value problems of thermoelasticity in a multi-wedge-multi-layered region. Part 1. Sweep method. *Archives of Mechanics*, 49(6):1103–1134, 1997.

[193] W Dornisch, G Vitucci, and S Klinkel. The weak substitution method–an application of the mortar method for patch coupling in NURBS-based isogeometric analysis. *International Journal for Numerical Methods in Engineering*, 2015.

[194] W Geis, G Mishuris, and AM Sändig. Piezoelectricity in multilayer actuators. modelling and analysis in two and three dimensions. *Preprint IANS*, 23, 2003.

[195] G Mishuris, A Ochsner, and G Kuhn. FEM-Analysis of nonclassical transmission conditions between elastic structures part 1: soft imperfect interface. *CMC-Tech Science Press*, 2(4):227–238, 2005.

[196] G Mishuris, A Ochsner, and G Kuhn. FEM-analysis of nonclassical transmission conditions between elastic structures. Part 2: Stiff imperfect interface. *CMC-Tech Science Press*, 4(3):137 – 152, 2006.

[197] Michal Wrobel and Gennady Mishuris. Numerical method for solving joint thermo-diffusive problems in an infinite combined domain with thin resistant interphase. *The International Journal of Multiphysics*, 3(2): 111–128, 2009.

[198] Michal Wrobel and Gennady Mishuris. Numerical modelling of mass transfer problems in combined domains with non-linear imperfect transmission conditions. In *Defect and Diffusion Forum*, volume 283, pages 527–532. Trans Tech Publ, 2009.

[199] Mohamed N Rahaman. *Ceramic processing*. Wiley Online Library, 2006.

[200] A Jagota and CY Hui. Mechanics of sintering thin films – ii. cracking due to self-stress. *Mechanics of Materials*, 11(3):221–234, 1991.

[201] RJ Bruls, HT Hintzen, G De With, and R Metselaar. The temperature dependence of the Young's modulus of MgSiN 2, AlN and Si 3 N 4. *Journal of the European Ceramic Society*, 21(3):263–268, 2001.

[202] VA Yeremeyev, AB Freidin, and LL Sharipova. The stability of the equilibrium of two-phase elastic solids. *Journal of Applied Mathematics and Mechanics*, 71(1):61–84, 2007.

[203] Holm Altenbach, Victor A Eremeyev, and Nikita F Morozov. On the influence of residual surface stresses on the properties of structures at the nanoscale. In *Surface Effects in Solid Mechanics*, pages 21–32. Springer, 2013.

[204] Victor A Eremeyev. On effective properties of materials at the nano- and microscales considering surface effects. *Acta Mechanica*, 10:1007, 2015.

[205] Etienne Munch, Maximimilan E Launey, Daan H Alsem, Eduardo Saiz, Antoni P Tomsia, and Robert O Ritchie. Tough, bio-inspired hybrid materials. *Science*, 322(5907):1516–1520, 2008.

[206] LI Slepyan and LV Troyankina. Fracture wave in a chain structure. *Journal of Applied Mechanics and Technical Physics*, 25(6):921–927, 1984.

[207] Leonid I Slepyan. *Models and phenomena in fracture mechanics*. Springer Science & Business Media, 2012.

[208] Leonid I Slepyan, MV Ayzenberg-Stepanenko, and John P Dempsey. A lattice model for viscoelastic fracture. *Mechanics of Time-Dependent Materials*, 3(2):159–203, 1999.

[209] O Kresse and L Truskinovsky. Lattice friction for crystalline defects: from dislocations to cracks. *Journal of the Mechanics and Physics of Solids*, 52(11):2521–2543, 2004.

[210] MJ Nieves, GS Mishuris, and LI Slepyan. Analysis of dynamic damage propagation in discrete beam structures. *International Journal of Solids and Structures*, 97:699–713, 2016.

[211] Nikolai Gorbushin and Gennady Mishuris. Analysis of dynamic failure of the discrete chain structure with non-local interactions. *Mathematical Methods in the Applied Sciences*, 2016. doi: 10.1002/mma.4178.

[212] Robb Thomson, C Hsieh, and V Rana. Lattice trapping of fracture cracks. *Journal of Applied Physics*, 42(8):3154–3160, 1971.

[213] Nikolai Gorbushin and Gennady Mishuris. Dynamic fracture of a discrete media under moving load. *Accepted for publication of International Journal of Solids and Structures. preprint arXiv:1701.02725*, 2017.

[214] Lucas Máximo Alves and Rui F. R. M. Lobo. The possibility to predict crack patterns on dynamic fracture. *International Journal of Fracture*, pages 1–23, 2017.

[215] Gennady S Mishuris, Alexander B Movchan, Leonid I Slepyan, et al. Dynamics of a bridged crack in a discrete lattice. *Quarterly journal of mechanics and applied mathematics*, 61(2):151–160, 2008.

[216] Gennady S Mishuris, Alexander B Movchan, and Leonid I Slepyan. Localised knife waves in a structured interface. *Journal of the Mechanics and Physics of Solids*, 57(12):1958–1979, 2009.

[217] Leonid I Slepyan, Alexander B Movchan, and Gennady S Mishuris. Crack in a lattice waveguide. *International Journal of Fracture*, 162 (1):91–106, 2010.

[218] Leonid Slepyan, Mark Ayzenberg-Stepanenko, and Gennady Mishuris. Forerunning mode transition in a continuous waveguide. *Journal of the Mechanics and Physics of Solids*, 78:32–45, 2015.

[219] MJ Nieves, GS Mishuris, and LI Slepyan. Transient wave in a transformable periodic flexural structure. *International Journal of Solids and Structures*, 112:185–208, 2017.

[220] Nikolai Gorbushin and Gennady Mishuris. Dynamic crack propagation along the interface with non-local interactions. *Journal of the European Ceramic Society*, 36(9):2241–2244, 2016.

[221] Mark Ayzenberg-Stepanenko, Gennady Mishuris, and Leonid Slepyan. Brittle fracture in a periodic structure with internal potential energy. spontaneous crack propagation. In *Proc. R. Soc. A*, volume 470, page 20140121. The Royal Society, 2014.

[222] G. Mishuris, A.B. Movchan, and L.I. Slepyan. Waves and fracture in an inhomogeneous lattice structure. *Waves in Random and Complex Media*, 17(4):409–428, 2007.

[223] M.J. Nieves, A.B. Movchan, I.S. Jones, and G.S. Mishuris. Propagation of slepyan's crack in a non-uniform elastic lattice. *Journal of the Mechanics and Physics of Solids*, 61(6):1464–1488, 2013.

[224] JR Xiao, J Staniszewski, and JW Gillespie. Fracture and progressive failure of defective graphene sheets and carbon nanotubes. *Composite structures*, 88(4):602–609, 2009.

[225] Rudolf Merkel, Pierre Nassoy, Andrew Leung, Ken Ritchie, and Evan Evans. Energy landscapes of receptor–ligand bonds explored with dynamic force spectroscopy. *Nature*, 397(6714):50–53, 1999.

[226] Peter Hinterdorfer and Yves F Dufrêne. Detection and localization of single molecular recognition events using atomic force microscopy. *Nature methods*, 3(5):347–355, 2006.

[227] Y. Wei and J. Hutchinson. Interface strength, work of adhesion and plasticity in the peel test. *International Journal of Fracture*, 1:315333, 1998.

[228] M. Nase, M. Rennert, K. Naumenko, and V. A. Eremeyev. Identifying tractionseparation behavior of self-adhesive polymeric films from in situ digital images under t-peeling. *Int. J. Fract.*, 91:40–55, 2016.

Acknowledgements

Finally, after much effort, the most read section of many theses. Will I escape the trend?

Gennady is a multi-faceted, intuitive scientist and an extremely tough mathematician. He taught me a lot, but perhaps most importantly how to raise worthy questions. He encouraged me with his overflowing energy whenever I was in need. Graduates should crowd in Aberystwyth for being supervised by him. I was lucky in meeting his colleague Ivan who switched a light on in me about the fact that engineers must not be shy to open their mind to biological sciences. They are indeed very much welcome to do so. Thank you both.

The funding from the Marie Curie ITN European Project *CERMAT2* has been generous and has enabled me to attend many scientific meetings and postgraduate courses. My overall postgraduate experience has received a huge boost.

A fantastic view on the Cardigan Bay helped me bearing the mist and gloom of the Welsh weather, which you are told has been great anytime you were away (incidentally, I never believed you, people!). It has been possible only thanks to those dragons of inner and outer balance who respond to the names Sam and Bongo. You attracted only lovely people as house mates. Apart from me.

Far and near friends, you will be acknowledged by given name initials only. Repeated initials will be counted once. In order not to offend

anyone with the sorting, you have even been shuffled with a random-generator in Python:

$$['B','N','P','A','D','S','K','R','F','M','J','L','C','T','V','G'].$$

The original list has been deleted for shunning remonstrations. However, it has been fun and a stimulating time. We shall have more of it. Grazie a tutti.

That F is not Francesca's, who deserves a special separate mention because, besides many amusing moments, she had also to endure bad sides which were mostly spared to the others.

I am always amazed at people acknowledging their family because *without them this would not be possible*. It is self evident on the ground of well documented scientific reasons. Still it true also in less trivial ways, at least in this case. Thank you, dear Skype correspondents!